



Funded by  
the European Union



# A framework for data & information exchange for seismic risk harmonization in the Greece- Türkiye Cross Border Area

## Deliverable No: D4.1

**WP4: Joint investigation of seismic risk indicators based on  
instrumentation of school buildings (pilot sites in the CBA)**

**T4.1: Design and Manufacture of Next Generation Accelerometers**

**T4.2 Deployment of Next Generation Accelerometers in selected schools  
of the pilot sites**

**D4.1 Investigation of seismic risk indicators based on instrumentation of  
school buildings in the selected pilot sites**

### **DELIVERABLE COORDINATED BY:**

**ORGANISMOS ANTISEISMIKOU SXEDIASMOU KAI PROSTASIAS (OASP  
EPPO EARTHQUAKE PLANNING AND PROTECTION ORGANIZATION)  
(ITSAK/EPPO)**

### **INVOLVED PARTNERS:**

**DIETHNES PANEPISTIMIO ELLADOS (IHU)**

**GEBZE TEKNİK UNIVERSİTESİ (GTU)**

**ICISLERI BAKANLIGI AFET VE ACIL DURUM YONETIMI BASKANLIGI  
(AFAD)**

## PROJECT DETAILS

	EUROPEAN COMMISSION Directorate-General for European Civil Protection and Humanitarian Aid Operations (ECHO) ECHO.B - Disaster Preparedness and Prevention B.2 - Prevention and Disaster Risk Management
Project No	101101206
Project Name	Earthquake Resilient Schools
Project Acronym	EReS
Call	UCPM-2022-PP
Topic	UCPM-2022-PP
Type of action	UCPM Project Grants
Granting authority	European Commission-EU
Lead Partner	DIETHNES PANEPISTIMIO ELLADOS (IHU)
Total Budget	923.784,50 Euro (€)
Grant Amount	785.215,92 Euro (€)
Time Frame: Start Date - End Date	01/03/2023 - 28/02/2025
Project Coordinator	Papatheodorou K. (IHU)

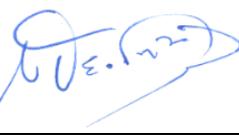
## DELIVERABLE CONTRIBUTORS

<b>IHU:</b>	Papatheodorou K., Panagopoulos G., Kirtas Em., Panagiotopoulos Ch.
<b>GTU:</b>	Zülfikar C., Tugsal Mert Ü., Ergen V., Yeşilyurt A.
<b>AFAD:</b>	Nurlu M., Kuterdem K., Sezer S., Tekin B.M.
<b>ITSAK/EPPO:</b>	Theodoulidis N., Papanikolaou V., Morfidis K., Konstantindou K.

## **RECORD OF REVISIONS**

<b>Release</b>	<b>Date</b>	<b>Description of Change</b>
v.01	18.09.2024	First version of the document
v.02	30.10.2024	Final version of the document

## DOCUMENT RELEASE SHEET

<b>Deliverable Responsible Partner: GTU</b>		
<b>Approval</b>	<b>Konstantinos Papatheodorou (IHU)</b>	 Signature 31.10.2024
<b>Approval</b>	<b>Can Zulfikar (GTU)</b>	 Signature 31.10.2024
<b>Approval</b>	<b>Murat Nurlu (AFAD)</b>	 Signature 31.10.2024
<b>Approval</b>	<b>Nikolaos Theodoulidis (ITSAK/OASP)</b>	 Signature 31.10.2024
<b>Distribution:</b>	<b>ALL PARTNERS</b>	

## TABLE OF CONTENTS

<b><u>1</u></b>	<b><u>BACKGROUND OF THE DOCUMENT</u></b> .....	<b>11</b>
1.1	RELATED WORKPACKAGE AND TASKS.....	11
1.2	SCOPE AND OBJECTIVES .....	11
1.3	EXECUTIVE SUMMARY .....	11
<b><u>2</u></b>	<b><u>INSTRUMENTATION OF SCHOOL BUILDINGS IN THE GREEK PILOT SITES</u></b> .....	<b>13</b>
2.1	DESIGN AND MANUFACTURE OF NEXT GENERATION ACCELEROMETERS .....	13
2.2	INSTALLATIONS IN ALEXANDROUPOLIS .....	26
2.2.1	SELECTION OF SCHOOL BUILDINGS FOR THE INSTALLATIONS.....	27
2.2.2	INSTALLATIONS .....	27
2.3	INSTALLATIONS IN SAMOS.....	32
2.3.1	SELECTION OF SCHOOL BUILDINGS FOR THE INSTALLATIONS.....	32
2.3.2	INSTALLATIONS .....	33
<b><u>3</u></b>	<b><u>INSTRUMENTATION OF SCHOOL BUILDINGS IN THE TURKISH PILOT SITES</u></b> ...	<b>36</b>
3.1	TECHNICAL SPECIFICATION OF NEXT GENERATION ACCELEROMETERS.....	36
3.2	INSTALLATIONS IN IZMIR .....	38
3.2.1	SELECTION OF SCHOOL BUILDINGS FOR THE INSTALLATIONS.....	39
3.2.2	INSTALLATIONS .....	40
3.3	INSTALLATIONS IN ÇANAKKALE .....	46
3.3.1	SELECTION OF SCHOOL BUILDINGS FOR THE INSTALLATIONS.....	46
3.3.2	INSTALLATIONS .....	47
<b><u>4</u></b>	<b><u>INVESTIGATION OF SEISMIC RISK INDICATORS</u></b> .....	<b>54</b>
4.1	SEISMIC DAMAGE INDICATORS BASED ON THE DRIFT RATIO .....	54
4.1.1	DAMAGE ESTIMATES BASED ON THE DRIFT RATIO LEVEL .....	54
4.1.2	DRIFT ESTIMATION BASED ON MEASUREMENTS .....	59
4.1.3	PILOT STUDIES IN TYPICAL SCHOOL BUILDINGS IN THE CBA .....	59
4.2	SEISMIC DAMAGE INDICATORS BASED ON THE DETERIORATION OF STRUCTURAL PROPERTIES IN THE INELASTIC RANGE .....	62
4.2.1	ESTIMATION OF DYNAMIC RESPONSE PROPERTIES BASED ON MEASUREMENTS AT THE TOP AND THE BOTTOM OF THE BUILDINGS.....	63
4.2.2	DAMAGE INDICATORS BASED ON STIFFNESS DEGRADATION.....	64
4.2.2.1	Numerical analysis of a typical school in the CBA .....	64
4.2.2.2	Numerical analysis of a simplified 3-storey, 2D frame.....	70
4.2.2.3	Discussion on the stiffness degradation indicators .....	75
4.3	SEISMIC DAMAGE INDICATORS BASED ON FRAGILITY FUNCTIONS.....	76
<b><u>5</u></b>	<b><u>REFERENCES</u></b> .....	<b>83</b>

**APPENDIX-A: TESTING RESULTS IN TIME DOMAIN (ACCELERATION TIME HISTORIES)..... 85**

**APPENDIX-B: TESTING RESULTS IN FREQUENCY DOMAIN (FAS) ..... 110**

## LIST OF FIGURES

**Figure 1.** The low-cost accelerograph SeismoBug v3.0. .... 14

**Figure 2.** Noise performance (power spectral density) of the employed MEMS sensor. .... 14

**Figure 3.** Software for device configuration and local data retrieval..... 15

**Figure 4.** Dedicated software for record post-processing. .... 16

**Figure 5.** Device online operation..... 16

**Figure 6.** Server terminal communication to the client device. .... 17

**Figure 7.** Remotely recorded acceleration stream from an established station/terminal script. .... 17

**Figure 8.** Remotely recorded acceleration stream from an established station / triaxial accelerogram..... 18

**Figure 9.** (a) The 97 earthquake epicenters in western Greece area and the Argonet location in Ceplalonian island. (b) and (c) The local magnitude,  $M_L$ , of these 97 earthquakes, vs their epicentral distance from the Argonet and vs the corresponding PGA, of the two horizontal (E-W and N-S) and the Vertical components..... 20

**Figure 10.** (a) The RMS of the 97 noise records, are presented for each component separately (red, blue and green for the EW, NS and Vertical component, respectively). Their corresponding average and STD values are also presented in solid and dashed lines (b) The correlation (%) of each one of the 97 S-wave motion record of each component (Appendix A), between the SeismoBug and the CK0 accelerometers vs the PGA detected in the CK0 (c) The ratio between all the PGA detected from SeismoBug and CK0 accelerometers, vs the PGA detected in the CK0..... 21

**Figure 11.** Existing school units in the municipality of Alexandroupolis (top), Selected 5 schools for installation of Low Cost accelerometers (bottom). .... 27

**Figure 12.** Geologic map of the broader area of the city of Alexandroupolis together with the 5 selected school units (1:50.000 scale, IGME maps, <https://www.eagme.gr/site/services>). The ITSAK permanent accelerometer station is also shown as ALX1. .... 28

**Figure 13.** Alexandroupolis 2nd EPAL building instrumented in ground floor and top ceiling. .... 28

**Figure 14.** (a) Alexandroupolis 4<sup>th</sup> high school building instrumented in ground floor and top ceiling (b) Plans of the ground floor and upper floor. .... 29

**Figure 15.** Alexandroupolis 3<sup>rd</sup> high school building instrumented in ground floor and top ceiling. .... 30

**Figure 16.** Alexandroupolis 5<sup>th</sup> high school building instrumented in ground floor and top ceiling. .... 30

<b>Figure 17.</b> Alexandroupolis 2 <sup>nd</sup> high school building instrumented in ground floor and top ceiling. ....	31
<b>Figure 18.</b> Existing school units in the municipality of Vathy-Samos (top), selected 5 schools for installation of Low Cost accelerometers (bottom). ....	32
<b>Figure 19.</b> Geologic map of the broader area of the town of Vathy-Samos (1:50.000 scale, IGME maps, <a href="https://www.eagme.gr/site/services">https://www.eagme.gr/site/services</a> ) together with the 5 selected school units. ....	33
<b>Figure 20.</b> Vathy-Samos “Mavrogeneio“ EPAL building instrumented in ground floor, middle floor and top ceiling. ....	33
<b>Figure 21.</b> Vathy-Samos 2 <sup>nd</sup> high school building instrumented in ground floor and top ceiling. ....	34
<b>Figure 22.</b> Vathy-Samos 2 <sup>nd</sup> Exp. Elementary school building instrumented in ground floor and top ceiling. ....	34
<b>Figure 23.</b> Vathy-Samos 3 <sup>rd</sup> Elementary school building instrumented in ground floor and top ceiling. ....	35
<b>Figure 24.</b> Vathy-Samos Music high school building instrumented in ground floor (reference rock station).....	35
<b>Figure 25.</b> Working Principle of Structural Health Monitoring .....	38
<b>Figure 26.</b> Geographical distribution of the pilot schools with different soil conditions in İzmir province.....	39
<b>Figure 27.</b> Ali Osman Konakçı Mesleki ve Teknik Anadolu Lisesi 3 <sup>rd</sup> Floor Accelerometer Location (Instrumentation).....	40
<b>Figure 28.</b> Ali Osman Konakçı Mesleki ve Teknik Anadolu Lisesi Basement Floor Accelerometer Location (Instrumentation).....	40
<b>Figure 29.</b> Çamkıran Ortaokulu Bayraklı 3 <sup>rd</sup> Floor Accelerometer Location (Instrumentation). ....	41
<b>Figure 30.</b> Çamkıran Ortaokulu Bayraklı Basement Floor Accelerometer Location (Instrumentation).....	41
<b>Figure 31.</b> Bornova Anadolu Lisesi G-Blok 2 <sup>nd</sup> Floor Accelerometer Location (Instrumentation). ....	42
<b>Figure 32.</b> Bornova Anadolu Lisesi G-Blok Basement Floor Accelerometer Location (Instrumentation).....	42
<b>Figure 33.</b> Buca Anadolu Lisesi 2 <sup>nd</sup> Floor Accelerometer Location (Instrumentation). ....	43
<b>Figure 34.</b> Buca Anadolu Lisesi Basement Floor Accelerometer Location (Instrumentation). ....	43
<b>Figure 35.</b> Prof. Dr. Aziz Sancar Ortaokulu 3 <sup>rd</sup> Floor Accelerometer Location (Instrumentation).....	44
<b>Figure 36.</b> Prof. Dr. Aziz Sancar Ortaokulu Basement Floor Accelerometer Location (Instrumentation).....	44
<b>Figure 37.</b> Dr. Güngör Özbek Anadolu Lisesi 2 <sup>nd</sup> Floor Accelerometer Location (Instrumentation).....	45
<b>Figure 38.</b> Dr. Güngör Özbek Anadolu Lisesi Basement Floor Accelerometer Location (Instrumentation).....	45

Figure 39. Geographical distribution of the pilot schools with different soil conditions in Çanakkale province. ....	46
Figure 40. Gelibolu 100. Yıl Barış Ortaokulu 3 <sup>rd</sup> Floor Accelerometer Location (floor plan (left), instrumentation (right)). ....	47
Figure 41. Gelibolu 100. Yıl Barış Ortaokulu Basement Floor Accelerometer Location (floor plan (left), instrumentation (right)). ....	48
Figure 42. Lapseki Erol Çarmıklı Anadolu Lisesi 3 <sup>rd</sup> Floor Accelerometer Location (floor plan (top), instrumentation (bottom)). ....	49
Figure 43. Lapseki Erol Çarmıklı Anadolu Lisesi Basement Floor Accelerometer Location (floor plan (top), instrumentation (bottom)). ....	49
Figure 44. Cevatpaşa Ortaokulu 2 <sup>nd</sup> Floor Accelerometer Location (Instrumentation). ....	50
Figure 45. Cevatpaşa Ortaokulu Basement Floor Accelerometer Location (Instrumentation). ....	50
Figure 46. Gazi Ortaokulu 2 <sup>nd</sup> Floor Accelerometer Location (floor plan (left), instrumentation (right)). ....	51
Figure 47. Gazi Ortaokulu Basement Floor Accelerometer Location (floor plan (left), instrumentation (right)). ....	51
Figure 48. Çanakkale Anadolu Lisesi 2 <sup>nd</sup> Floor Accelerometer Location (Instrumentation)..	52
Figure 49. Çanakkale Anadolu Lisesi Basement Floor Accelerometer Location (Instrumentation). ....	52
Figure 50. Kepez Hafız Halil Atan Ortaokulu 2 <sup>nd</sup> Floor Accelerometer Location (floor plan (left), instrumentation (right)). ....	53
Figure 51. Kepez Hafız Halil Atan Ortaokulu Basement Floor Accelerometer Location (floor plan (left), instrumentation (right)). ....	53
Figure 52. Roof and interstorey displacements (Su et al., 2008) ....	55
Figure 53. Example Fragility Curves for Slight, Moderate, Extensive, and Complete Damage States (Hazus 4.2 SP3, 2020).....	55
Figure 54. Typical Drift Ratios Used to Define Median Values of Structural Damage (top) and Damage for Nonstructural Drift-Sensitive Components (bottom) (Hazus 4.2 SP3, 2020) ....	56
Figure 55. Typical degrees of damage of columns and beams (d: storey drift or drift of member ends, KAN.ΕΠΕ., 2022) ....	57
Figure 56. Damage States for Residual ISD Ratio (FEMA P-58-1, ATC, 2019) ....	57
Figure 57. Experimental values of maximum inter-storey drift ratio (or total drift ratios for low-rise buildings) characterising observed damage limit states in RC structures (top). Judgement/code values of maximum inter-storey drift ratio (or drift ratios for low-rise buildings) characterising damage limit states in RC structures (bottom) (Rossetto, 2003) ....	58
Figure 58. Nodes of finite element model of the typical school building where the drifts are calculated ....	60
Figure 59. Global drift time-history, in x-direction, at node C of the structure for the inelastic response case ....	61

Figure 60. F.E. model of the examined school building (details provided in Deliverable 3.2) .....	65
Figure 61. Fourier ratio of acceleration time-histories between the top and the base of the modeled structure (linear elastic response) .....	66
Figure 62. Plastic hinges developed during nonlinear dynamic analysis .....	67
Figure 63. Fourier ratio of acceleration time-histories between the top and the base of the modeled structure (nonlinear response) .....	67
Figure 64. Fourier ratio of acceleration time-histories between the top and the base of the modeled structure (comparison between linear and nonlinear response) .....	68
Figure 65. Ratios of spectrograms of acceleration time-histories between the top and the base of the modeled structure for linear elastic response (top) and nonlinear response case (bottom) .....	69
Figure 66. Geometry of a simplified concrete frame .....	70
Figure 67. Fourier ratio of acceleration time-histories between the top and the base of the simplified 2D frame (top) and the corresponding spectrogram ratio (bottom) for the linear elastic response .....	71
Figure 68. Plastic hinges for the nonlinear dynamic analyses .....	72
Figure 69. Fourier ratio of acceleration time-histories between the top and the base of the simplified 2D frame (top) and the corresponding spectrogram ratio (bottom) for the nonlinear inelastic response using the Kocaeli motion without scaling.....	73
Figure 70. Fourier ratio of acceleration time-histories between the top and the base of the simplified 2D frame (top) and the corresponding spectrogram ratio (bottom) for the nonlinear inelastic response using the Kocaeli motion scaled x2 .....	73
Figure 71. Fourier ratio of acceleration time-histories between the top and the base of the simplified 2D frame (top) and the corresponding spectrogram ratio (bottom) for the nonlinear inelastic response using the Kocaeli motion scaled x5 .....	74
Figure 72. Basic steps of near real-time seismic risk assessment methodology.....	77
Figure 73. 3D numerical model of the existing school building .....	78
Figure 74. Target spectra for different seismic hazard levels.....	79
Figure 75. Fragility curves presented by Martin Silva 2009 for mid-rise school buildings ...	79
Figure 76. DPM values calculated for different seismic hazard levels.....	80
Figure 77. Identification of damage thresholds in capacity curves .....	81
Figure 78. Capacity curves in both directions; X direction (left), Y direction (right) .....	82

## LIST OF TABLES

Table 1. The information (Date-Time, Longitude, Latitude, Depth, Local Magnitude) from the 97 Events (earthquakes) used in this study (Figure 1), provided by Geodynamic Institute catalogues ( <a href="https://bbnet.gein.noa.gr/HL/">https://bbnet.gein.noa.gr/HL/</a> ).....	23
Table 2. Schools selected in the first stage in İzmir province. ....	39

Table 3. Schools selected in the first stage in Çanakkale province.....	46
Table 4. Global (top to basement) drift estimates at different nodes of the structure for the inelastic analysis.....	60
Table 5. First storey drift estimates at different nodes of the structure for the inelastic analysis.....	61
Table 6. Simplified concrete frame reinforcement. ....	70
Table 7. Consequence model utilized to derive vulnerability functions. ....	80
Table 8. Recommended MDR(%) limits for both directions of the structure.....	82

## **1 BACKGROUND OF THE DOCUMENT**

### **1.1 RELATED WORKPACKAGE AND TASKS**

Deliverable “D4.1. D4.1 Investigation of seismic risk indicators based on instrumentation of school buildings in the selected pilot sites” capitalizes on information produced by previous project deliverables, including “D2.1 A framework for data and information exchange for seismic hazard harmonization in the Greece - Türkiye CBA “and “D3.1 A framework for data & information exchange for seismic risk harmonization in the Greece- Türkiye CBA” which set the basis for harmonized outputs of all following tasks, “D2.2 Joint assessment of seismic hazard in the Greece- Türkiye CBA” and especially “D3.2 Joint assessment of seismic risk in the Greece- Türkiye CBA (school buildings in the pilot sites)”.

This report details the collaborative efforts undertaken to assess earthquake risk in the Greece-Türkiye cross-border area (CBA), specifically focusing on existing school buildings within the selected pilot sites.

### **1.2 SCOPE AND OBJECTIVES**

The scope of this document is to outline the activities carried out within the framework of WP4 and more specifically of Tasks 4.1 and 4.2 aimed at accomplishing the project objectives. These efforts are ultimately geared towards attaining the Specific Objective of "Risk Assessments" as stipulated by the funding Programme under the Call "Prevention and Preparedness Projects on Civil Protection and Marine Pollution (UCPM-2022-PP)."

In pursuit of this goal, the present deliverable places emphasis on the following project objectives:

- Development of next generation accelerometers oriented to the needs of this project.
- Installation of accelerometers at carefully selected school buildings in the pilot sites to monitor strong ground motion (towards improved resolution Shakemaps) and building response.
- Investigation of possible damage indicators based on strong ground motion recordings at the base and roof level of instrumented buildings.

### **1.3 EXECUTIVE SUMMARY**

Deliverable “D4.1. Investigation of seismic risk indicators based on instrumentation of school buildings in the selected pilot sites” emphasizes the

importance of monitoring school buildings to assess their seismic response and potential damage during earthquakes.

It presents a low-cost instrumentation approach for seismic hazard assessment in urban areas, focusing on the development of next-generation accelerometers and their installation at selected pilot sites, specifically in school buildings within the Greek/Turkish cross border area. The technical specifications of the accelerometers are detailed, including their design, manufacturing process, and testing procedures used to evaluate their reliability when necessary.

The next part of the deliverable examines potential damage indicators associated with strong ground motion recordings at the base and roof levels of instrumented buildings. The primary objective of this investigation is to develop an effective method for identifying structural damage in near real-time following an earthquake. It outlines methodologies for utilizing synthetic data and numerical simulations to estimate structural damage and improve seismic risk assessment, highlighting the need for advanced instrumentation and the significance of real-time data collection for effective post-earthquake evaluation and preparedness.

The seismic damage indicators are calculated using real-time recordings at the base and roof levels of the school buildings, either by estimating global and/or interstorey drifts to correlate structural deformations with structural and non-structural damage levels, or by identifying stiffness degradation of the inelastic response through acceleration Fourier ratios between the top and base of the structure. Challenges related to the complexities of accurately assessing structural responses to earthquakes are also discussed. Furthermore, the seismic recordings at the base of the structure allow for the use of appropriate fragility functions to estimate the probabilities of the school buildings exceeding specific damage state thresholds, as well as to propose corresponding consequence models.

Additionally, D4.1 provides appendices that compare time and frequency domain data from 97 recordings, enhancing the understanding of structural behavior during seismic events.

D4.1 findings aim to enhance the understanding of seismic risks and improve the resilience of educational infrastructures against earthquakes within the Greek/Turkish Cross Border Area (CBA). Overall, this study contributes to improving the structural integrity assessment in earthquake-prone areas.

## 2 INSTRUMENTATION OF SCHOOL BUILDINGS IN THE GREEK PILOT SITES

### 2.1 DESIGN AND MANUFACTURE OF NEXT GENERATION ACCELEROMETERS

#### (a) Overview and Technical Specifications

In this section, an overview of the innovative, low-cost, and autonomous accelerograph device **SeismoBug® v3.0** is presented. This device was designed and manufactured in-house for real-time monitoring of strong-motion activity in Alexandroupoli and Samos cities, in the framework of the EReS project. It represents a significant advancement over previous versions, which have been presented, together with field applications (ITSAK, 2015; Karakostas et al., 2014, 2018; Kishida et al., 2016; Papanikolaou & Karakostas, 2014) and employed in previous projects (e.g. REDACT <https://www.redact-project.eu/>). The device has a small form factor (83×58×33 mm), as depicted in Figure 1, and is typically powered by an external power supply (USB). Its continuous operation is safeguarded against power failure, which can occur during a strong motion event, using a rechargeable battery backup system that ensures operation for several hours. A small Wi-Fi antenna provides wireless connectivity, enabling real-time streaming of acceleration data. Furthermore, the device can record vibrational data locally, on non-volatile storage (SD card), integrating a standard STA/LTA motion trigger algorithm. The installation process is simple, as the device is fixed on a flat surface using two small screws. Figure 1 illustrates the SeismoBug v3.0.

The device operates with a high-performance digital triaxial MEMS (micro-electromechanical) acceleration sensor (Papanikolaou & Karakostas, 2013). This sensor has a  $\pm 2g$  range with 20-bit resolution and a nominal noise spectral density (PSD) of  $22.5 \mu g/\sqrt{Hz}$ . The sensor's noise performance was tested directly on the device and found to match the nominal specification, measuring a noise RMS value lower than 0.1 mg at a 125 Hz sampling rate (31.25 Hz bandwidth). Figure 2 compares the noise PSD distribution of this sensor with earlier versions (14-bit) and a commercial-grade accelerograph. It is noted that the frequency response appears flat over the frequency range of interest.



Figure 1. The low-cost accelerometer SeismoBug v3.0.

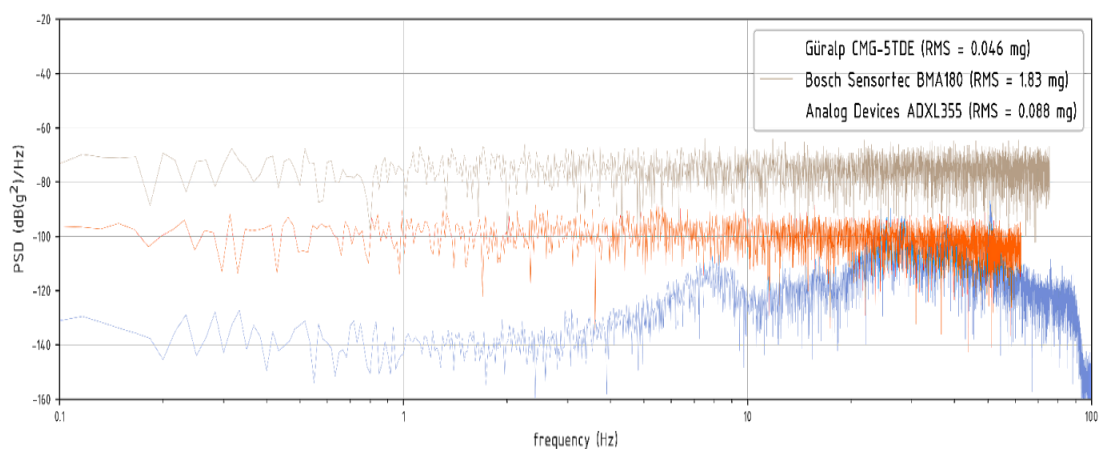


Figure 2. Noise performance (power spectral density) of the employed MEMS sensor.

Besides the acceleration sensor, the device is equipped with additional peripherals including a high-accuracy (**2 ppm**) real-time clock for data timestamping, **serial RAM** for data buffering (used to capture pre-trigger activity), an SD card for local storage, and **Bluetooth** connectivity for local device configuration and data retrieval. An **8-bit** microcontroller facilitates the necessary digital protocols for peripheral interconnectivity (**Serial, SPI**) and houses the device's upgradeable firmware, which manages all necessary operations.

A notable feature of the current version is the inclusion of an auxiliary **Wi-Fi module** based on the **ESP8266** platform (blue, see Fig. 1). This module, mounted as a mezzanine board on the mainboard, receives acceleration data from the mainboard via a serial protocol and provides real-time wireless transmission to a remote server. It contains separate upgradeable firmware that supports bidirectional communication (**client-to-server and vice versa**). In addition to data transmission, the firmware accurately **synchronizes** the device's time using a user-specified **NTP (Network Time Protocol)** server.

After being **physically installed**, the device can be initially configured using custom software (Figure 3) through a wireless Bluetooth connection (or alternatively via a built-in Wi-Fi access point). Configuration parameters include station name, geo-location, local Wi-Fi router settings, remote server parameters, NTP server information, data packet size, sampling rate, local triggering parameters, and more. The device can operate simultaneously in offline (local) and online modes.

The software also provides an interface for retrieving and post-processing locally stored records. Figure 4 showcases the dedicated post-processing software, featuring options to view the recorded triaxial records in both time and frequency domains.

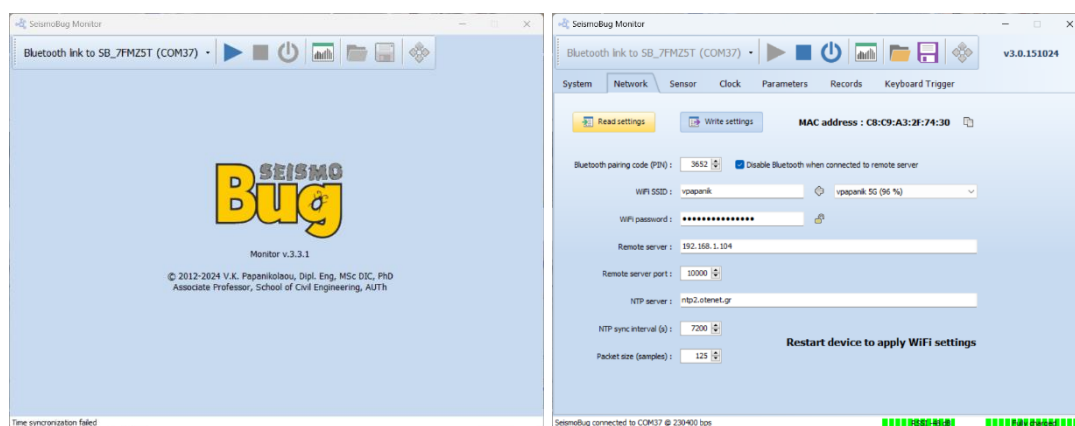


Figure 3. Software for device configuration and local data retrieval.

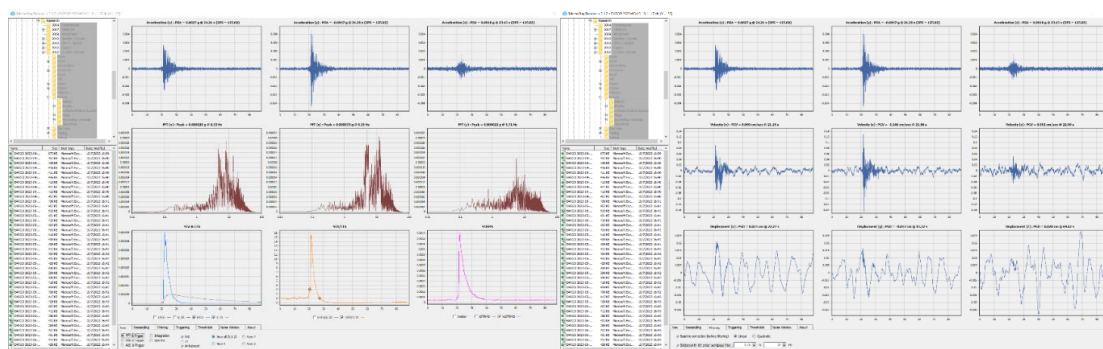


Figure 4. Dedicated software for record post-processing.

When the device operates in online mode, it connects to a local **gateway** (such as a **Wi-Fi** router or access point) using the usual **SSID** (Service Set Identifier) and password like other devices on the local network. Upon successful connection, it is registered in the gateway's network client list with its serial number.

**The device is programmed** to automatically reconnect to the local gateway in case of a network or power failure. **It is recommended** that the device and gateway should remain within a relatively short distance to maintain an **RSSI** (Received Signal Strength Indication) value higher than **-75 dBm**.

After connecting to the local gateway, the device automatically attempts to connect to a user-specified remote server (**or IP address**) using a dedicated **TCP** (Transmission Control Protocol) port. When this port is opened, a bidirectional TCP connection is automatically established, allowing the device to transmit data but also receive instructions from the remote server (Figure 5).



Figure 5. Device online operation.

Once connected to the remote server, several commands (**in human-readable form**) can be sent from the server to the device, even via a simple TCP terminal. These commands allow users to query device identity, synchronize time, modify parameters, reboot the device, and most importantly, **start and stop** continuous acceleration data streaming (Figure 6).

*Earthquake Resilient Schools - EReS [BSB 966]  
 Project Nr: 101101206 (UCPM-2022-PP)  
 Deliverable D4.1: Investigation of seismic risk indicators based on instrumentation  
 of school buildings in the selected pilot sites*

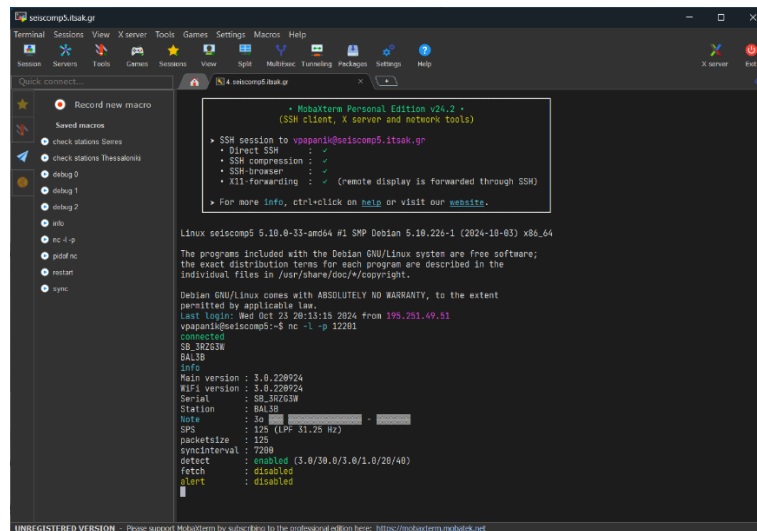


Figure 6. Server terminal communication to the client device.

The most significant feature of the current version is its capability to transmit a continuous acceleration data stream to a remote server. This stream is **comprised of successive TCP data packets**, each containing a header and a series triaxial acceleration sample. The **header consists of a 10-byte timestamp and packet duration**, followed by a user-specified number of **9-byte acceleration samples** (3 axes × 3 bytes per axis). Each packet terminates with a **4-byte CRC32 checksum**, which ensures data integrity. Figures 7-8 show a **100-packet transmission** from an established station collected using a python script, where each packet contains 125 samples. As this measurement was taken in a quiet environment, only sensor noise is displayed, with **RMS = 0.087 mg, 0.088 mg, 0.144 mg** for x, y, z axes. respectively.

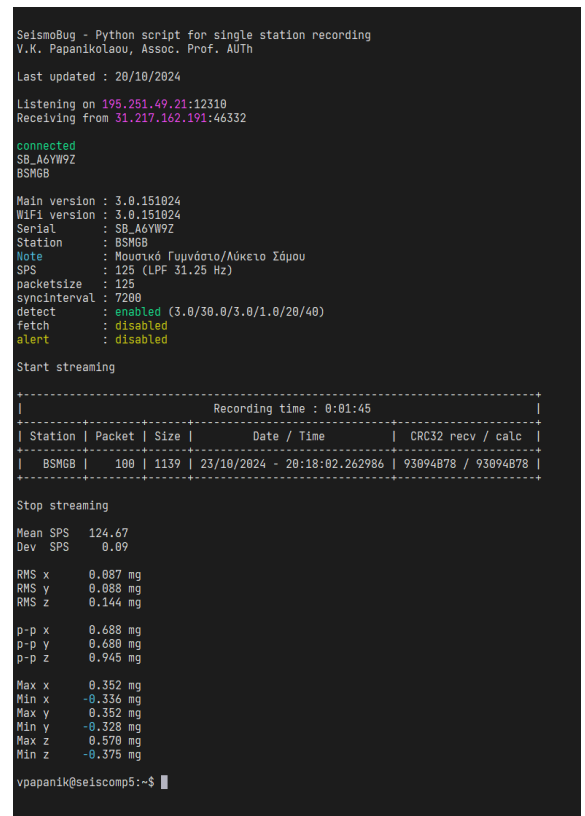
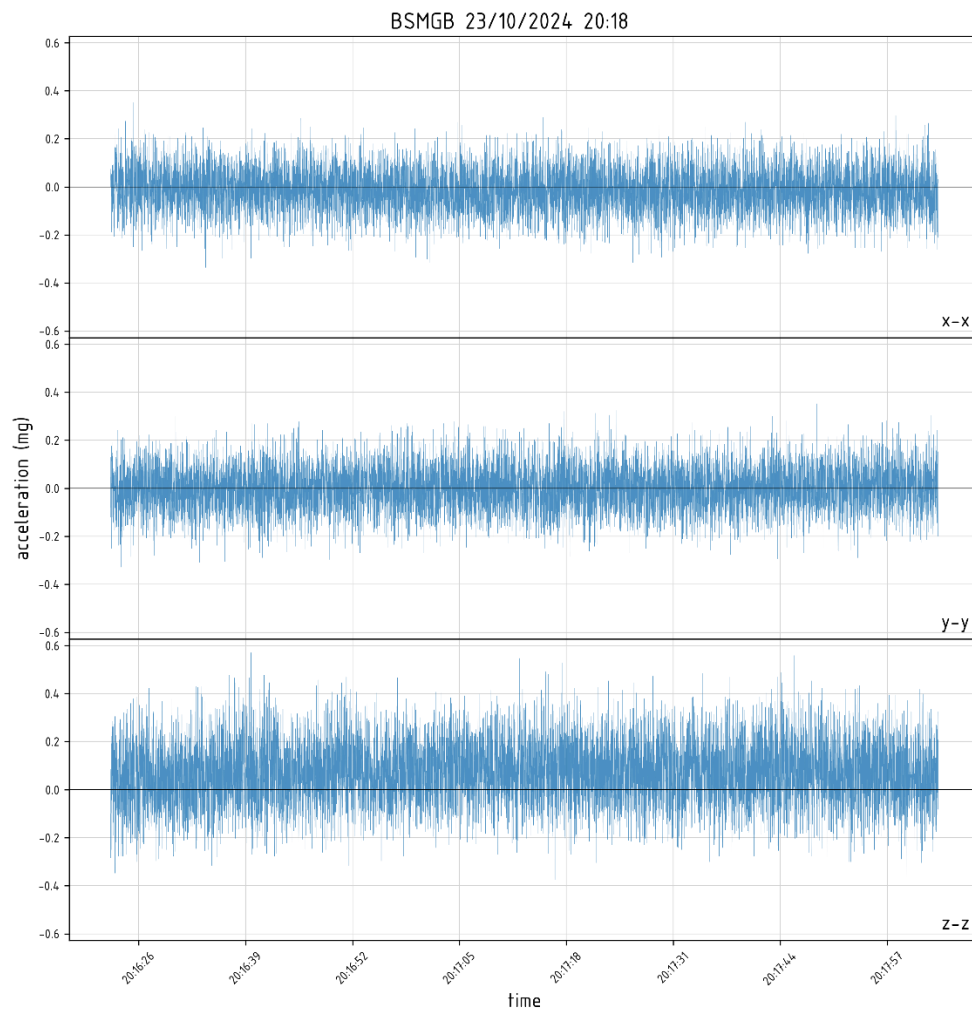


Figure 7. Remotely recorded acceleration stream from an established station/terminal script.



**Figure 8.** Remotely recorded acceleration stream from an established station / triaxial accelerogram.

### **(b) Testing**

To assess the reliability of the Low Cost Accelerometer (Seismobug v3.0) a testing procedure has been designed and implemented in the framework of the project. Specifically, two commercially available broad-band accelerometers were chosen as reference recorders, namely a Guralp CMG-5TD installed in Thessaloniki and a Force Balanced Episensor of Kinemetrics coupled with a 24bits Digitizer Centaur of Nanometrics installed in Kefalonia, Greece. At the same sites a Seismobug was installed for a period of about 11 months to record local or/and regional earthquakes. For the case of Thessaloniki being in the zone of moderate seismicity no significant events were recorded. To the contrary for the case of Kefalonia that is the highest seismicity region in Greece and in Europe, 97 earthquakes were recorded, with magnitudes  $1.8 < M < 4.5$ , in both accelerometers (BB Episensor and Seismobug v3.0), offering a valuable dataset for comparison between the two

accelerometers and testing of the Seismobug with respect to FB Episensor. Results of the comparison are presented in the following.

For the examined time period of almost 11 months (30/06/2023 - 16/05/2024), the low-cost Next Generation Accelerometer (NGA-LC) (SeismoBug), was kept installed very close (practically, at the same position) to the high-cost accelerometer (which from now on is going to be called as “CK0”), belonging to the permanent Argostoli Vertical Array network (ARGONET, ITSAK et al., 2015, Theodoulidis et al., 2018). This high-cost accelerometer corresponds to a force balance Episensor (Kinematics), of high broad-band frequency range (DC-200 Hz), equipped with a 24-bit digitizer.

During these 11-months, time-period, 97 earthquakes occurred mainly in western Greece. These earthquakes were analyzed together with the already recorded to the previous examined period (01/05/2024 and 30/06/2024) 30 earthquakes (Figure 9a).

These 97 in total, earthquake events, were simultaneously recorded by both the two accelerometers (the low cost “SeismoBug” and the higher cost, “CK0-ARGONet” broad-band one). The local magnitude,  $M_L$  of these 97 earthquakes range from 1.5 to 4.4, according to the catalogue of Geodynamic Institute of the National Observatory of Athens (G.I. - NOA, <https://bbnet.gein.noa.gr/HL/>), while they are characterized as shallow earthquakes with depths lower than 30 km (Table 1). The epicentral distances of these earthquakes with respect to the Argonet location where both the two examined instruments are installed, range between ~3 km and ~161 km (Figure 9b), while the corresponding PGAs recorded by the permanent installed CK0 “reference” accelerometer, range from a minimum of ~0.08 mg, up to a maximum of ~154 mg (Figure 9c). It’s worth noting that this maximum recorded PGA corresponds to the N-S component record of an  $M_L$ -4.1 earthquake, at ~16.4 km depth, in ~ 9.2 km epicentral distance from the Argonet location.

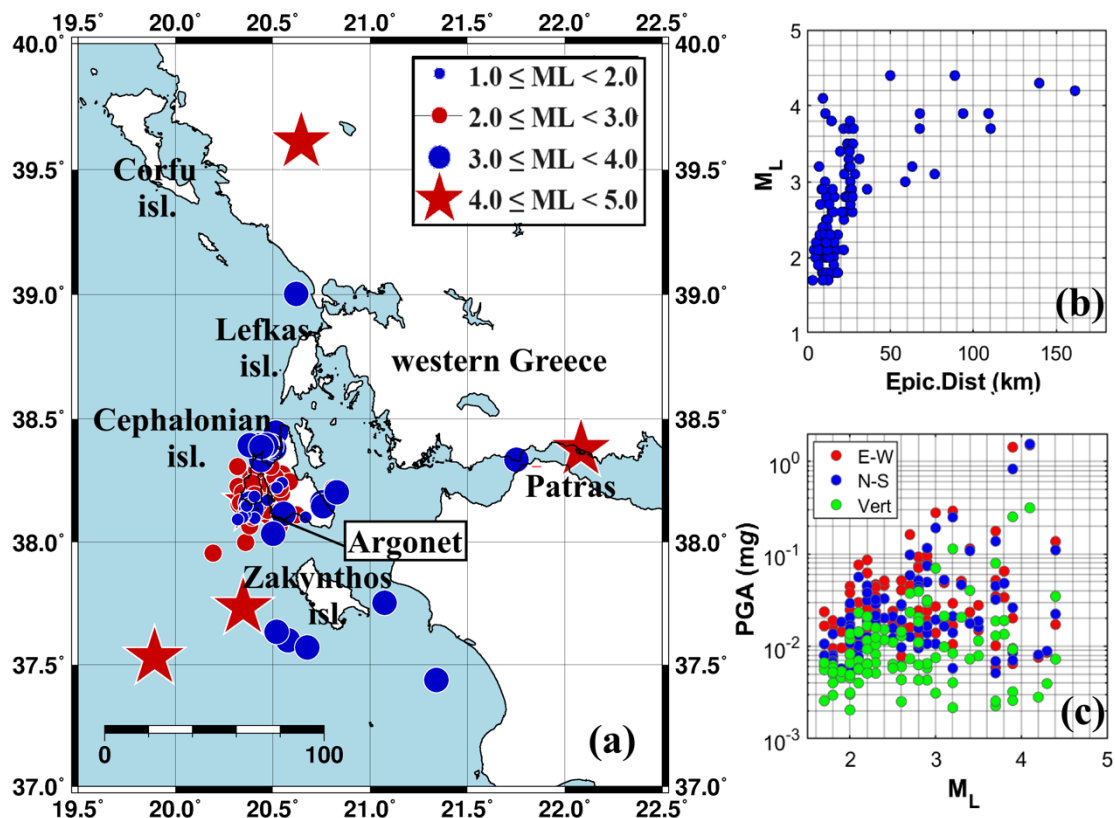


**Figure 9.** (a) The 97 earthquake epicenters in western Greece area and the Argonet location in Cephalonian island. (b) and (c) The local magnitude,  $M_L$ , of these 97 earthquakes, vs their epicentral distance from the Argonet and vs the corresponding PGA, of the two horizontal (E-W and N-S) and the Vertical components.

In order to evaluate the recording reliability level of the low-cost Next Generation Accelerometers (NGA-LC) (**SeismoBug**), all the three component records (EW, NS, Vertical-Z) of both the two examined accelerometers (the low cost “**SeismoBug**” and the higher cost, “**CK0-ARGOnet**” broad-band one), of the 97 (in total) examined earthquakes (Figure 9a), were firstly visually separately inspected. More specifically the total seismic record (including the pre-event noise, the body P- and S- wave part, as well as several tens of seconds after them), and separately the S-wave part, which correspond to the main earthquake energy, were visually inspected based on Appendix A. The S-wave motion window was separately detected at each earthquake record, starting from the manually picked S-wave arrival, and ending to a time proportional to the epicentral distance ( $0.1 \times \text{Epic. Dist}(km)$ , plus 0.5 sec, as an average Seismic Source duration for all the Events), according to **Kishida et al. (2016)**.

It’s worth noting that to all the examined seismic records of each earthquake for the two accelerometers (**Appendix A**), a detrend function was first

applied for the baseline correction. Moreover, a Bandpass Butterworth filter of 4<sup>th</sup> order between 0.05 Hz and 50Hz was also applied to each record, carrying for the low energy noise effects below the low frequency reliability limit of the instruments (~0.05 Hz), as well as for the higher reliability limit related to the Nyquist frequency (~50 Hz) of these records.

Moreover, the RMS and Peak-to-Peak (P-P) quantities of the noise records selected at each component, of all the 97 examined waveforms, have been determined here. In Figure 10a, the 97 RMS values are presented for each component separately (red, blue and green for the EW, NS and V component, respectively), while their average values have been also computed. The average RMS level is ~0.073 mg ( $\pm 0.003$ ) and ~0.114 mg ( $\pm 0.006$ ), for the Horizontal and Vertical components, respectively. The corresponding average P-P values are equal to ~0.49 ( $\pm 0.06$ ) and ~0.76 mg ( $\pm 0.08$ ), respectively.

It is denoted that the average RMS and P-P values do not correspond to natural ambient local noise, but to the “inherent” instrument (SeismoBug) noise, since it is relevantly quite higher than the corresponding one recorded by the comparable higher-resolution and cost Episensor (CK0). Moreover, it’s worth noting that the average RMS values computed here are comparable to the corresponding measured values of the examined instruments on laboratory conditions (RMS ~0.089 and 0.13 for the Horizontal and Vertical component, respectively).

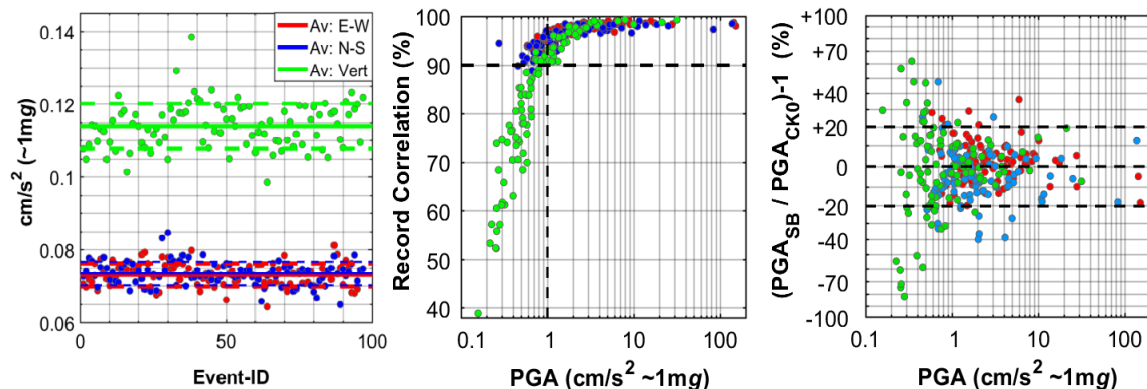


**Figure 10.** (a) The RMS of the 97 noise records, are presented for each component separately (red, blue and green for the EW, NS and Vertical component, respectively). Their corresponding average and STD values are also presented in solid and dashed lines (b) The correlation (%) of each one of the 97 S-wave motion record of each component (Appendix A), between the SeismoBug and the CK0 accelerometers vs the PGA detected in the CK0 (c) The ratio between all the PGA detected from SeismoBug and CK0 accelerometers, vs the PGA detected in the CK0.

Thereafter, the corresponding Fourier Amplitude Spectra (FAS) of both the Total and the S-wave part seismic record (Appendix A), were also visually inspected in Appendix B. Regarding the separately computed S-wave FAS, only the reliable considered values (per frequency) under a Signal-to-Noise Ratio (SNR) greater than 5, are presented. The pre-event noise of each record was considered as the noise used for the SNR process.

In Figure 10b, the cross correlation (%) of the S-wave motion record between the two examined accelerometers (SeismoBug and CK0) for each component and of each earthquake, is presented, in comparison to the PGA measured from the reference accelerometer, CK0. What is firstly observed from this figure is that when the real (reference) PGA, recorder by CK0 station is higher than ~1 mg, the correlation of the S-wave seismic motion recorded from SeismoBug to the one recorded by CK0 is more than 90 %. Moreover, it is also observed that the higher the PGA, the higher the correlation of the intense S-wave seismic motion. For example, for real PGA greater than ~2.0 mg, the correlation is greater than 95.5%, while for PGA greater than 3 mg, the correlation is greater than ~96.5% and is stabilized to ~ 98.7 % (~98-99.5 %) for PGA greater than 10 mg.

In Figure 10c, a comparison between the recorded PGAs of the 97 examined earthquakes from the Seismobug with the reference CK0 reference accelerometer is presented in order to investigate the efficiency of the examined Seismobug accelerometer to “detect” the real PGA of a potential earthquake. What is observed from this figure is that for real PGA > 6 mg, separately recorded in each component (EW, NS and Vertical) by the CK0 reference accelerometer, the recorded PGA from the examined accelerometer (SeismoBug) is similar to the one recorded from the reference one (i.e. the CK0). The maximum difference can reach up to a maximum of 20% between the two PGA (the real and the recorded one from the SeismoBug) (Figure 10c). The same is also for PGA > 1 mg, where however few records present PGA differences up to ~40%.

Based on the above observations it can be concluded that the examined low-cost accelerometer (SeismoBug) can satisfactorily capture the real ground motion when this is higher than the dominant noise level, as well as when the characteristic Peak value (PGA) can be greater than ~6 mg, that is it fulfills ground motion recording of engineering interest.

*Earthquake Resilient Schools - EReS [BSB 966]*  
*Project Nr: 101101206 (UCPM-2022-PP)*  
*Deliverable D4.1: Investigation of seismic risk indicators based on instrumentation of school buildings in the selected pilot sites*

---

**Table 1.** The information (Date-Time, Longitude, Latitude, Depth, Local Magnitude) from the 97 Events (earthquakes) used in this study (Figure 1), provided by Geodynamic Institute catalogues (<https://bbnet.gein.noa.gr/HL/>).

	YYYY/MM/DD_hh:mm:ss	Long.	Lat.	Depth (km)	ML
1	2023/04/13_21:23:40.910	21.0741	37.7531	27.4	3.7
2	2023/04/14_09:06:36.780	20.3865	38.2594	13.1	2.2
3	2023/04/15_14:57:26.500	20.5476	38.2768	18.1	2.3
4	2023/04/19_03:52:38.970	21.3405	37.4373	15.7	3.9
5	2023/04/22_12:03:03.480	20.3215	38.2265	16.9	2.1
6	2023/04/29_01:20:56.830	20.6685	38.101	17.3	1.8
7	2023/04/29_18:02:57.520	22.0834	38.3762	12.6	4.3
8	2023/05/01_15:06:03.430	20.6461	39.6103	6.6	4.2
9	2023/05/06_22:20:39.640	20.5156	38.4444	16.9	3.3
10	2023/05/08_04:53:10.960	19.8926	37.5293	8.5	4.4
11	2023/05/12_23:01:04.990	20.5783	37.5998	12.1	3.2
12	2023/05/15_10:39:48.370	20.3865	38.1578	16.4	3
13	2023/05/15_13:10:07.420	20.3448	38.2013	4.7	2.6
14	2023/05/22_16:49:19.340	20.1933	37.9555	6.3	2.9
15	2023/05/23_08:49:16.370	20.5394	38.2393	11.2	1.8
16	2023/05/23_09:48:04.320	20.5472	38.2407	16.7	1.8
17	2023/05/23_09:52:07.750	20.5412	38.2466	6.6	2
18	2023/05/23_12:43:05.010	20.533	38.2375	18.3	2.9
19	2023/05/27_06:19:21.300	20.5325	38.0649	20.6	2.5
20	2023/05/27_15:49:29.770	21.7516	38.3345	10.9	3.7
21	2023/05/31_02:14:03.600	20.3746	38.1056	18.3	2
22	2023/05/31_02:17:28.260	20.3755	38.0928	14.8	2.3
23	2023/06/05_21:17:49.730	20.3677	38.1693	11.1	2.5
24	2023/06/05_22:22:24.670	20.3439	38.1619	11	2.2
25	2023/06/18_18:29:38.990	20.5197	37.6346	12.4	3
26	2023/06/19_17:03:46.990	20.4424	38.2274	14.7	2.1
27	2023/06/22_02:17:35.450	20.3604	37.999	13.7	2.6
28	2023/06/23_10:56:21.710	20.62	39.0028	17	3.9
29	2023/06/28_18:47:14.700	20.392	38.0946	18.1	2.3

*Earthquake Resilient Schools - EReS [BSB 966]*

*Project Nr: 101101206 (UCPM-2022-PP)*

*Deliverable D4.1: Investigation of seismic risk indicators based on instrumentation of school buildings in the selected pilot sites*

	YYYY/MM/DD_hh:mm:ss	Long.	Lat.	Depth (km)	ML
30	2023/06/29_11:10:32.940	20.4616	38.1651	17.6	2.1
31	2023/07/07_12:56:21.210	20.4401	38.3331	9.5	3.4
32	2023/07/19_03:59:08.030	20.4066	38.0974	18.1	1.8
33	2023/07/20_12:20:13.010	20.3879	38.129	10	2.2
34	2023/07/23_05:52:05.300	20.5559	38.1157	16.1	3.2
35	2023/07/30_20:06:58.470	20.381	38.0663	15.5	2.6
36	2023/08/10_16:46:26.480	20.3275	38.1528	16	2
37	2023/08/11_03:52:53.370	20.5852	38.2457	15.6	2.8
38	2023/08/18_06:32:48.000	20.4167	38.2915	10.5	2.8
39	2023/08/23_18:16:27.760	20.5119	38.264	15.7	2.1
40	2023/08/27_09:48:57.990	20.3348	38.1601	13.3	2.9
41	2023/08/30_04:36:07.420	20.6209	38.1111	17.3	2.2
42	2023/09/02_02:06:14.710	20.4506	38.134	15.7	2.2
43	2023/09/09_02:32:27.390	20.4263	38.3505	11.7	2.5
44	2023/09/19_03:24:08.210	20.3572	38.112	18	1.8
45	2023/09/19_05:10:37.080	20.3444	38.101	16.2	1.9
46	2023/09/19_08:49:43.760	20.5138	38.2072	16.1	2
47	2023/09/21_07:00:51.040	20.7545	38.1624	15.2	3.7
48	2023/09/21_09:57:45.120	20.7582	38.1459	16.6	3.1
49	2023/10/06_10:38:40.960	20.4314	38.1276	15.2	2.7
50	2023/10/06_14:24:56.170	20.7536	38.1413	16	2.1
51	2023/10/22_15:19:48.090	20.3947	38.102	19.5	2
52	2023/10/28_05:26:58.000	20.3929	38.2402	11.4	2.7
53	2023/11/16_22:15:15.580	20.7431	38.1693	27.4	2.6
54	2023/11/19_11:42:10.700	20.8127	38.1949	20	2.6
55	2023/11/21_10:12:35.840	20.6772	37.5705	12	3.9
56	2023/11/22_07:05:48.900	20.4726	38.1706	16.8	1.7
57	2023/11/26_15:21:29.870	20.8287	38.2027	16.1	3.1
58	2023/11/30_12:39:18.760	20.3476	37.7335	9	4.4
59	2023/12/13_22:10:56.330	20.544	38.1963	21.5	2
60	2024/01/01_09:27:18.360	20.4744	38.1294	12.7	2

*Earthquake Resilient Schools - EReS [BSB 966]*

*Project Nr: 101101206 (UCPM-2022-PP)*

*Deliverable D4.1: Investigation of seismic risk indicators based on instrumentation of school buildings in the selected pilot sites*

---

	YYYY/MM/DD_hh:mm:ss	Long.	Lat.	Depth (km)	ML
61	2024/01/16_15:53:38.560	20.3815	38.1281	15.4	2.4
62	2024/01/20_16:04:09.300	20.5421	38.1267	21.1	2.2
63	2024/01/30_05:18:14.760	20.5202	38.221	12.5	1.9
64	2024/01/30_06:03:45.270	20.4044	38.1491	16.4	2.4
65	2024/01/30_14:47:05.230	20.3197	38.307	15.6	2.8
66	2024/01/31_10:42:35.310	20.424	38.1532	13.4	2.3
67	2024/02/05_23:40:59.480	20.3664	38.1477	17.6	1.7
68	2024/02/17_20:10:06.740	20.4066	38.1917	16	2.9
69	2024/02/17_21:28:28.300	20.3746	38.1743	17.6	2
70	2024/03/03_13:35:09.180	20.5069	38.3798	8.4	3.5
71	2024/03/03_23:57:17.220	20.425	38.3922	14.5	3.5
72	2024/03/04_16:49:48.540	20.4707	38.3876	13.7	3.2
73	2024/03/04_17:11:11.890	20.4922	38.389	11.3	3.7
74	2024/03/04_19:18:46.550	20.4698	38.3922	11.3	3.8
75	2024/03/04_19:34:47.250	20.4689	38.394	13.2	3
76	2024/03/05_02:53:36.010	20.4662	38.394	14.5	3.2
77	2024/03/05_17:38:26.350	20.3819	38.3931	15.5	3.7
78	2024/03/06_06:39:28.280	20.4405	38.3858	15.4	3.4
79	2024/03/06_11:34:56.990	20.4703	38.3926	17.4	2.9
80	2024/03/09_21:48:31.240	20.49	38.308	14.7	2.2
81	2024/03/09_22:25:09.000	20.5096	38.3917	9.2	2.8
82	2024/03/10_21:37:54.710	20.4245	38.3871	15.7	2.7
83	2024/03/21_05:57:13.840	20.8067	38.1972	20	2.9
84	2024/03/24_00:59:36.920	20.4414	38.3775	13.7	2.8
85	2024/03/26_00:09:01.260	20.4057	38.1853	10.5	1.7
86	2024/04/01_13:02:38.370	20.5019	38.0342	26.4	3.8
87	2024/04/04_07:00:55.010	20.4854	38.405	10.7	2.8
88	2024/04/29_11:59:51.540	20.809	38.2169	17.6	2.8
89	2024/05/07_19:50:43.420	20.5376	38.2182	17.8	2.1
90	2024/05/10_06:18:37.470	20.3714	38.1216	13.6	2
91	2024/05/10_10:48:34.020	20.3897	38.1345	10.4	3.9

	YYYY/MM/DD_hh:mm:ss	Long.	Lat.	Depth (km)	ML
92	2024/05/10_12:56:14.110	20.4012	38.156	16.4	4.1
93	2024/05/10_21:26:02.020	20.3929	38.1349	11.2	2.3
94	2024/05/11_07:45:55.570	20.3773	38.1313	18	2.1
95	2024/05/15_07:22:40.400	20.3792	38.1541	15.6	2.2
96	2024/05/15_22:13:50.400	20.3201	38.0923	15.8	1.8
97	2024/05/16_06:25:36.300	20.3618	38.1148	16.2	2.3

Two Appendices are provided to show comparisons in both time and frequency (FAS) domain of all the 97 recordings.

In **Appendix (A)** 97 pairs of 6 subplots (two lines and three columns) which correspond to the 97 examined earthquake records. In top line (subplots-[a]) of each pair of 6 subplot, the total seismic record (including the pre-event noise, the body P- and S- wave part and several tens of seconds after S-waves) of each one of the 97 earthquake records, for each component (EW, NS and Vertical, in orange, blue and green color respectively for the SeismoBug and in black lines for the CK0 accelerometer), is depicted. In bottom line (subplots-[b]), only the S-wave part of each total seismic record, is depicted (zoom in).

In **Appendix (B)**, the corresponding Fourier Amplitude Spectra (FAS) of both the Total and the S-wave part seismic record of Appendix A, for each component record of the 97 examined earthquakes, for the two accelerometers (SeismoBug and FB Episensor).

## **2.2 INSTALLATIONS IN ALEXANDROUPOLIS**

All installations in Alexandroupolis city were positioned on the ground floor and at the ceiling of the top floor in the school buildings. This setup allows for investigation of the building’s dynamic response and estimation of inter-storey drift indicators. Additionally, it enables the estimation of the building’s fundamental period. The school buildings in the pilot sites, Alexandroupolis and Samos, are typically reinforced concrete structures ranging from one to four stories, with most being three stories or fewer.

The spatial installation plan was designed to support potential ground-floor (free field like) recordings, which can enhance Shakemap coverage at the city scale by increasing the density of observation stations across Greece.

### 2.2.1 Selection of school buildings for the installations

In the municipality of Alexandroupolis, there are over 30 school units in operation. Each school unit may consist of multiple structurally independent buildings. Figure 11 presents a plan view of the city, showing the locations of all school units, with five selected units highlighted.



**Figure 11.** Existing school units in the municipality of Alexandroupolis (top), Selected 5 schools for installation of Low Cost accelerometers (bottom).

According to the geologic map (1:50,000 scale) of the broader city area (Figure 12), nearly the entire city is situated on surface geology of recent Holocene age, characterized by cays, sands, cobbles, and unconsolidated scree formations. Consequently, all five selected schools are founded on this specific geologic formation.

### 2.2.2 Installations

The following section provides a brief overview of the five instrumented school buildings, identified by their official names. Each entry includes a photograph of the building as well as images of the Low-Cost Accelerometer installations on both the ground floor and ceiling. As planned, a total of 10 Low-Cost Accelerometers were successfully installed in Alexandroupolis.



Figure 12. Geologic map of the broader area of the city of Alexandroupolis together with the 5 selected school units (1:50.000 scale, IGME maps, <https://www.eagme.gr/site/services>). The ITSAK permanent accelerometer station is also shown as ALX1.

(a) 2<sup>nd</sup> EPAL-School building



Figure 13. Alexandroupolis 2nd EPAL building instrumented in ground floor and top ceiling.

(b) 4<sup>th</sup> High-School building



(a)



(b)

Figure 14. (a) Alexandroupolis 4<sup>th</sup> high school building instrumented in ground floor and top ceiling (b) Plans of the ground floor and upper floor.

(c) 3<sup>rd</sup> High-School building



Figure 15. Alexandroupolis 3<sup>rd</sup> high school building instrumented in ground floor and top ceiling.

(d) 5<sup>th</sup> High-School building



Figure 16. Alexandroupolis 5<sup>th</sup> high school building instrumented in ground floor and top ceiling.

(e) 2<sup>nd</sup> High-School building



**Figure 17.** Alexandroupolis 2<sup>nd</sup> high school building instrumented in ground floor and top ceiling.

Data streaming from all five school buildings has been successfully acquired, with local observers contributing to the resolution of in-situ operational issues. The viability of the network in Alexandroupolis can be ensured through close collaboration with the Directorate of Education. Additionally, the installed accelerometer stations, can serve as valuable tools for training and raising awareness within the school communities, in the future.

## 2.3 INSTALLATIONS IN SAMOS

### 2.3.1 Selection of school buildings for the installations

In the municipality of Vathy-Samos, over 15 school units are currently in operation. Each school unit may consist of multiple structurally independent buildings. Figure 18 provides a plan view of the city, illustrating all existing school units, with five selected units highlighted.



**Figure 18.** Existing school units in the municipality of Vathy-Samos (top), selected 5 schools for installation of Low Cost accelerometers (bottom).

According to the geological map of the broader city area (1:50,000 scale), as shown in (Figure 19), nearly the entire city is situated on three geological formations: Quaternary-Holocene scree and talus cones, Paleozoic marble, and Neogene-Miocene travertine-like limestones. As a result, three of the five school buildings are located within the Quaternary-Holocene formations, one is at the boundary of these formations and the Neogene-Miocene travertine-like limestones, and the fifth is on the Paleozoic marble, which can be considered a "rock" reference site.

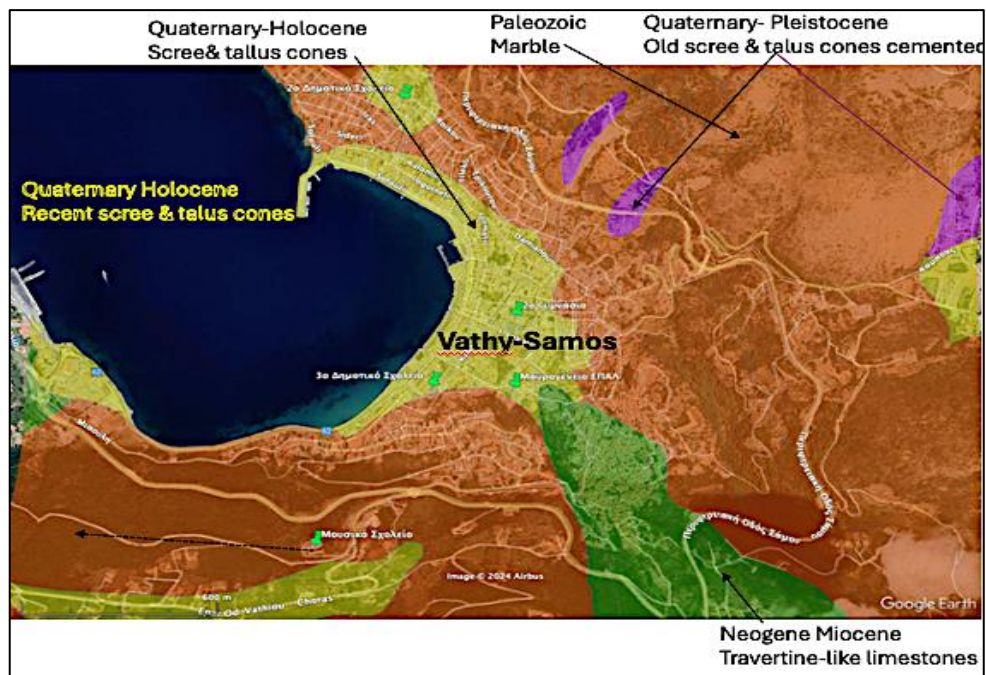


Figure 19. Geologic map of the broader area of the town of Vathy-Samos (1:50.000 scale, IGME maps, <https://www.eagme.gr/site/services>) together with the 5 selected school units.

### 2.3.2 Installations

The following section provides a brief overview of the five instrumented school buildings, identified by their official names. Each entry includes a photograph of the building, along with images of the Low-Cost Accelerometer installations on both the ground floor and ceiling. As planned, a total of 10 Low-Cost Accelerometers were successfully installed in Vathy-Samos.



Figure 20. Vathy-Samos “Mavrogeneio“ EPAL building instrumented in ground floor, middle floor and top ceiling.



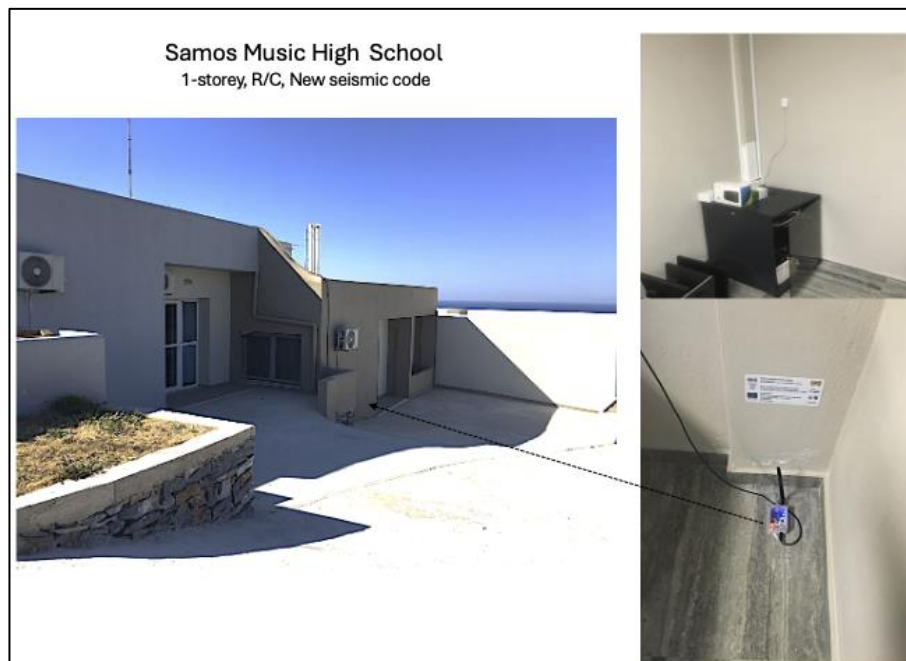
Figure 21. Vathy-Samos 2<sup>nd</sup> high school building instrumented in ground floor and top ceiling.



Figure 22. Vathy-Samos 2<sup>nd</sup> Exp. Elementary school building instrumented in ground floor and top ceiling.



**Figure 23.** Vathy-Samos 3<sup>rd</sup> Elementary school building instrumented in ground floor and top ceiling.



**Figure 24.** Vathy-Samos Music high school building instrumented in ground floor (reference rock station)

### 3 INSTRUMENTATION OF SCHOOL BUILDINGS IN THE TURKISH PILOT SITES

#### 3.1 TECHNICAL SPECIFICATION OF NEXT GENERATION ACCELEROMETERS

The SH-HPAS series sensors (High Precision Accelerometer Sensors), manufactured by StructHEALTH, are highly precise three-axis accelerometers designed for a variety of applications, including seismic monitoring, structural health assessment, vibration monitoring, vibration testing, and human comfort and acceleration monitoring (<https://structhealth.com/>).

The S-TEK HPAS V3 sensor is an all-in-one solution that allows for the direct transfer of three-axis acceleration and inclination data to a PC via Ethernet.

The technical specifications for the acceleration and inclination sensors, along with additional specifications, are provided below:

##### **Acceleration Information:**

- Two separate mems measurement - hybrid technology
  - Excellent long-term stability with hermetic mems structure
  - 3 axis acceleration measurement (X-Y-Z)
  - Very low noise level (1  $\mu\text{g}/\text{Hz}$ ) ( $\pm 2\text{g}$  measurements)
- < 1 $\mu\text{g}$  RMS DC level noise
- $\pm 2\text{g}$  /  $\pm 4\text{g}$  /  $\pm 8\text{g}$  measurement range (User programmable)

Optional upto  $\pm 20\text{g}$  in high frequency version

- 24-bit sampling, Non-linearity  $\pm 0.1\%$  FS
- 100 / 200 / 400 sps data transfer (User programmable)

Optional 64 ksps in high frequency version

- Lowpass and highpass digital filters
- Frequency response: DC to 500 Hz, \*Optional up to 20 KHz  
Optional additional precision geophone support \*

##### **Inclination Information:**

- 2 axis inclination measurement (Roll - Pitch)
- Angle output resolution  $0.0055^\circ/\text{LSB}$
- Ultra-low  $0.001^\circ/\text{Hz}$  noise density
- Proven capacitive 3D-MEMS technology
- $\pm 3^\circ$  &  $\pm 90^\circ$  Measurement Range Modes

##### **Communication & Other Interfaces:**

- 100 Mbit ETH interface, POE, \*Optional GSM, \*Optional GPS
- CAN, RS422 or RS232 serial communication (256 kbps or 512 kbps)

**Other Features:**

- Self Test feature, Temperature Sensor, Optional adjustable relay alarm output
- Time synchronization input in multiple sensors recording. (1ms resolution)
- Ethernet network offline time synchronization feature
- 5-30V DC industrial power input and power input protection, POE
- Internal flash for 120 seconds internal earthquake recordings,
- Optional USB external flash
- IP67 plastic case, Working temperature: -40 / + 80 C - Storage temperature: -40 / +85 C

### 3.2 INSTALLATIONS IN IZMIR

The installation of accelerometers in structural health monitoring systems is a critical step in monitoring and analyzing the dynamic behavior of structures. First, strategic points where accelerometers will be placed must be determined. These points are usually selected as the areas where the vibrations of the structure are felt the most or that best represent the structural integrity of the structure.

Before installation, the calibration of the accelerometers must be performed, and the sensitivity of the devices must be checked. Accelerometers are usually mounted tightly to the surface of the structure and a solid connection is established so that they can measure vibrations accurately. In addition, cabling and data acquisition systems must be designed to transmit the signals from the accelerometers without interruption.

Finally, appropriate software is used for data analysis to evaluate the collected data and obtain information about the health status of the structure. This process enables continuous monitoring and analysis to increase the safety and durability of structures.

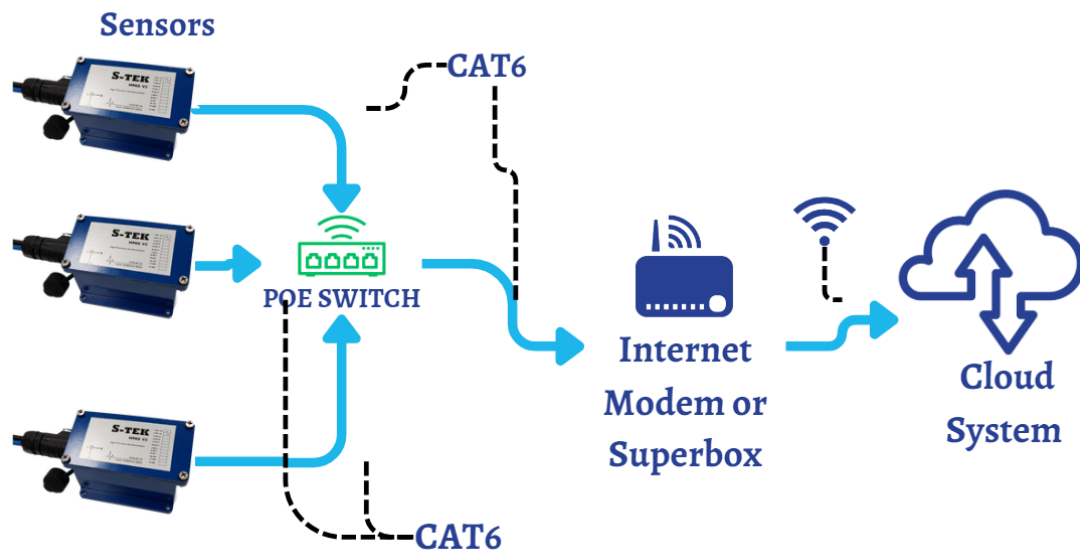


Figure 25. Working Principle of Structural Health Monitoring

#### Healthy Structures Building Health Monitoring Platform:

It is an end-to-end Structural health monitoring service where data obtained from Structhealth sensors are transferred to the cloud system via the internet.

### 3.2.1 Selection of school buildings for the installations

The list of the school buildings located in İzmir province were given in the D3.1 deliverable. The updated list and statistical distribution of the school buildings are given in D3.2 deliverable. Six of the school buildings have been selected as the pilot schools to be instrumented with the NGA devices. The distribution of the pilot schools is presented in Figure 26.

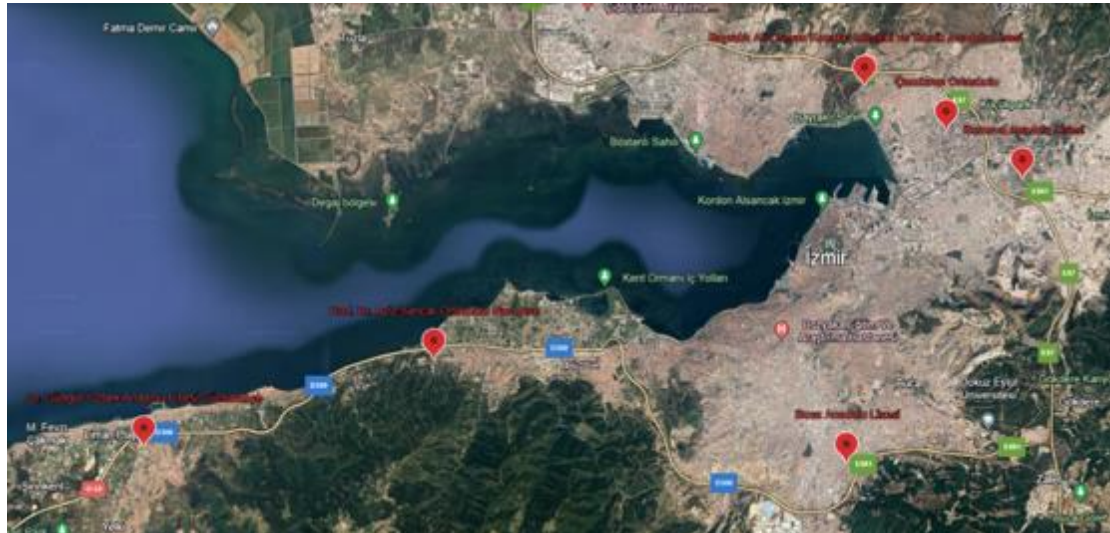


Figure 26. Geographical distribution of the pilot schools with different soil conditions in İzmir province.

Table 2 tabulates the general characteristics of the pilot schools in İzmir. The google map view, geographical coordinates and photo of the building taken during the site investigation were also presented in D3.2 deliverable.

Table 2. Schools selected in the first stage in İzmir province.

School Name	District	Construction Year	Structural System	# of Stories	Geology
Ali Osman Konakçı Mesleki ve Teknik Anadolu Lisesi	Bayraklı	2011	RC-MF-w-SW	3 (B+Z+2N)	Agglomerate
Çamkırın OrtaOkulu	Bayraklı	2023	RC-MF-w-SW	4 (B+Z+3N)	Alluvium
Bornova Anadolu Lisesi - G-Blok	Bornova	2015	RC-MF-w-SW	3(B+Z+2N)	Alluvium
Buca Anadolu Lisesi	Buca	2011	RC-MF-w-SW		Limestone
Prof. Dr. Aziz Sancar Ortaokulu	Narlıdere	2011	RC-MF-w-SW	3 (B+Z+2N)	Sandstone-Mudstone-Limestone
Dr.Güngör Özbek Anadolu Lisesi	Güzelbahçe	2015	RC-MF-w-SW	3 (B+Z+2N)	Gravel

### 3.2.2 Installations

#### i. Ali Osman Konakçı Mesleki ve Teknik Anadolu Lisesi



Figure 27. Ali Osman Konakçı Mesleki ve Teknik Anadolu Lisesi 3<sup>rd</sup> Floor Accelerometer Location (Instrumentation).



Figure 28. Ali Osman Konakçı Mesleki ve Teknik Anadolu Lisesi Basement Floor Accelerometer Location (Instrumentation).

ii. **Çamkiran Ortaokulu Bayraklı**



Figure 29. Çamkiran Ortaokulu Bayraklı 3<sup>rd</sup> Floor Accelerometer Location (Instrumentation).



Figure 30. Çamkiran Ortaokulu Bayraklı Basement Floor Accelerometer Location (Instrumentation).

iii. **Bornova Anadolu Lisesi- G Blok**



**Figure 31.** Bornova Anadolu Lisesi G-Blok 2<sup>nd</sup> Floor Accelerometer Location (Instrumentation).



**Figure 32.** Bornova Anadolu Lisesi G-Blok Basement Floor Accelerometer Location (Instrumentation).

**iv. Buca Anadolu Lisesi**



**Figure 33.** Buca Anadolu Lisesi 2<sup>nd</sup> Floor Accelerometer Location (Instrumentation).



**Figure 34.** Buca Anadolu Lisesi Basement Floor Accelerometer Location (Instrumentation).

v. **Prof. Dr. Aziz Sancar Ortaokulu**



**Figure 35.** Prof. Dr. Aziz Sancar Ortaokulu 3<sup>rd</sup> Floor Accelerometer Location (Instrumentation).



**Figure 36.** Prof. Dr. Aziz Sancar Ortaokulu Basement Floor Accelerometer Location (Instrumentation).

**vi. Dr. Güngör Özbek Anadolu Lisesi**



**Figure 37.** Dr. Güngör Özbek Anadolu Lisesi 2<sup>nd</sup> Floor Accelerometer Location (Instrumentation).

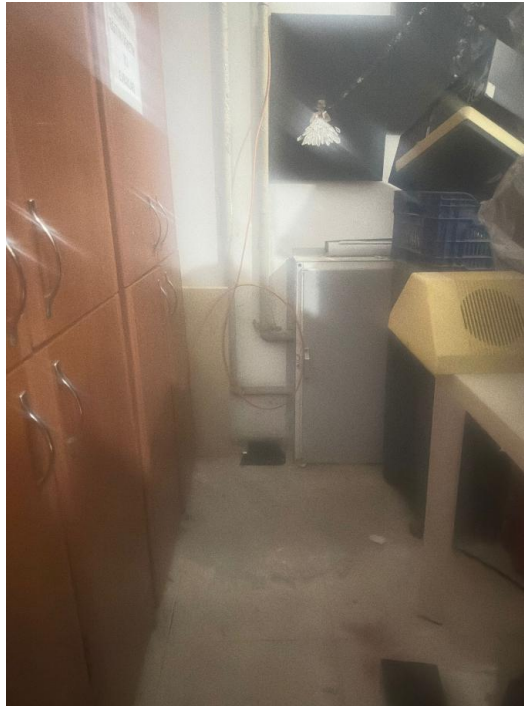


**Figure 38.** Dr. Güngör Özbek Anadolu Lisesi Basement Floor Accelerometer Location (Instrumentation).

### 3.3 INSTALLATIONS IN ÇANAKKALE

#### 3.3.1 Selection of school buildings for the installations

The list of the school buildings located in Çanakkale province were given in the D3.1 deliverable. The updated list and statistical distribution of the school buildings are given in deliverable D3.2. Six of the school buildings have been selected as the pilot schools to be instrumented with the NGA devices. The distribution of the pilot schools is presented in Figure 39.

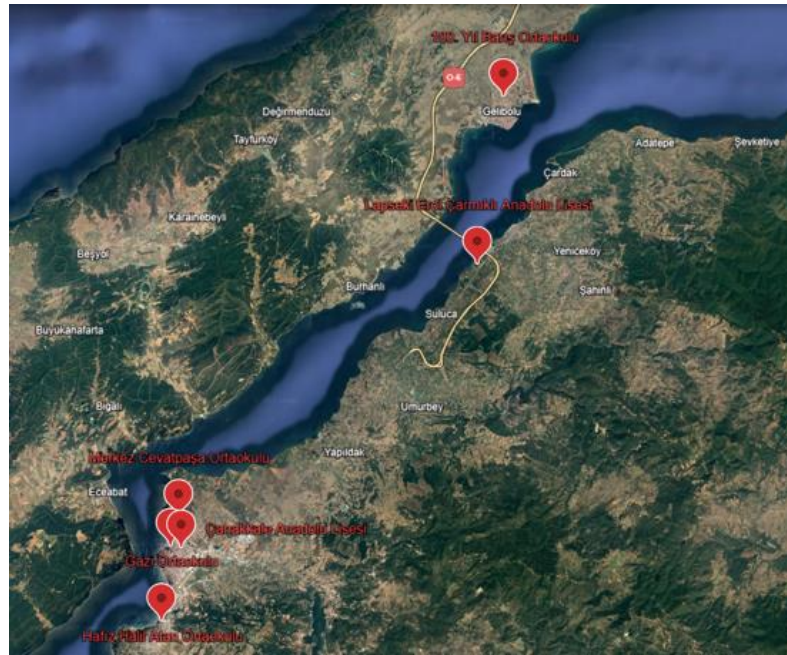


Figure 39. Geographical distribution of the pilot schools with different soil conditions in Çanakkale province.

Table 3 tabulates the general characteristics of the pilot schools in Çanakkale. The google map view, geographical coordinates and photo of the building taken during the site investigation were also presented in D3.2 deliverable.

Table 3. Schools selected in the first stage in Çanakkale province.

School Name	District	Construction Year	Structural System	# of Stories	Geology
Gelibolu 100.Yıl Barış OrtaOkulu	Gelibolu	2015	RC-MF-w-SW	3	Claystone
Lapseki Erol Çarmıklı Anadolu Lisesi	LAPSEKİ	2021	RC-MF-w-SW	4	Sandstone-Mudstone-Limestone
Merkez Cevat Paşa OrtaOkulu	Merkez	2011	RC-MF-w-SW	4	Gravel-Sandstone-Mudstone
Gazi OrtaOkulu	Merkez	2022	RC-MF-w-SW	2	Alluvium

School Name	District	Construction Year	Structural System	# of Stories	Geology
Çanakkale Anadolu Lisesi	Merkez	1982	RC-Infill Wall	4	Alluvium
Kepez Hafız Halil Atan Ortaokul	Kepez	2018	RC-MF-w-SW	3	Alluvium - Gravel-Sandstone-Mudstone

### 3.3.2 Installations

#### i. Gelibolu 100. Yıl Barış Ortaokulu

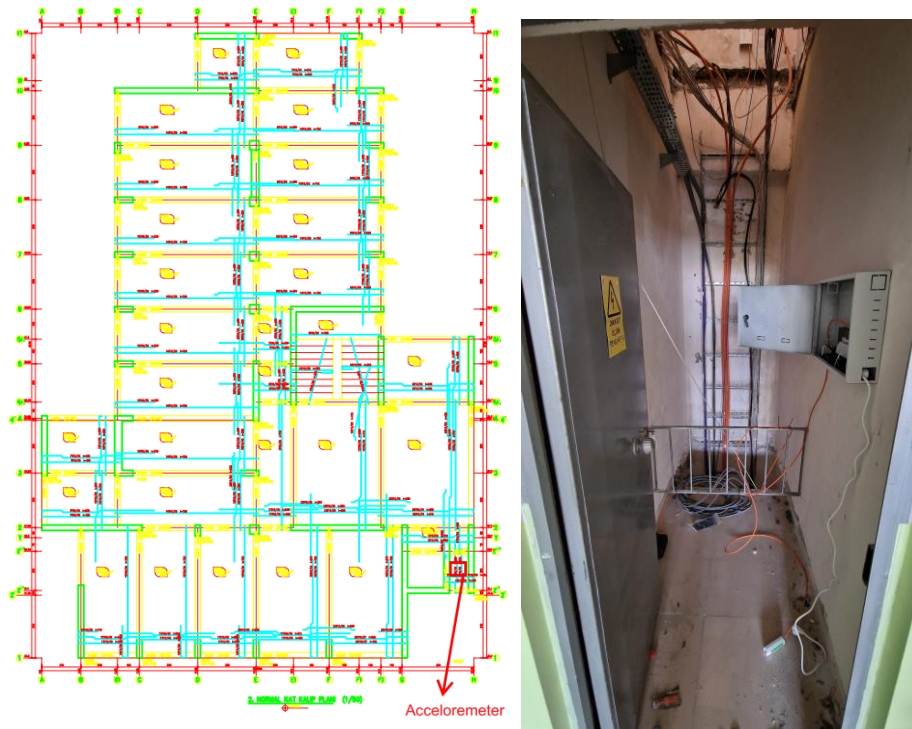


Figure 40. Gelibolu 100. Yıl Barış Ortaokulu 3<sup>rd</sup> Floor Accelerometer Location (floor plan (left), instrumentation (right)).



Figure 41. Gelibolu 100. Yıl Barış Ortaokulu Basement Floor Accelerometer Location (floor plan (left), instrumentation (right)).

ii. Lapseki Erol Çarmıklı Anadolu Lisesi

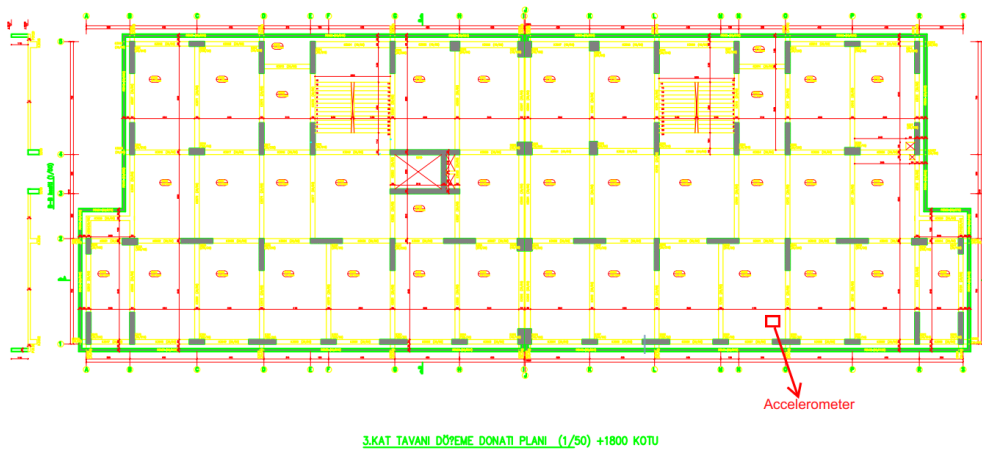




Figure 42. Lapseki Erol Çarmıklı Anadolu Lisesi 3<sup>rd</sup> Floor Accelerometer Location (floor plan (top), instrumentation (bottom)).

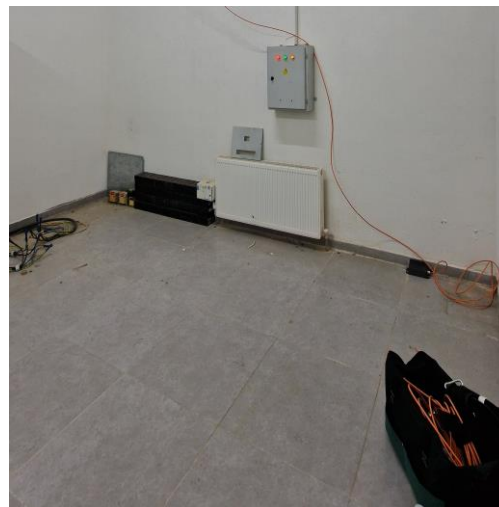
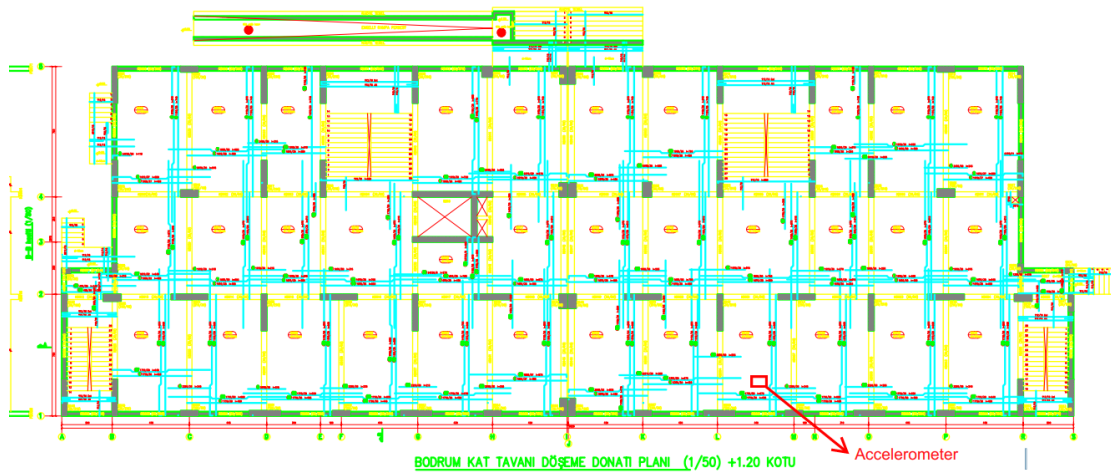


Figure 43. Lapseki Erol Çarmıklı Anadolu Lisesi Basement Floor Accelerometer Location (floor plan (top), instrumentation (bottom)).

**iii. Cevatpaşa Ortaokulu**



**Figure 44.** Cevatpaşa Ortaokulu 2<sup>nd</sup> Floor Accelerometer Location (Instrumentation).



**Figure 45.** Cevatpaşa Ortaokulu Basement Floor Accelerometer Location (Instrumentation).

iv. Gazi Ortaokulu

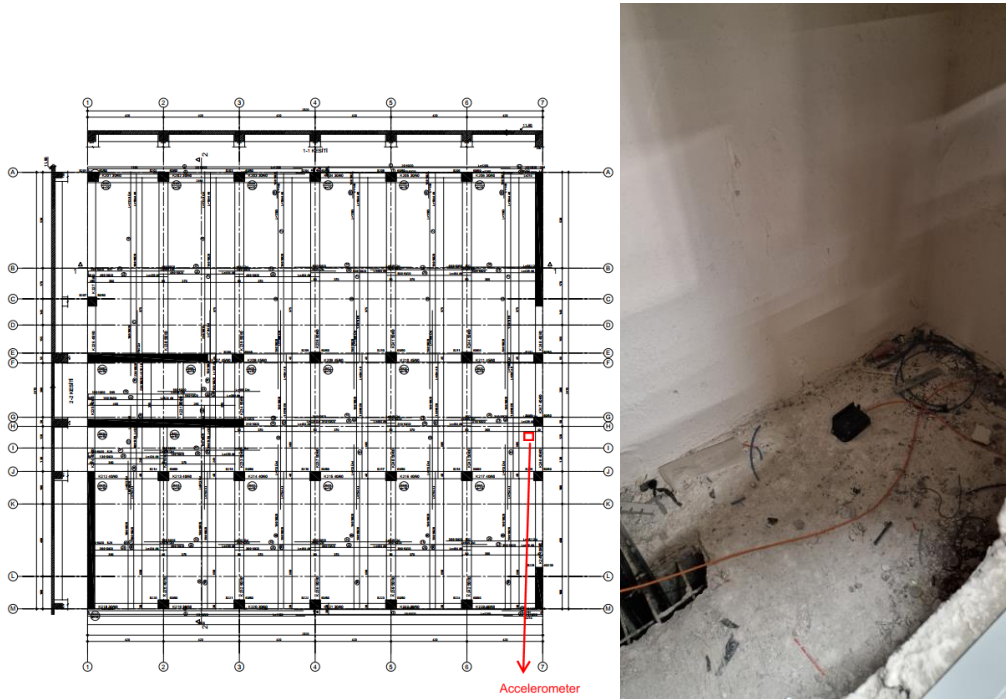


Figure 46. Gazi Ortaokulu 2<sup>nd</sup> Floor Accelerometer Location (floor plan (left), instrumentation (right)).

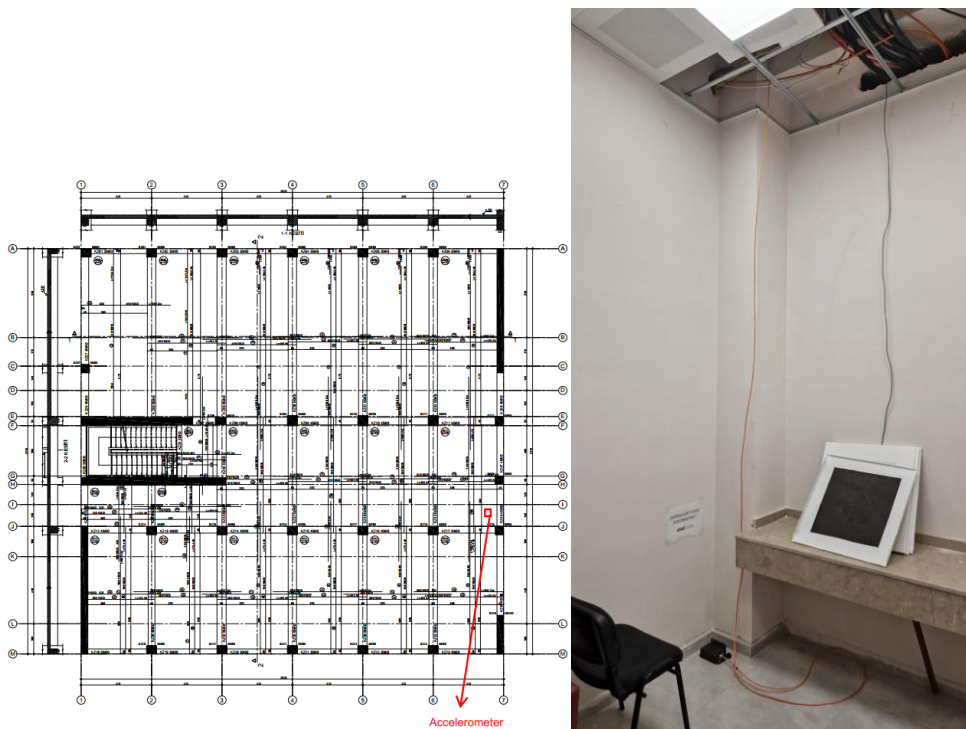


Figure 47. Gazi Ortaokulu Basement Floor Accelerometer Location (floor plan (left), instrumentation (right)).

v. **Çanakkale Anadolu Lisesi**



**Figure 48.** Çanakkale Anadolu Lisesi 2<sup>nd</sup> Floor Accelerometer Location (Instrumentation).



**Figure 49.** Çanakkale Anadolu Lisesi Basement Floor Accelerometer Location (Instrumentation).

vi. **Kepez Hafız Halil Atan Ortaokulu**

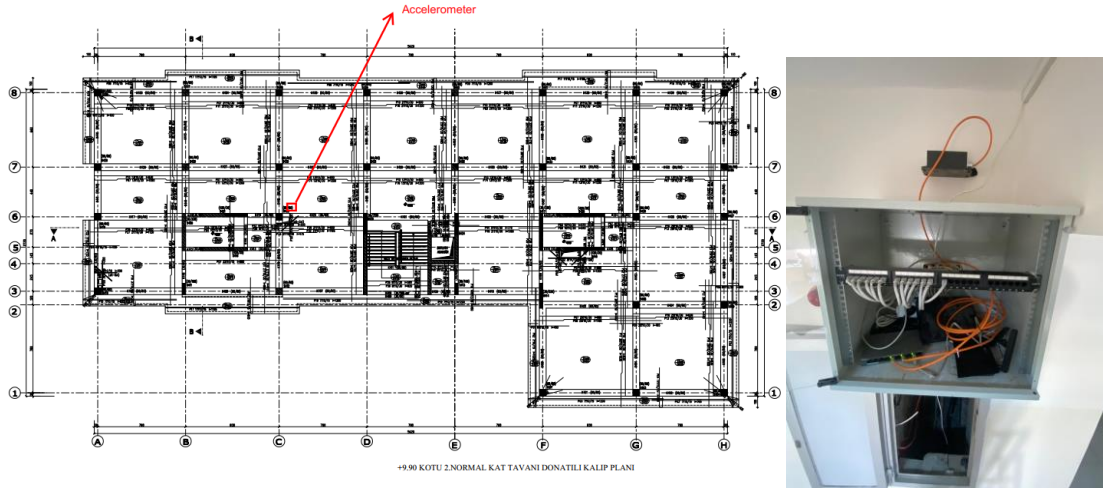


Figure 50. Kepez Hafız Halil Atan Ortaokulu 2<sup>nd</sup> Floor Accelerometer Location (floor plan (left), instrumentation (right)).

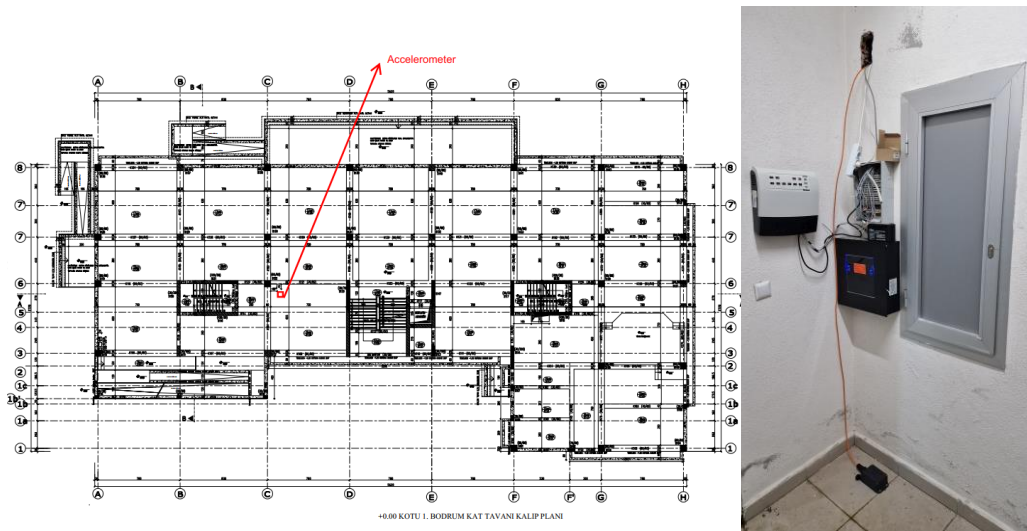


Figure 51. Kepez Hafız Halil Atan Ortaokulu Basement Floor Accelerometer Location (floor plan (left), instrumentation (right)).

## **4 INVESTIGATION OF SEISMIC RISK INDICATORS**

Having successfully installed a substantial number of accelerometers in school buildings at the selected pilot sites, as described in Sections 2 and 3, we are now able to record seismic motion in real-time during an earthquake event. The installations at the basement or ground floor of the school buildings capture the ground motion, which, when combined with appropriate fragility functions, enables estimations of expected damage. Additional installations at the top of the school buildings provide insights into the structural response during seismic events, allowing for the identification of dynamic properties as well as any potential damage.

The seismic risk indicators related to the expected damage of school buildings during a seismic event can be categorized as follows:

- Damage indicators based on the global or the interstorey drifts of the structures.
- Damage indicators reflecting the deterioration of structural properties within the inelastic range.
- Estimations of the probabilities that school buildings have exceeded the thresholds of predefined damage states, using appropriate fragility functions

The first two approaches directly address the instrumented school buildings by explicitly analyzing their seismic response. The third approach, however, adopts a more implicit method, as it uses recordings of the ground motion and combines the spectral accelerations from this motion with the fragility curves associated with the school building's typology to estimate structural damage. When a numerical model of the building is available, more detailed damage estimates can be calculated, as outlined in Section 4.3.

### **4.1 SEISMIC DAMAGE INDICATORS BASED ON THE DRIFT RATIO**

#### **4.1.1 Damage estimates based on the drift ratio level**

Global and interstorey drifts provide a direct measure of deformation, describing how much the structure moves relative to its original configuration. Global drift is used to describe the overall horizontal displacement of a building ( $\Delta_{\text{roof}}/H_b$ , Fig. 52), while interstorey drift is defined as the relative horizontal displacement between two successive floors, divided by the storey height ( $\Delta_i/h_i$ , Fig. 52).

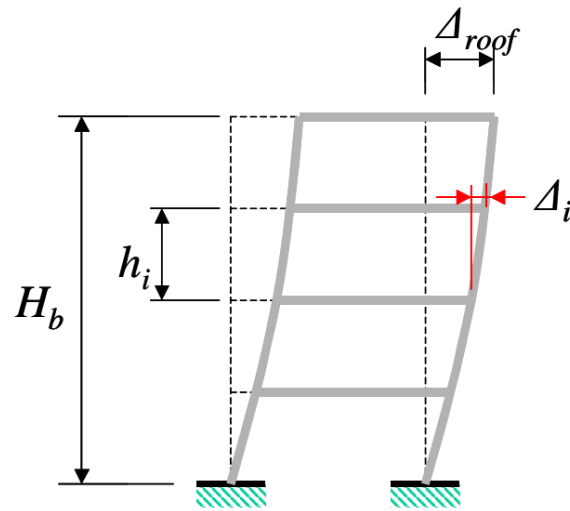


Figure 52. Roof and interstorey displacements (Su et al., 2008)

These metrics are simple, yet provide a clear link between deformation levels and different states of structural or non-structural damage. The global drift can be associated with commonly used spectral displacement-based ( $S_d$ ) fragility curves (e.g. Hazus, 2020). An example of such fragility curves as well as the typical drift ratios Used to define median values of structural damage and damage for nonstructural drift-sensitive components are presented in Figures 53 and 54)

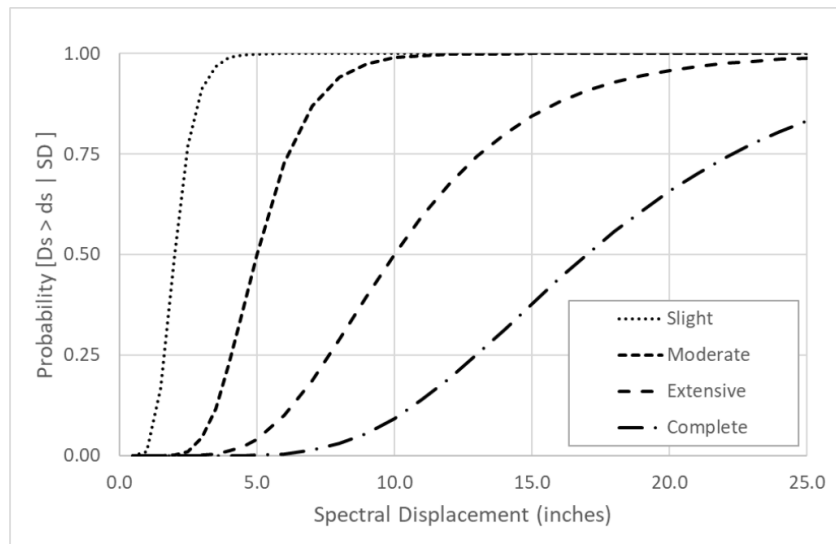


Figure 53. Example Fragility Curves for Slight, Moderate, Extensive, and Complete Damage States (Hazus 4.2 SP3, 2020)

Seismic Design Level	Building Type (Low-Rise)	Drift Ratio at the Threshold of Structural Damage			
		Slight	Moderate	Extensive	Complete
High-Code	W1/W2	0.004	0.012	0.040	0.100
	C1L, S2L	0.005	0.010	0.030	0.080
	RM1L/RM2L, PC1/PC2L	0.004	0.008	0.024	0.070
Moderate-Code	W1/W2	0.004	0.010	0.031	0.075
	C1L, S2L	0.005	0.009	0.023	0.060
	RM1L/RM2L, PC1/PC2L	0.004	0.007	0.019	0.053
Low-Code	W1/W2	0.004	0.010	0.031	0.075
	C1L, S2L	0.005	0.008	0.020	0.050
	RM1L/RM2L, PC1/PC2L	0.004	0.006	0.016	0.044
	URML, C3L, S5L	0.003	0.006	0.015	0.035
Pre-Code	W1/W2	0.003	0.008	0.025	0.060
	C1L, S2L	0.004	0.006	0.016	0.040
	RM1L/RM2L, PC1/PC2L	0.003	0.005	0.013	0.035
	URML, C3L, S5L	0.002	0.005	0.012	0.028

Drift Ratio at the Threshold of Nonstructural Damage			
Slight	Moderate	Extensive	Complete
0.004	0.008	0.025	0.050

**Figure 54.** Typical Drift Ratios Used to Define Median Values of Structural Damage (top) and Damage for Nonstructural Drift-Sensitive Components (bottom) (Hazus 4.2 SP3, 2020)

The interstorey drift (ISD) is particularly valuable because it captures how much each storey moves in relation to the adjacent ones, which is crucial for understanding the localized effects of seismic deformation. Large ISDs often lead to significant damage in non-structural elements such as partitions, facades, and even some structural components that might experience shear failures or local buckling. Figure 63 presents the ISD levels for typical degrees of damage, as adopted by the latest revision of the Greek Code of Structural Interventions (KAN.ΕΠΕ., 2022). Figure 64 presents such values for each damage state, as proposed by FEMA P-58-1 (ATC, 2019).

Several similar approaches and proposed drift values are available in the literature. Rossetto (2004) has made a comprehensive review in her PhD Thesis; some examples are presented in

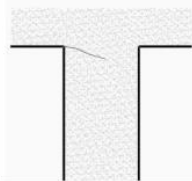
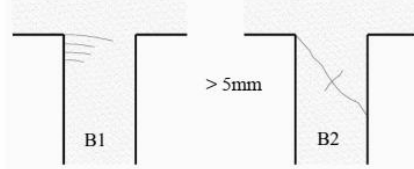
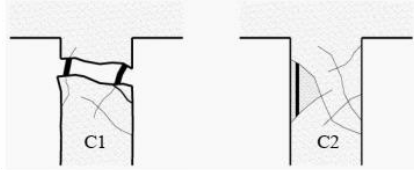
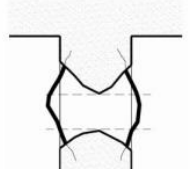
Limited importance	Light damage	A		$< 2\text{mm}$	$d=0$
		B		$> 5\text{mm}$	$d \ll$
Affecting the overall safety	Serious	C			$d < 1\%$
		D or D/E		Buckling or fracture of bars, opening or fracture of stirrups	$d > 2\%$

Figure 55. Typical degrees of damage of columns and beams (d: storey drift or drift of member ends, KAN.ΕΠΕ., 2022)

Damage State	Description	Residual Story Drift Ratio $\Delta / h^{(1)}$
DS1	No structural realignment is necessary for structural stability; however, the building may require adjustment and repairs to nonstructural and mechanical components that are sensitive to building alignment (e.g., elevator rails, curtain walls, and doors).	0.2% (equal to the maximum out-of-plumb tolerance typically permitted in new construction)
DS2	Realignment of structural frame and related structural repairs required to maintain permissible drift limits for nonstructural and mechanical components and to limit degradation in structural stability (i.e., collapse safety)	0.5%
DS3	Major structural realignment is required to restore margin of safety for lateral stability; however, the required realignment and repair of the structure may not be economically and practically feasible (i.e., the structure might be at total economic loss).	1%
DS4	Residual drift is sufficiently large that the structure is in danger of collapse from earthquake aftershocks (note: this performance point might be considered as equal to collapse, but with greater uncertainty).	High Ductility Systems $4\% < 0.5V_{design}/W$
		Moderate Ductility Systems $2\% < 0.5V_{design}/W$
		Limited Ductility Systems $1\% < 0.5V_{design}/W$

Figure 56. Damage States for Residual ISD Ratio (FEMA P-58-1, ATC, 2019)

**Earthquake Resilient Schools - EReS [BSB 966]**  
**Project Nr: 101101206 (UCPM-2022-PP)**  
**Deliverable D4.1: Investigation of seismic risk indicators based on instrumentation of school buildings in the selected pilot sites**

Source	Structure Type	Damage State	Parameter	Value	Comments
Duffey et al. (1994)	Low-rise shear walls	Serviceability (threshold) Life safety (threshold)	ISD <sub>max%</sub>	0.8% 1.8%	Experiment
Gulkan and Sozen (1974)	MRF	Non-structural damage Repairable damage Irreparable damage Collapse	ISD <sub>max%</sub>	0.0-1.0% 1.0-4.0% 4.0-6.0% >6.0%	Experiment
Bracci et al. (1995)	Non-ductile MRF	No damage Slight damage (threshold) Minor damage (threshold) Moderate damage (threshold)	ISD <sub>max%</sub>	0.28, 0.24, 0.24% 0.89, 1.07% 1.33% 2.24, 2.03%	Shake-table testing of three 1/3 scale models of MRF designed to gravity loads only.
Rzhevsky and Avanesov (1978)	MRF	Collapse (threshold)	ISD <sub>max%</sub>	7-8%	Dynamic tests on 3 scaled model frames
Wang and Shah (1987)	Infilled MRF	Non-structural damage (threshold) Non-structural damage Collapse of non-structural components	ISD <sub>max%</sub>	0.004% 0.004-0.02% >0.02%	Tests on models of infilled frames.
Kircher et al. (1997)	Low-rise shear-walls: High seismic code Moderate code Low seismic code Gravity designed	Slight/Moderate/Extensive/Collapse Slight/Moderate/Extensive/Collapse Slight/Moderate/Extensive/Collapse Slight/Moderate/Extensive/Collapse	Drift ratio	0.004/ 0.01/ 0.03/ 0.08 0.004/ 0.008/ 0.023/ 0.06 0.003/ 0.006/ 0.015/ 0.035 0.002/ 0.005/ 0.012/ 0.028	Assembled as the average of published experimental results by several different authors.
Ghoborah et al. (1999)	MRF	Non-structural damage Repairable damage Irreparable damage/partial collapse Collapse	ISD <sub>max%</sub>	<1.0% 1.0-4.0% 4.0-6.0% >6.0%	Based on experimental work of Roufaiei and Meyer (1981).

Source	Structure Type	Damage State	Parameter	Value	Comments
Mosalam et al. (1997)	Low-rise bare frames	No damage Insignificant damage Yielding/moderate damage General yielding/extensive damage	ISD <sub>max%</sub>	0.0-0.2% 0.2-0.5% 0.5-1.0% >1.0%	Judgement
	Low-rise infilled frames	No damage Insignificant damage Yielding/moderate damage General yielding/extensive damage	ISD <sub>max%</sub>	0.0-0.02% 0.02-0.05% 0.05-0.10% >0.10%	Judgement
HAZUS99 (FEMA 1999)	Low-rise, High seismic code level: Bare MRF Shear-wall	Slight/Moderate/Extensive/Collapse Slight/Moderate/Extensive/Collapse	Total drift ratio	0.005/ 0.01/ 0.03/ 0.08% 0.004/ 0.01/ 0.03/ 0.08%	Based on judgement but includes some experimental data.
	Low-rise, Moderate seismic code level: Bare MRF Shear-wall	Slight/Moderate/Extensive/Collapse Slight/Moderate/Extensive/Collapse	Total drift ratio	0.005/ 0.0087/ 0.0233/ 0.06% 0.004/ 0.0084/ 0.0232/ 0.06%	
FEMA273 (ATC 1997)	MRF	Immediate occupancy Life safety Collapse prevention	Transient/ Permanent Drift	0.0-1.0 / 0.0% 1.0- 2.0 / 0.0-1.0% 2.0- 4.0 / 1.0-4.0%	Judgement and some experimental data.
	Shear-walls	Immediate occupancy Life safety Collapse prevention	Transient/ Permanent Drift	0.0-0.5 / 0.0% 0.5- 1.0 / 0.0-0.5% 1.0- 2.0 / 0.5-2.0%	
FEMA273 (ATC 1997)	Masonry infill panel	Immediate occupancy Life safety Collapse prevention	Transient/ Permanent Drift	0.0-0.1 / 0.0% 0.1- 0.5 / 0.0-0.3% 0.5- 0.6 / 0.3-0.6%	Judgement, some experimental data.

**Figure 57.** Experimental values of maximum inter-storey drift ratio (or total drift ratios for low-rise buildings) characterising observed damage limit states in RC structures (top). Judgement/code values of maximum inter-storey drift ratio (or drift ratios for low-rise buildings) characterising damage limit states in RC structures (bottom) (Rossetto, 2003)

#### **4.1.2 Drift estimation based on measurements**

Having installed accelerometers on multiple storey levels of the school building, it is possible to measure the building's response at these specific locations during an earthquake. For the drift calculations, we double-integrate the recorded accelerations over time to obtain the displacement time histories at those locations. With the displacement responses  $u_n(t)$  and  $u_{n-1}(t)$  at two successive levels, we can calculate the interstorey drift as  $d_n(t)=(u_{n-1}(t)-u_n(t))/H_n$ ,  $H_n$  being the height difference  $H_n=h_n-h_{n-1}$  of these successive levels. Likewise, we can estimate the global drift of the structure if the installed accelerometers are at the roof and the ground level of the building.

The calculated drift ratios can be used as damage indicators based on values given in the literature as presented in Section 4.1.1. It should be noted that since the installed accelerometers were not always possible to be located at the same vertical place on each floor level, torsional effects should be considered into the drift calculations.

#### **4.1.3 Pilot studies in typical school buildings in the CBA**

We conducted testing on a representative building from the Greek school building stock, which is also one of the selected structures to be instrumented with accelerometers. This building was fully documented in Deliverable 3.2 of WP3.

In the absence of some actual strong motion recordings until the completion of the present WP4, we use, in order to present the general framework of the processes involved, synthetic data through numerical F.E.M. simulations. The input seismic motion was the accelerogram of the Samos 2020 earthquakes, as recorded in Izmir. This motion was assigned with various scaling factors to check the inelastic response of the school building. We considered non-linear inelastic dynamic analysis with concentrated plasticity at the potential plastic hinges. The double time differentiation of the response of the displacements acquired on specific nodal locations of the structure will later be used as the main signals simulating the actual accelerations that are to be measured on instrumented structures. It should be noted that in the case of inelastic non-linear analysis, accomplished utilizing the CSI's SAP2000 software, we do not directly use the accelerations response of the structure since it seems to correspond to some non-equilibrated intermediate step used to compute displacements up to convergence of the step. For that reason, we use the second derivative of the displacement time history in order to produce simulated accelerations on the instrumented structure.

For the inelastic non-linear response of structure under strong motion earthquake excitation, for which case damage is presented in the structure in the form of plastic hinges, the global (top to basement) drifts of the building for both directions are given in Table 4 at several locations of the floor's plan (Figure 58).

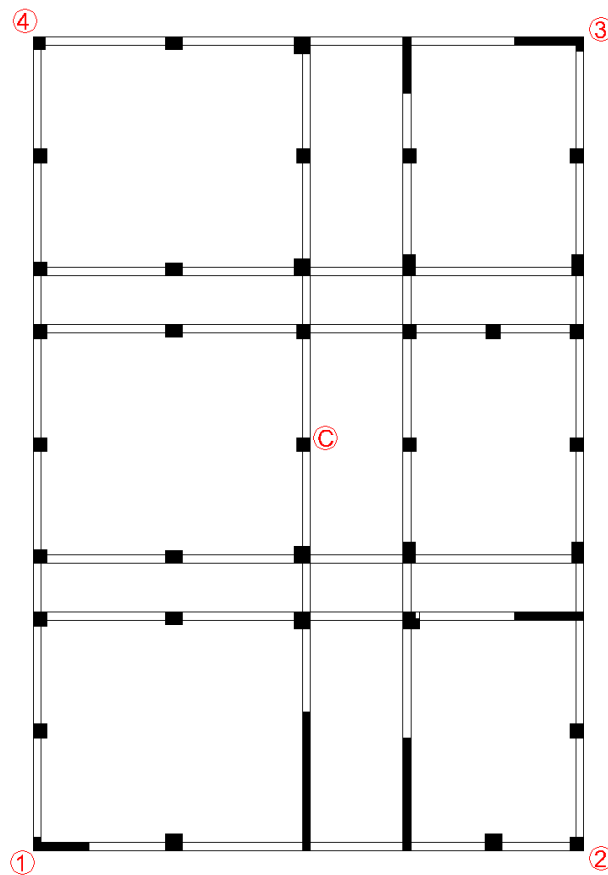


**Figure 58.** Nodes of finite element model of the typical school building where the drifts are calculated

**Table 4.** Global (top to basement) drift estimates at different nodes of the structure for the inelastic analysis

Location	Min <sub>x</sub> (%)	Max <sub>x</sub> (%)	Min <sub>y</sub> (%)	Max <sub>y</sub> (%)
1	-0.203	0.137	-0.106	0.090
2	-0.202	0.137	-0.076	0.098
3	-0.254	0.174	-0.074	0.092
4	-0.257	0.170	-0.110	0.093
C	-0.202	0.126	-0.066	0.057

The time history of global drifts as calculated from records at node C is depicted in Figure 59.

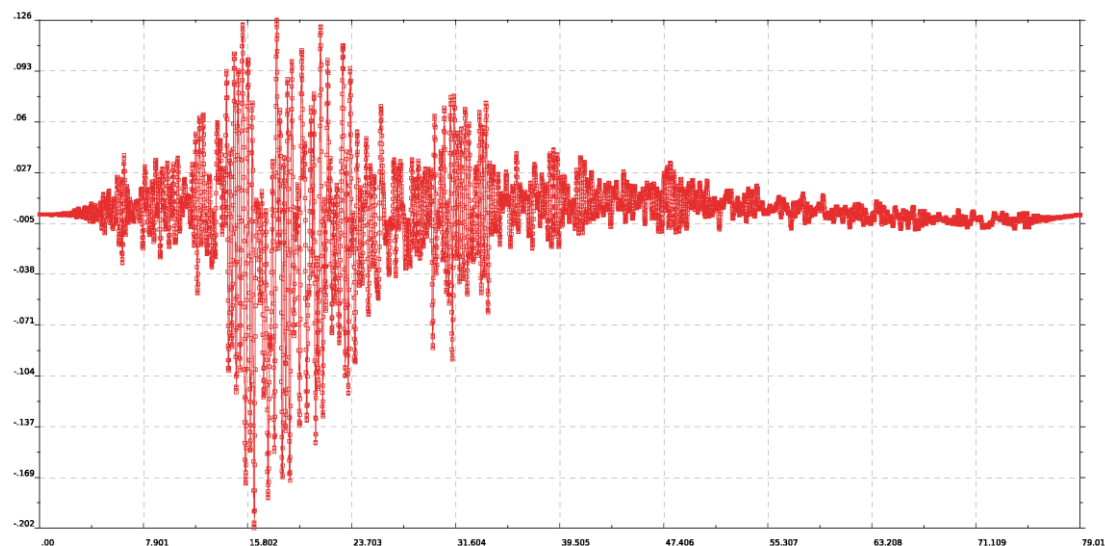


**Figure 59.** Global drift time-history, in x-direction, at node C of the structure for the inelastic response case

As it has been mentioned, interstorey drifts can be typically used as potential damage indicators. However, in our case, and due to the limited number of available recording instruments, two 3D accelerometers are installed at each instrumented building, one at the top slab, and one at the basement. For the cases where the building is not a single storey one, the global (building top to base) drift does not coincide with the specific interstorey drift of each storey. In the present, simulated investigation for the two storey building, additional data also for the first storey drifts can be calculated through the stimulated response data and are presented in Table 5.

**Table 5.** First storey drift estimates at different nodes of the structure for the inelastic analysis

Location	Min <sub>x</sub> (%)	Max <sub>x</sub> (%)	Min <sub>y</sub> (%)	Max <sub>y</sub> (%)
1	-0.206	0.136	-0.101	0.081
2	-0.206	0.135	-0.071	0.086
3	-0.234	0.150	-0.070	0.081
4	-0.234	0.150	-0.104	0.083
C	-0.192	0.114	-0.070	0.047

Comparing the results between Table 4 and Table 5, differences between the global (top to basement) and first storey drifts are observed. However, the order of magnitude is the same, and we can conclude that the actual recordings from the top and basement 3D accelerometers can be quite reliably used as a primary indicator of potential damage to the building. Another issue to point out is that the maximum drifts are expected to occur along the perimeter of the building (nodes 1-4), due to its rotational response during an earthquake excitation. Since this is not the case in the current instrumentation scheme, where an actual recording will be available only at one location of the top and basement of the building (where the two 3D accelerometers are installed), numerical simulations such as the one presented herein can be used in order to approximately estimate the maximum drifts at the perimeter of the building, based on the one recorded at the accelerometer locations. Of course, a full instrumentation of a building with an adequate number of sensors along its perimeter and at each building level would give an exact depiction of the actual response. However, this is usually not financially feasible, and complimentary estimations through the use of reliable F.E. models, such as the one shown above, will be typically needed.

#### **4.2 SEISMIC DAMAGE INDICATORS BASED ON THE DETERIORATION OF STRUCTURAL PROPERTIES IN THE INELASTIC RANGE**

The development of a significant level of damage in a building is associated with the entry of the building's response into the inelastic range through the formation of plastic hinges or other types of failure in structural members. When this occurs, the building's stiffness is clearly reduced compared to its initial, elastic state. It could therefore be investigated whether it is feasible to calculate the change in the structure's stiffness due to a strong earthquake, reflected in a corresponding shift of the fundamental period of the structure to larger values, which would indicate inelastic behavior and a significant likelihood of damage development.

The above approach is linked herein to the processing of earthquake recordings at the top and base of structures, deriving from the next generation (Low-Cost) accelerometers used for their instrumentation. Consequently, we are referring to an effort to determine the basic stiffness characteristics of the building using acceleration time-histories recorded at the top and base. Moreover, as the structure initially exhibits elastic response, and may gradually transition to inelastic behavior as the earthquake

progresses, it is required to identify the modification in stiffness over time during the strong seismic motion.

Due to lack of actual earthquake recordings from the instrumented school networks until now, such an approach is herein investigated on an analytical level only, providing a brief outline of the calculation framework and highlighting the several shortcomings and limitations of the procedure in the following sections.

#### **4.2.1 Estimation of dynamic response properties based on measurements at the top and the bottom of the buildings**

The basic dynamic characteristics of a structure are commonly identified by employing numerical simulation and eigenvalue analysis, where mode shapes and eigen periods of vibration can be calculated. However, when the structure undergoes inelastic deformations, calculation of mode shapes is not feasible since there is a constant shift of its stiffness throughout the response.

A common method for evaluating the dynamic properties of the structure in such cases involves post-processing of the response time-histories in the frequency domain. As a first step, the Fourier spectra of the acceleration time-histories at the top of the building can provide insights into the predominant frequencies of the structural response. However, these spectra also include components related to the characteristics of the specific earthquake motion and of the soil deposit response. To address this, ratios of the Fourier spectra between the top and the base of the structure can be used, to effectively isolate the frequencies where motion is amplified due to the structural response itself, partially filtering out the effects of the input motion and the soil response. This concept has been initially introduced to identify strong motion amplification due to local site effects in soil deposits. Later, it was successfully employed to facilitate the investigation of soil-structure interaction phenomena. Indicatively, Stewert et al. (1998) utilized the roof/free-field, roof/foundation, and foundation/free-field Fourier ratios of the respective response acceleration time-histories, commonly addressed as transfer functions or transmissibility functions depending on the examined points of the system, which were properly smoothed to provide rough estimates of modal frequencies of the soil-structure system.

The approach of using Fourier ratios to identify the structural system's dynamic properties presents several challenges. Apart from the issues related to the shape of the resulting Fourier ratio, which is often characterized by extreme peaks at specific frequencies potentially due to numerical issues rather than reflecting the actual response of the structure, there is also the

problem of the influence of soil response. Indeed, due to the non-linear soil behavior even in low levels of seismic excitation, a shift of the Fourier ratio to higher period values (lower frequencies) can be also attributed to the modification of the soil properties with increasing soil shear strain, Related findings are presented in Kirtas et al. 2007, regarding various soil types of decreasing stiffness, which bears similarities with the case of deteriorating soil properties addressed herein. Consequently, the correlation between observed changes in the Fourier ratio and the level of damage on structures should be made with due caution, considering all involved parameters.

#### **4.2.2 Damage indicators based on stiffness degradation**

The concept of associating the shift of the building's eigen period with a damage level has received some attention during the last years (e.g. Eleftheriadou and Karabinis 2013, Ditommaso et al. 2013, Gallipoli et al. 2016, Diaz et al. 2023). Yet, research in this direction is still under way, and proper attention is required when trying to associate the elongation of the fundamental period of the structure with a specific damage level in structures of different configuration and dynamic properties.

Although the next generation accelerometers were successfully installed in several school buildings, as described in sections 2 and 3 of the present deliverable, they have not provided any earthquake recordings until the completion of WP4. Therefore, in order to investigate the feasibility of identifying structural dynamic features based on acceleration time-history recording at the top and the base of the structure, two numerical (Finite Element - F.E.) models have been examined.

- a) A typical reinforced concrete school building in Alexandroupolis.
- b) A simplified 3 storey, 2-dimensional reinforced concrete frame.

##### **4.2.2.1 Numerical analysis of a typical school in the CBA**

The F.E. model of a typical reinforced concrete school building in Alexandroupolis is depicted in Figure 60. This model was presented in detail in Deliverable 3.2 of WP3, since it was used for inelastic static analyses to check the applicability of the selected fragility curves.

In the present WP4, dynamic linear elastic and inelastic time-history analyses of the building were conducted, considering the accelerogram recordings of the Samos-Izmir earthquake in 2020, increasingly scaled so as to induce inelastic structural behavior. The resulting Fourier ratio between the top and

the base of the structure was then compared with the respective results from the linear elastic analysis.

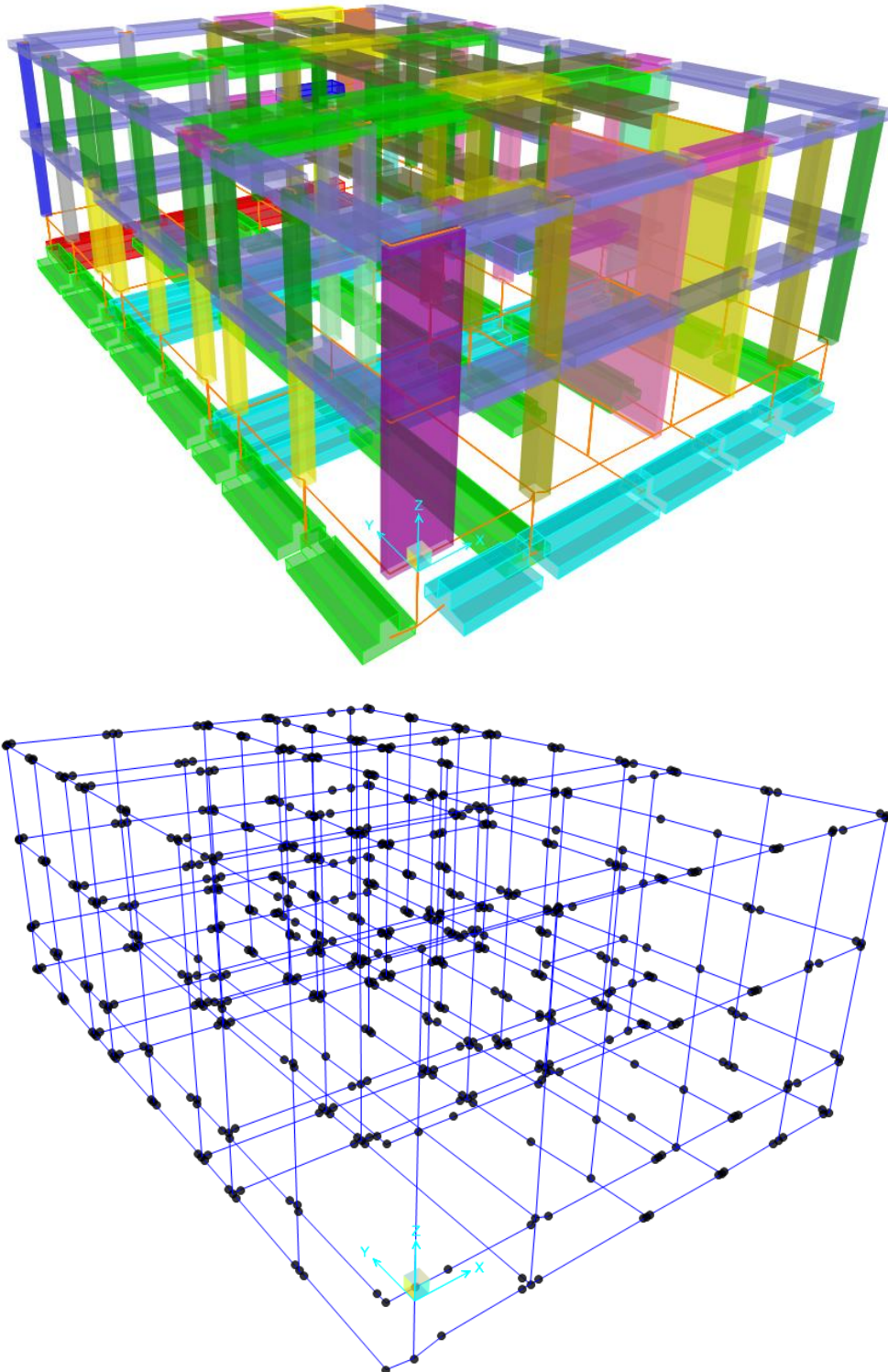


**Figure 60.** F.E. model of the examined school building (details provided in Deliverable 3.2)

Top-to-base Fourier ratio in the linear elastic response is indicatively presented for direction X in Figure 61. It is quite clear that two resonance frequencies can be identified. The first is identified at approximately 4Hz ( $T=0.25s$ ) corresponding to the 1<sup>st</sup> (fundamental) period of the structure, which was calculated at 0.254s using modal analysis. The second frequency observed in the Fourier ratio at 12.5Hz (0.08s) corresponds to the 4<sup>th</sup> period of the structure, which is the second one involving a significant modal participating mass ratio in the examined X direction (the modal analysis calculation yielded a respective eigenperiod of 0.078s). So, in principle, Fourier ratios seem to provide a comprehensive depiction of the dynamic properties of the building per examined direction. It is worth mentioning though, that in structures with significant influence of torsional modes, some components of the response will be harder to detect using the presented approach, especially if the installed accelerometers do not lie near the center of rotation of the building.

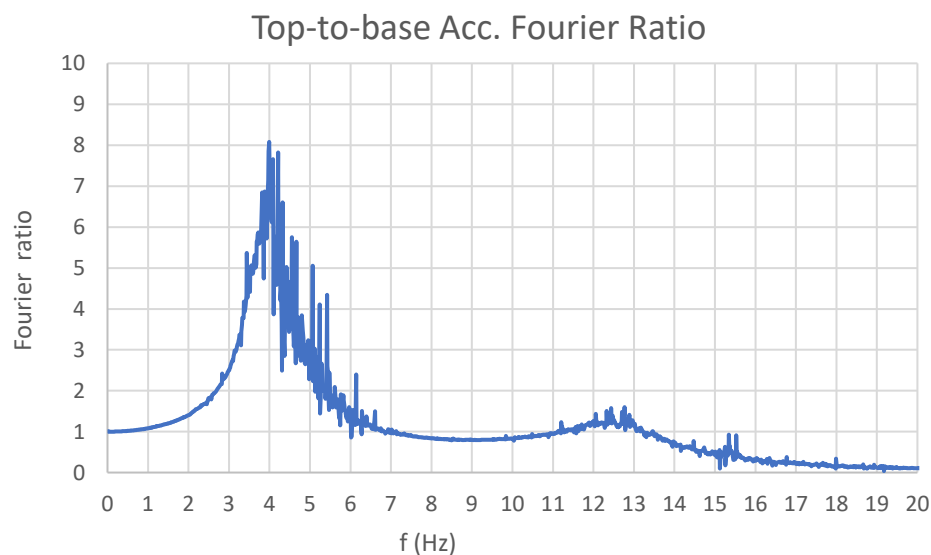


**Figure 61.** Fourier ratio of acceleration time-histories between the top and the base of the modeled structure (linear elastic response)

The inelastic dynamic analysis that was considered for the comparison resulted in the formation of multiple plastic hinges in the beam elements of the structure, as well as few hinges in columns, as depicted in Figure 62. It should be mentioned that this behavior resulted through scaling of the amplitude of the accelerogram of the Samos-Izmir earthquake in order to achieve inelastic behavior.

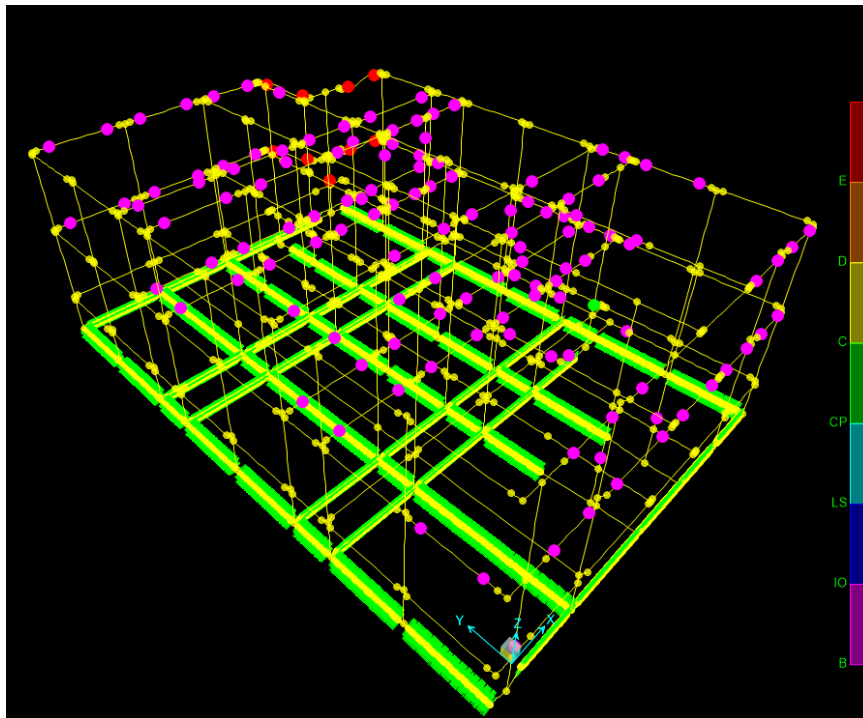


**Figure 62.** Plastic hinges developed during nonlinear dynamic analysis

Top-to-base Fourier ratio when the structure exhibits nonlinear (inelastic) behavior is indicatively presented for direction X in Figure 63. In this case, the diagram is not so clear, and a smoothing technique could be introduced to facilitate a better depiction. Yet, resonance frequencies are again visible at approximately 3.9Hz (0.256s) and in the range of 11-12Hz, although in the latter case it is difficult to discriminate the exact frequency value.

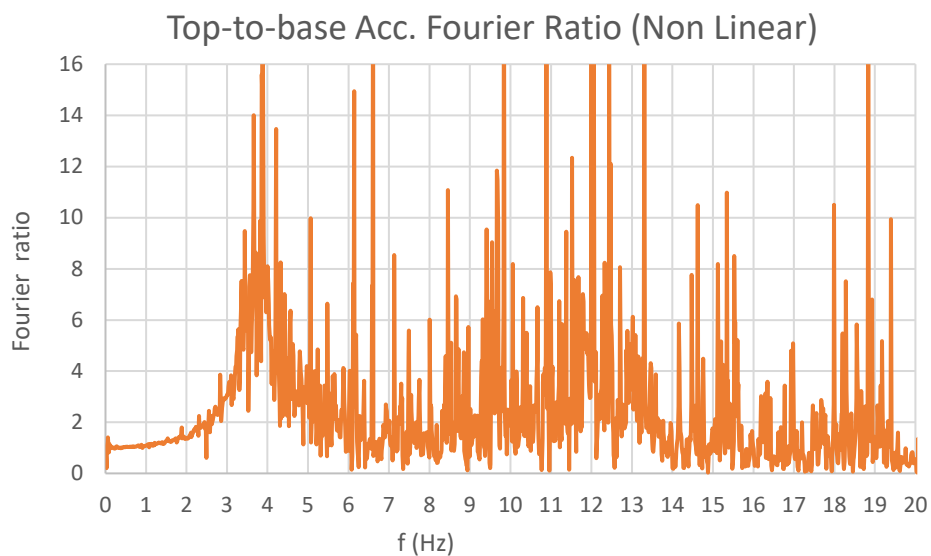


**Figure 63.** Fourier ratio of acceleration time-histories between the top and the base of the modeled structure (nonlinear response)

The results can be plotted on the same diagram to facilitate the comparison, as shown in Figure 64, where a closer look at the frequency range between 0-10Hz has been chosen. It is evident that the difference of the fundamental frequencies between the linear elastic (4Hz, 0.25s) and the nonlinear (3.9Hz, 0.256s) depicted in the diagram is not sufficient to provide a clear indication of inelastic behavior.

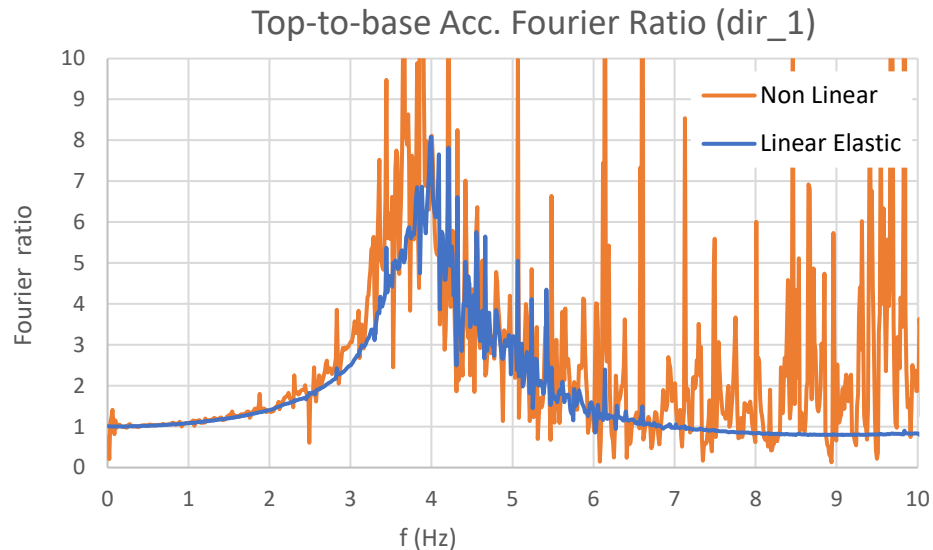


**Figure 64.** Fourier ratio of acceleration time-histories between the top and the base of the modeled structure (comparison between linear and nonlinear response)

A more elaborate step in this direction would involve calculating the ratio of the spectrograms at the top and base of the building for both the linear elastic and the inelastic response cases, capturing the variation of these values over time, using a sliding time window throughout the duration of the response. In this way, one would expect at the first seconds of the spectrogram to identify the fundamental frequency of the linear elastic structure, whereas, when reaching the part that several plastic hinges may have developed, a shift to lower frequency values indicative of inelastic response. Such an effort is presented in Figure 65.

The spectrogram for the elastic response case (Fig. 65, top) seems to identify the fundamental frequency of the structure from the first seconds of the excitation. The inelastic response of the structure (Fig. 65, bottom) activates more complex phenomena and frequency identification is less obvious. Although a small shift to lower frequencies (i.e. higher periods) could slightly be recognized in the time range between 25-35sec, this behavior is not very clear and higher values of the top-to-base ratio are also presented in several

frequencies, away from the range of the fundamental period of the structure. Note that in Figure 65, the results are given in dB, hence the existence of also negative values of the spectral ratios.

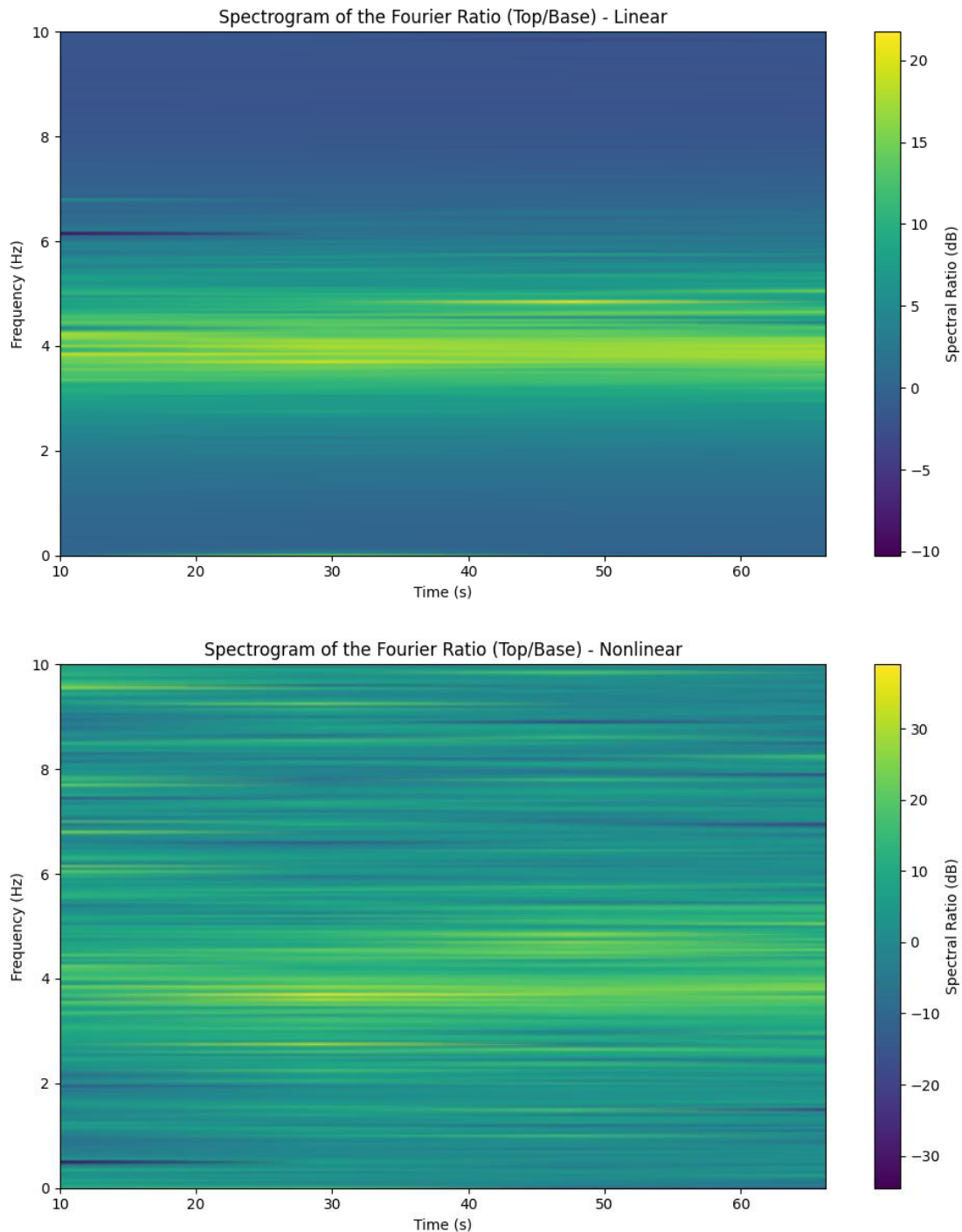


**Figure 65.** Ratios of spectrograms of acceleration time-histories between the top and the base of the modeled structure for linear elastic response (top) and nonlinear response case (bottom)

#### 4.2.2.2 Numerical analysis of a simplified 3-storey, 2D frame

Considering that inelastic dynamic time-history analyses of realistic 3D buildings are highly time-consuming, it was decided to test this approach on a simpler, two-dimensional reinforced concrete frame. This approach could allow to better identify the dynamic characteristics of the building in the elastic linear response, as well as the modifications that occur in the inelastic range. The geometry of this structure is presented in Figure 66 and its reinforcement in Table 1.



Figure 66. Geometry of a simplified concrete frame

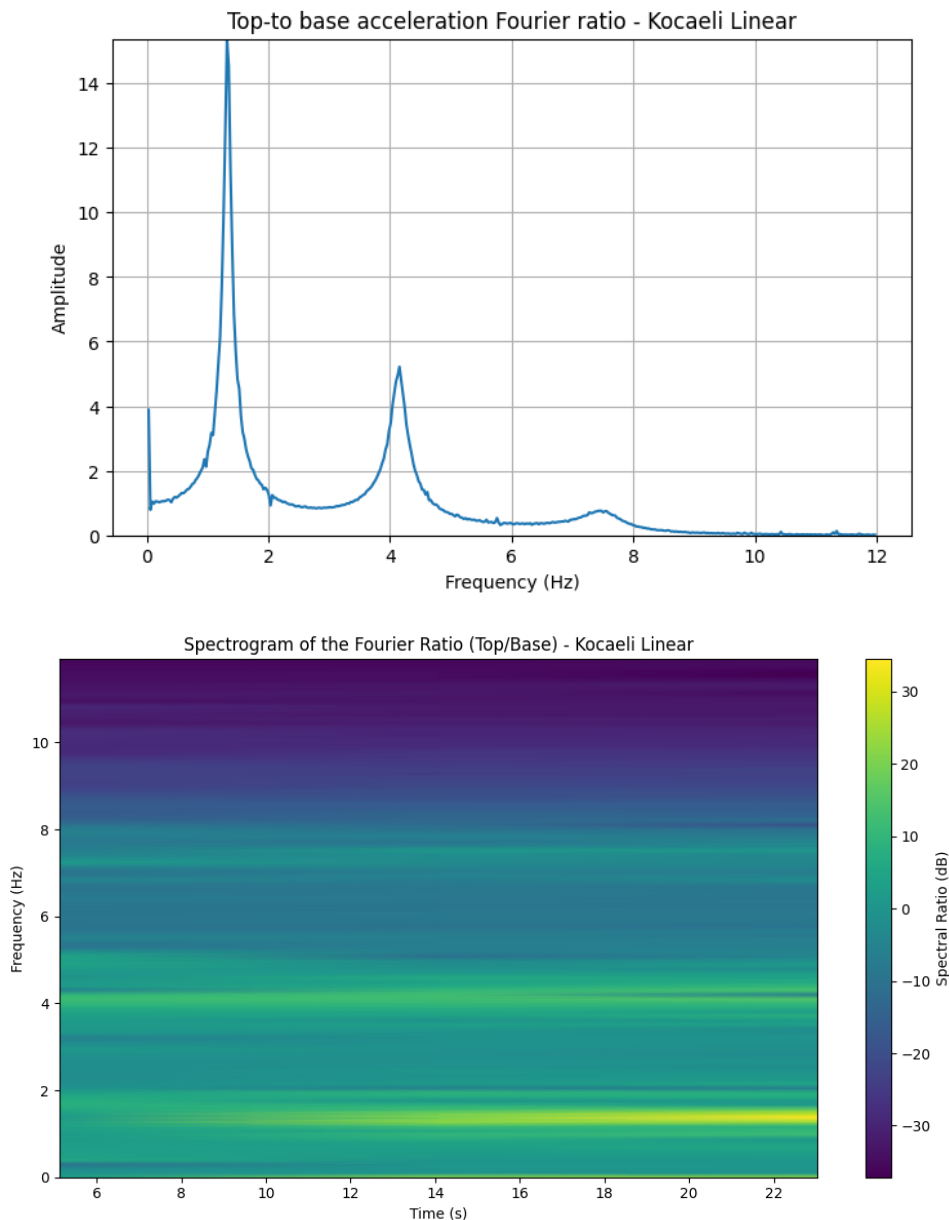
Table 6. Simplified concrete frame reinforcement.

Structural element		Longitudinal	Transverse
Ground storey columns		8Ø18	Ø8/120mm
Higher storeys columns		8Ø16	Ø8/150mm
Ground storey beams	External supports	3Ø18(t) - 2Ø18 (b)	Ø8/150mm
	Internal supports	5Ø18(t) - 3Ø18 (b)	Ø8/150mm
Higher storeys columns	External supports	3Ø16(t) - 2Ø16 (b)	Ø8/150mm
	Internal supports	5Ø16(t) - 3Ø16 (b)	Ø8/150mm

The modal analysis of this structure has yielded eigenperiods of  $T_1=0.753\text{sec}$  ( $f_1=1.33\text{Hz}$ ),  $T_2=0.240\text{sec}$  ( $f_2=4.17\text{Hz}$ ) and  $T_3=0.130\text{sec}$  ( $f_3=7.66\text{Hz}$ ). Then,

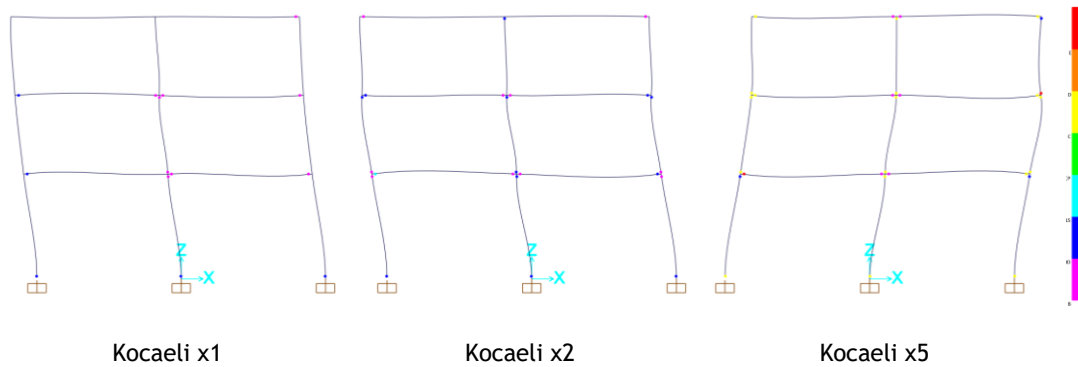
using the seismic motion of the Kocaeli (Türkiye) earthquake of August 17, 1999 we performed some time-history analyses, first a linear elastic one, and then several non-linear, scaling the acceleration values x1, x2 and x5.

Figure 67 presents the top-to-base acceleration Fourier ratio for the elastic analysis, as well as the corresponding spectrogram ratio, and it perfectly identifies the frequencies of the structure, as calculated through the modal analysis.



**Figure 67.** Fourier ratio of acceleration time-histories between the top and the base of the simplified 2D frame (top) and the corresponding spectrogram ratio (bottom) for the linear elastic response

Figure 68 shows the formation of plastic hinges for all inelastic analyses of the structure, revealing significant damage in several beams and columns.



**Figure 68.** Plastic hinges for the nonlinear dynamic analyses

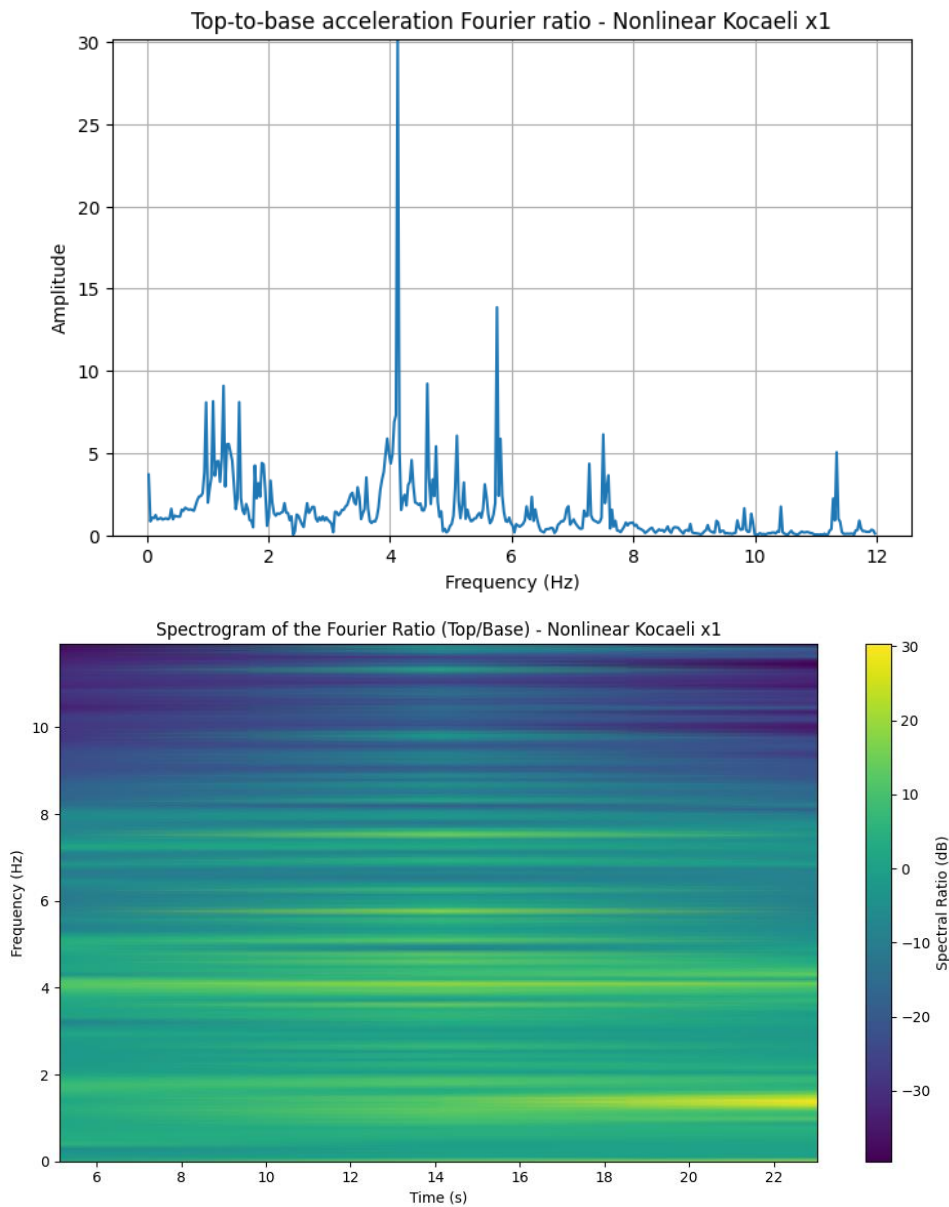


**Figure 69.** Fourier ratio of acceleration time-histories between the top and the base of the simplified 2D frame (top) and the corresponding spectrogram ratio (bottom) for the nonlinear inelastic response using the Kocaeli motion without scaling

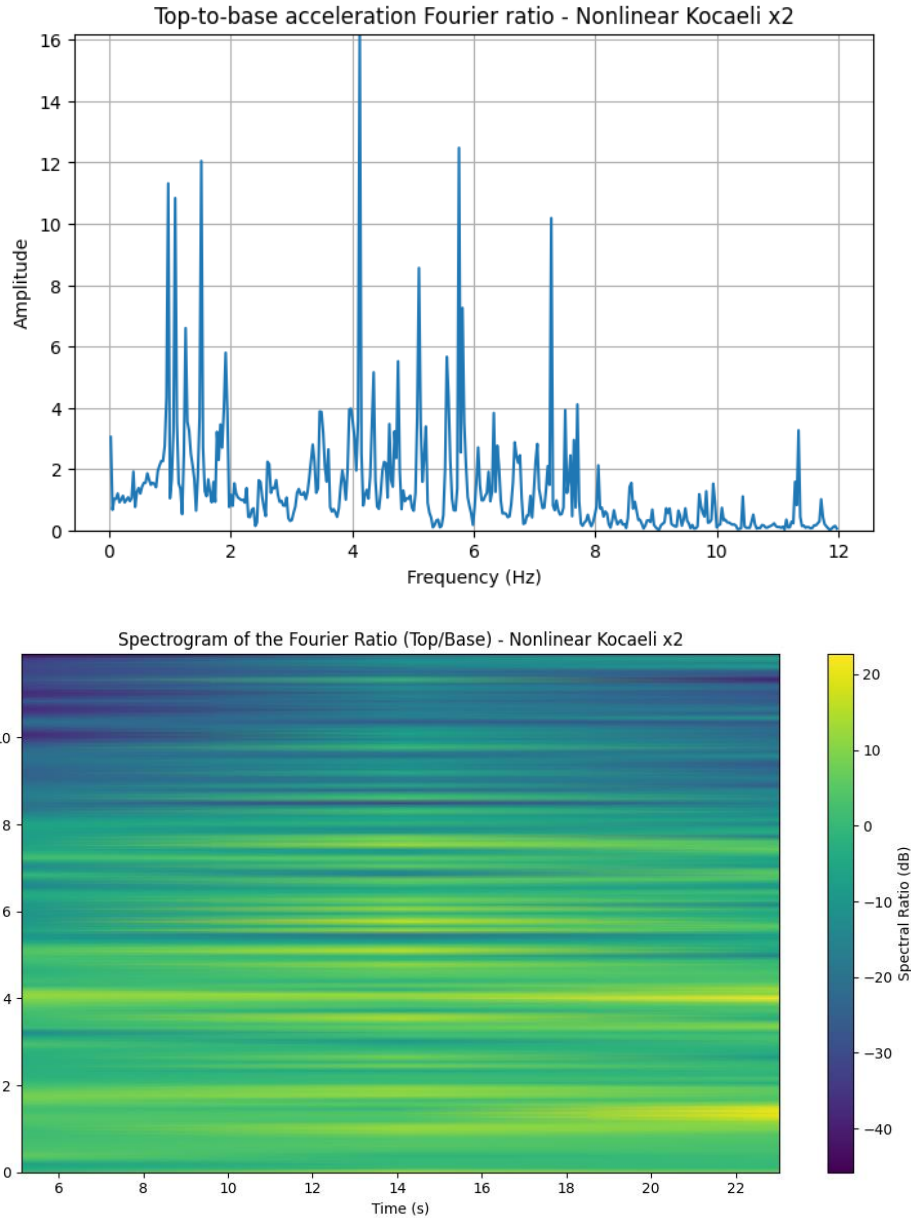


**Figure 70.** Fourier ratio of acceleration time-histories between the top and the base of the simplified 2D frame (top) and the corresponding spectrogram ratio (bottom) for the nonlinear inelastic response using the Kocaeli motion scaled x2

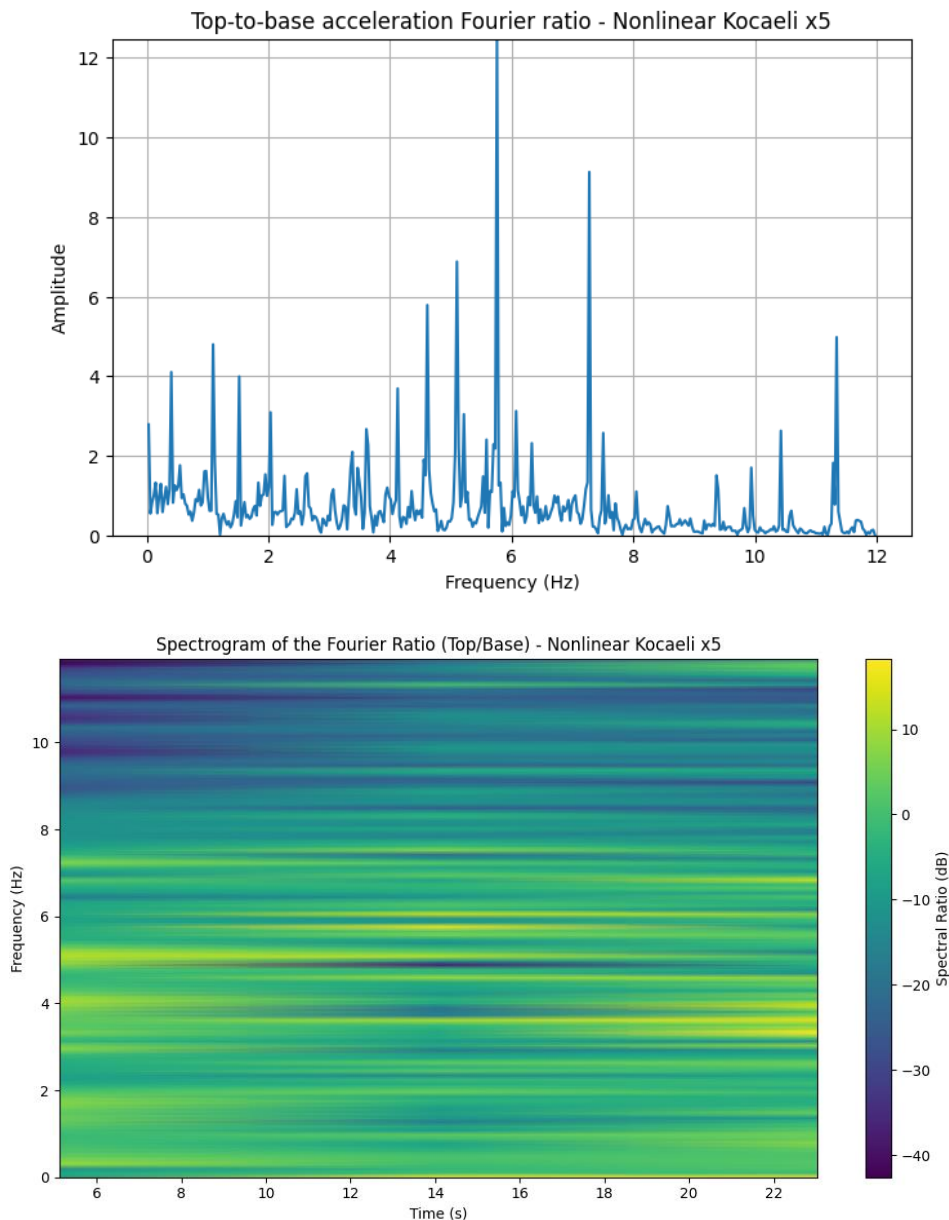


**Figure 71.** Fourier ratio of acceleration time-histories between the top and the base of the simplified 2D frame (top) and the corresponding spectrogram ratio (bottom) for the nonlinear inelastic response using the Kocaeli motion scaled x5

Figures 69-71 present the top-to-base ratios of the acceleration Fourier spectra for all inelastic analyses. A slight shift towards lower frequency values (i.e., higher periods) is observed in Figure 69 at the beginning of the inelastic response. However, under stronger input motions (Figures 70-71), the behaviour becomes somehow chaotic and it is not possible to identify the dynamic characteristics.

#### **4.2.2.3 Discussion on the stiffness degradation indicators**

Having installed accelerometers at the top and the bottom of the school buildings, it is possible to identify the dynamic characteristics of the structures in the elastic range, using the top-to-base Fourier ratios.

Within the lifetime of the school buildings, it is expected that the installed accelerometers will record several low to moderate earthquakes, with the buildings performing in the elastic range. Having these values as a reference, when a stronger earthquake occurs, the frequency shift to lower values in the beginning of the inelastic response, or even the more chaotic response in the results of a very severe earthquake could produce some clear indicators that the school buildings have entered the inelastic range, and their structural elements have been damaged.

However, the aforementioned procedure was unable to quantify this damage, indicating the need for further investigation to achieve this goal.

### **4.3 SEISMIC DAMAGE INDICATORS BASED ON FRAGILITY FUNCTIONS**

Seismic vulnerability and risk assessment studies are important for minimizing the damage caused by earthquakes and post-earthquake preparation. These studies are one of the most important tools in reducing human and economic losses.

In addition, seismic risk and loss estimation studies enable public education and awareness raising, estimation of manpower requirements for disaster management, and budget planning. Another objective of seismic risk studies is to ensure that post-earthquake disasters remain at a manageable level. The aim is to identify the elements at risk and the critical areas and then to gain foresight into the potential losses.

The first actions taken immediately after the earthquake are crucial to managing the crisis. Therefore, post-earthquake decision-making mechanisms based on scenario-based seismic hazard analyses are of utmost importance. Measuring structural damage or loss immediately after the earthquake and planning initial actions concerning the results obtained is one of the objectives of near real-time seismic risk assessment studies.

Fragility curves are widely used tools for the probabilistic prediction of structural damage to a particular structure or group of structures. The fragility curve expresses the conditional probability of reaching or exceeding a predefined damage state ( $DS_i$ ) for computed damage( $d$ ) under a certain ground motion intensity measure ( $IM$ ). The mathematical expression of the curves is given in Equation 1.

$$P(d \geq DS_i | IM) = \Phi \left[ \frac{1}{\beta_{DS_i}} \left( \ln \frac{IM}{\overline{IM}_{DS_i}} \right) \right] \quad (1)$$

Where,  $\beta_{DS_i}$  is the logarithmic standard deviation of the “d” conditioned on the  $IM$ ,  $\overline{IM}_{DS_i}$  symbolizes the median value of “d” under a certain  $IM$  value, and  $\Phi(\bullet)$  represents the standard cumulative distribution function.

In general, fragility curves obtained by considering analytical, empirical, hybrid, and expert judgment methods are mostly developed using log-normal distribution functions. These curves are defined using two statistical parameters, the median and the standard deviation [Baker,2015].

The primary objective of this chapter is to develop a near real-time seismic risk assessment methodology for the target school building. Subsequently, this methodology will be tested offline and decision-making mechanisms will be established regarding this methodology.

In the context of the Earthquake Resilient Schools - EReS [BSB 966] project, the flowchart of the near real-time seismic risk assessment study to be carried out using fragility curves is shown in Figure 72.

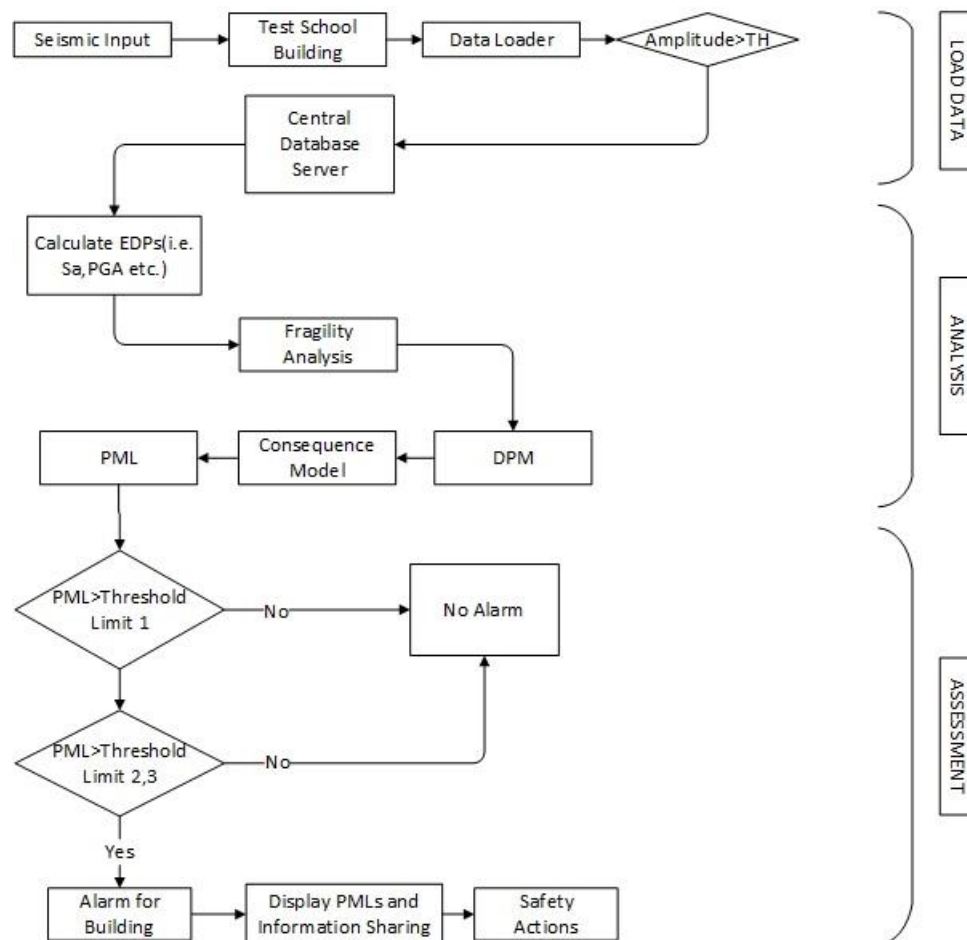


**Figure 72.** Basic steps of near real-time seismic risk assessment methodology

Figure 72 shows the basic steps of the near real-time seismic risk assessment for probable maximum loss (PML) values calculated using the fragility curves. The methodology consists of 3 main stages: Load data, Analysis, and Assessment.

Firstly, accelerometers placed at different locations of the target structure continuously monitor the instantaneous ground motion vibrations. Then, during the instantaneous measurement phase, if the acceleration-time record exceeds the threshold level (TH) of 0.005 g amplitude, the system identifies a possible earthquake. Following this identification, the 10 seconds before the first exceedance of the threshold level are taken into account and

transferred to the central database server, where the vibrations are permanently recorded for further processing.

The next stage is the analysis phase, where the intensity parameter considered in the fragility curve is calculated for the recorded acceleration-time record. Assuming that the fragility curves have been developed for  $S_a(g)$  and PGA, the values of these parameters are calculated first. The damage probability matrix (DPM) is calculated for the point of intersection of the calculated  $S_a(g)$  or PGA value on the fragility curves.

The direct use of DPM may not give a precise idea of how to establish instant decision mechanisms. Therefore, PML calculations are proposed to establish a relationship between structural damage and economic loss in the presented methodology. In simple terms, the PML refers to the ratio of repairing damage cost to the structure after the earthquake to the reconstruction cost of the structure. In the final assessment phase, the PML value computed is evaluated according to the predefined threshold limits, and then the warning system and information actions are performed.

The offline implementation of the presented methodology is accomplished for an existing school building located in Izmir, Türkiye. The 3-D finite element model of the considered structure is shown in Figure 73.

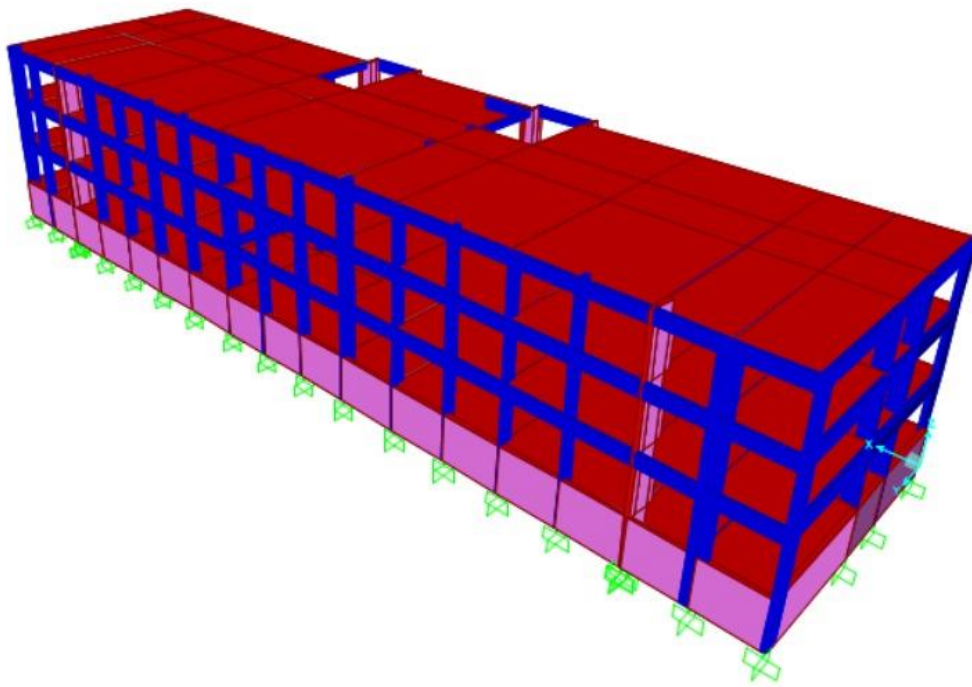


**Figure 73.** 3D numerical model of the existing school building

The considered building has recently been instrumented with accelerometers and has not been exposed to a destructive earthquake. For this reason, the seismicity of the location was determined using the target spectra computed by considering the DD-1 and DD2 seismic hazard levels expressed in TBSDC-2018.

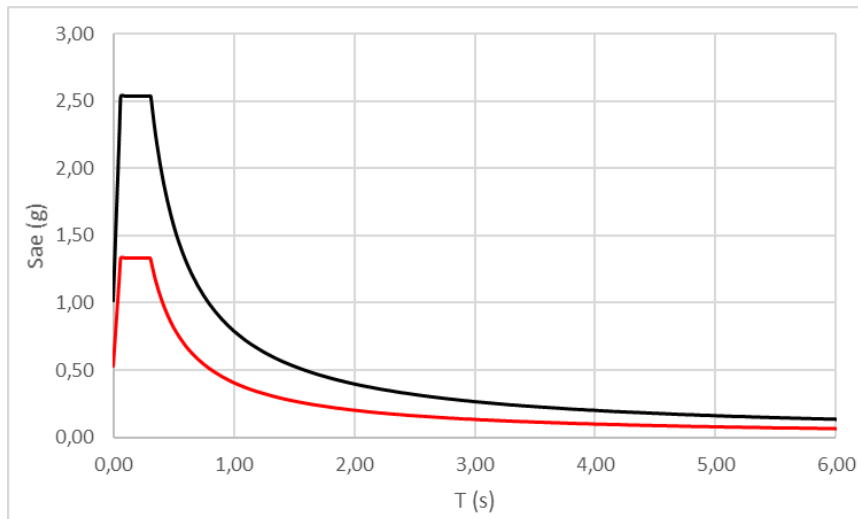


Figure 74. Target spectra for different seismic hazard levels

Considering the cracked section stiffness of the structure,  $S_a(T_1, g)$  values were calculated as 0.93 g and 0.48 g for DD-1 and DD-2 seismic hazard levels, respectively.

The vulnerability of the school building was evaluated using the appropriate fragility curves presented by Martin and Silva 2021 and given in Figure 4.4.

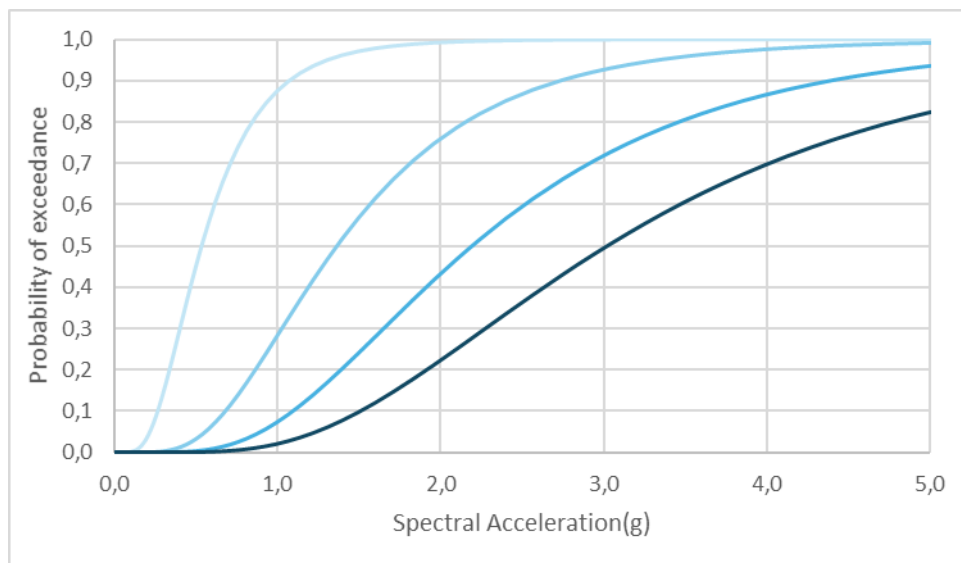


Figure 75. Fragility curves presented by Martin Silva 2009 for mid-rise school buildings

The DPM distribution obtained for DD-1 and DD2 hazard levels is given in Figure 76.

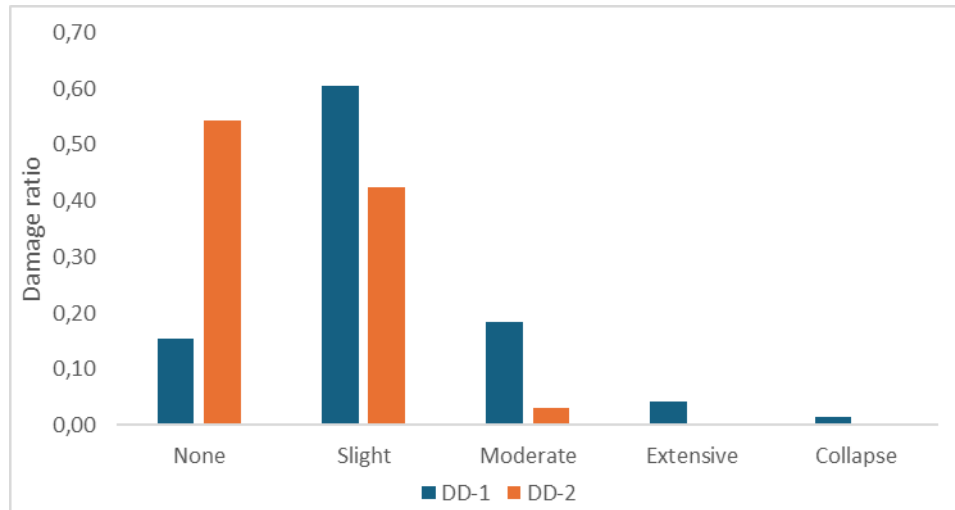


Figure 76. DPM values calculated for different seismic hazard levels

The consequence model [Martins and Silva, 2021] taken into account in relating the structural damage distribution to the economic loss are shown in Table 7.

Table 7. Consequence model utilized to derive vulnerability functions.

Damage State	CDR	Coefficient of variation
Slight	0.05	0.30
Moderate	0.20	0.20
Extensive	0.60	0.10
Collapse	1.00	0.00

The following is an example of the PML value that has been calculated for the DD-1 seismic hazard level using the CDR values given in Table 7.

$$PML: 0,15 * (0) + 0,61 * (5) + 0,18 * (20) + 0,04 * (60) + 0,02 * (100) = 11,05\%$$

Considering the calculations for the DD-1 seismic hazard level, the PML value was calculated as 11.05% using the consequence model proposed by Martins and Silva, 2021. The alarm threshold levels of PML values for four different ranges are defined below to assess the calculated PML value.

- Threshold Level 1 (PML (%) = 0-10): This refers to the level at which educational activities can continue safely and uninterrupted within the building.

- Threshold Level 2 (PML (%) = 10-20): This level indicates the plastic/permanent deformations in the structural elements; therefore, uses such as gas and electricity should be stopped.
- Threshold Level 3 (PML (%) = 20-40): This level means that educational activities in the building should stop, and the building needs to be assessed by seismic/structural experts. This is the level at which retrofiting is likely to be required, after which education can be resumed.
- Threshold Level 4 (PML (%) = 40-100): This is the level that indicates the necessity of rapid evacuation of the building without further evaluation. It usually refers to the level where the structure is likely to have partially collapsed.

The critical PML value calculated for the seismic hazard level DD-1 is 11.05%. The system presented is expected to alarm at level 2.

As a result of the step-by-step application of the presented methodology, it has been shown in a case study that instantaneous earthquake records obtained from instrumented target structures can predict the current damage state of the structure immediately after the earthquake. Another method proposed independently of fragility curves is the creation of decision-making mechanisms for the maximum drift ratio (MDR) damage parameter. To this end, the capacity curves of the target structure and the defined threshold levels are shown in Figure 77.

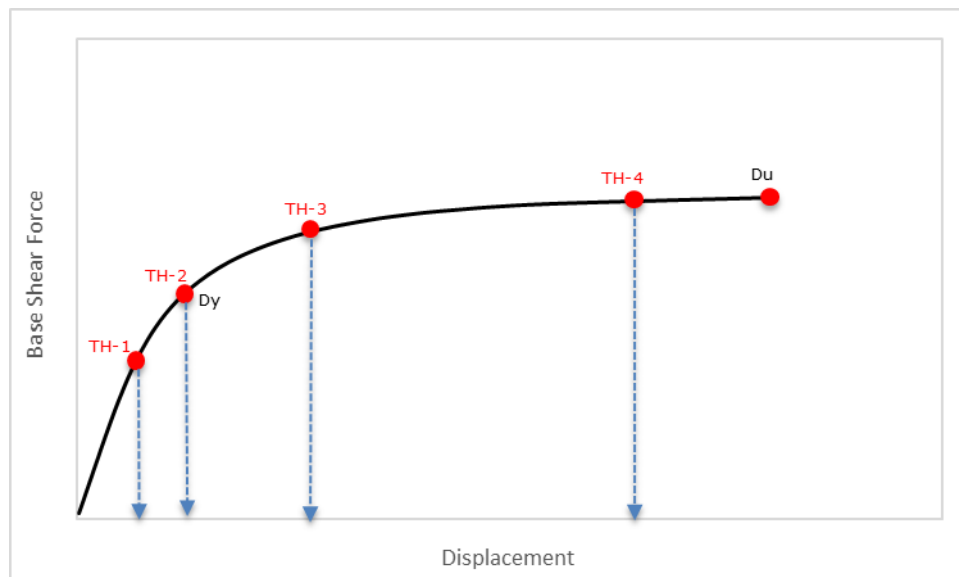
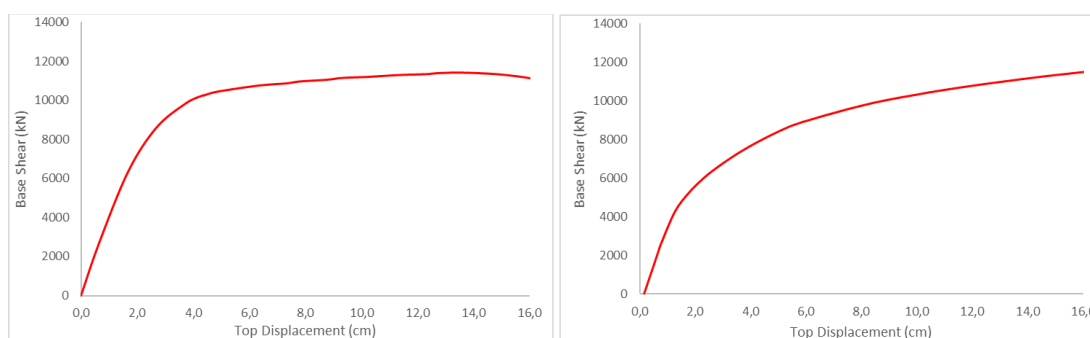


Figure 77. Identification of damage thresholds in capacity curves

Using the critical points shown in Figure 77 as a reference, they are associated with the four threshold levels mentioned above. In this study, Threshold Level

1, Threshold Level 2, Threshold Level 3 and Threshold Level 4 values were determined as  $0.7 \cdot D_y$ ,  $D_y$ ,  $0.25 \cdot D_u$ , and  $0.75 \cdot D_u$ , respectively. Therefore, in the evaluation to be carried out using the second method, the MDR is first calculated for both directions of the building, through equipment located in different locations. The alarm level is then determined for the critical MDR value. It would be safer to consider both methods together and making decision based on the critical method. The capacity curves obtained for both directions of the selected building are given in Figure 78.



**Figure 78.** Capacity curves in both directions; X direction (left), Y direction (right)

The MDR limits vary depending on the structural and geometrical characteristics of the structure under consideration. The four limit values have been calculated for both directions of the target structure and are given in Table 8.

**Table 8.** Recommended MDR(%) limits for both directions of the structure.

	TH-1	TH-2	TH-3	TH-4
X-Direction	0,179	0,255	0,595	1,786
Y-Direction	0,117	0,168	0,393	1,179

The considered structure has not yet been subjected to an earthquake. Therefore, it is not possible to calculate MDR through accelerometers/displacement meters. However, the action to be taken in case the structure is exposed to an earthquake has been explained.

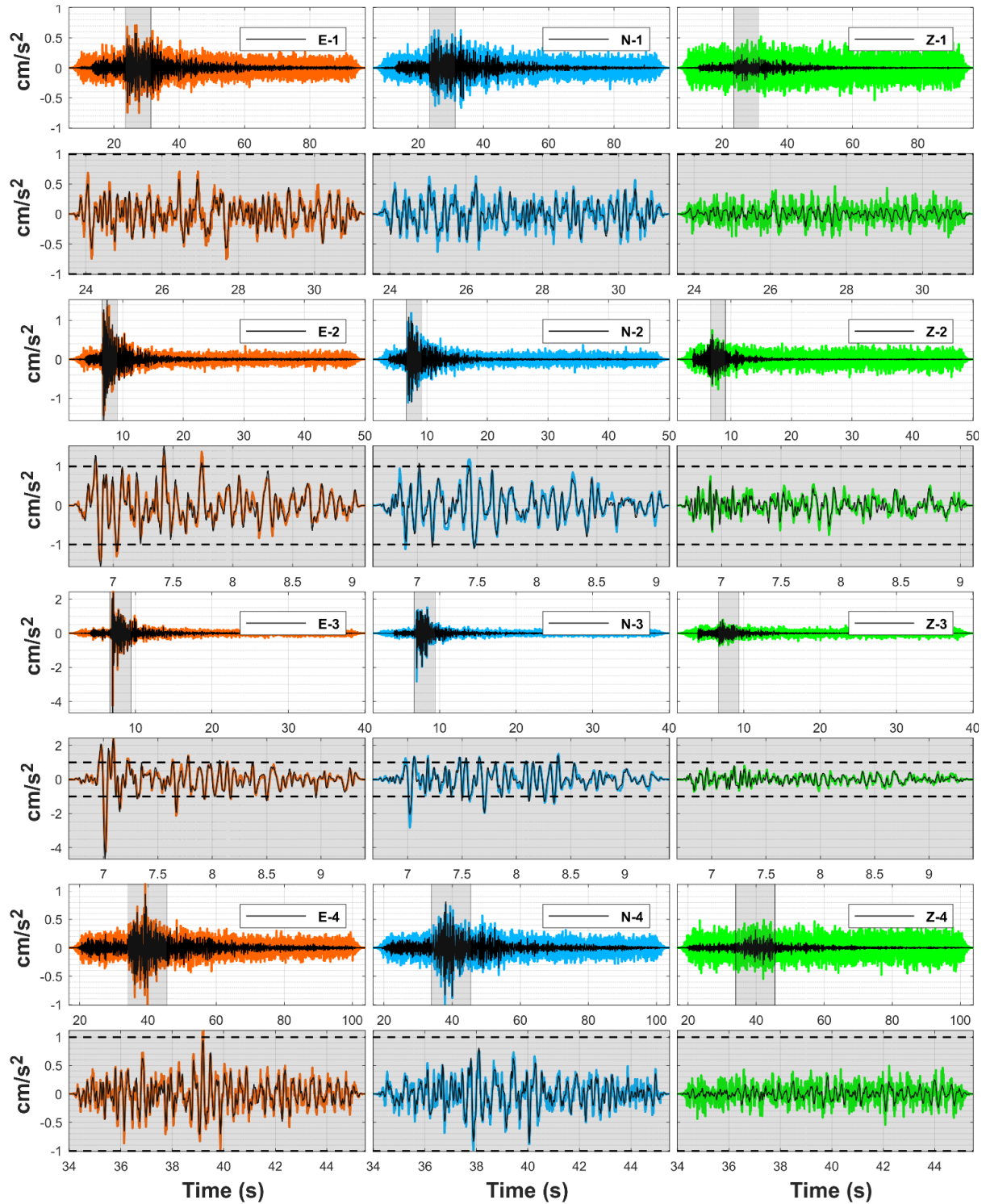
First, the MDR value can be calculated using the acceleration-time records obtained for both directions of the structure from the accelerometer located at different points of the target structure, or it is also possible to calculate the MDR directly from displacement measurements. Then, taking into account the limits given in Table 2, it is possible to predict the current damage state of the structure immediately after the earthquake.

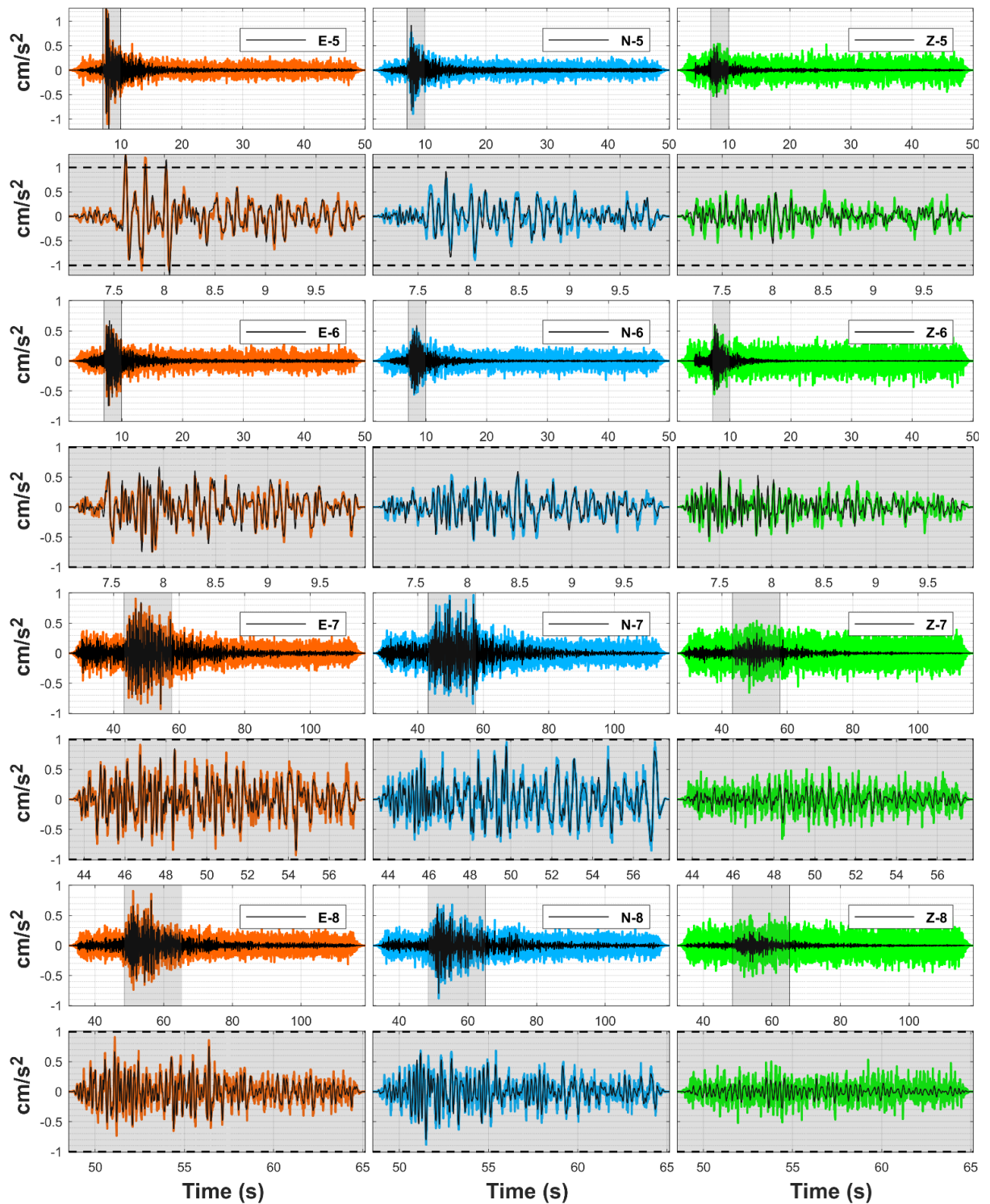
## 5 REFERENCES

- Applied Technology Council. (2019). Seismic performance assessment of buildings, Volume 1: Methodology, Second Edition (FEMA P-58-1). Federal Emergency Management Agency.
- Baker, Jack W. (2015) Introduction to Probabilistic Seismic Hazard Analysis. White Paper Version 2.1, 77 pp
- Díaz, S. A., Pinzón, L. A., Vargas-Alzate, Y. F., & Mora-Ortiz, R. S. (2023). Seismic Damage “Semaphore” Based on the Fundamental Period Variation: A Probabilistic Seismic Demand Assessment of Steel Moment-Resisting Frames. *Buildings*, 13(4), 1009.
- Ditommaso, R., Vona, M., Gallipoli, M. R., & Mucciarelli, M. (2013). Evaluation and considerations about fundamental periods of damaged reinforced concrete buildings. *Natural Hazards and Earth System Sciences*, 13(7), 1903-1912.
- Eleftheriadou, A. K., & Karabinis, A. I. (2013). Correlation of structural seismic damage with fundamental period of RC buildings.
- E.P.P.O. (2022) Code of Structural Interventions (KAN.ΕΠΕ.), 3rd Revision 2022, Athens, Greece
- Federal Emergency Management Agency (FEMA) and National Institute of Building Sciences (NIBS), 2020. Hazus Earthquake Model Technical Manual, Hazus 4.2 SP3. Washington DC
- Gallipoli, M. R., Stabile, T. A., Guéguen, P., Mucciarelli, M., Comelli, P., & Bertoni, M. (2016). Fundamental period elongation of a RC building during the Pollino seismic swarm sequence. *Case Studies in Structural Engineering*, 6, 45-52.
- ITSAK, CEA-Cadarache, IU, UP, 2015. ARGONET, a vertical accelerometric array implemented on the island of Kefalonia in Greece. [Data set/Seismic Network]. International Federation of Digital Seismograph Networks.
- Karakostas, C.Z., Papanikolaou, V.K. A low-cost instrumentation approach for seismic hazard assessment in urban areas, *Risk Analysis 2014*, Wessex Institute of Technology, June 2014.
- Karakostas, C.Z., Papanikolaou, V.K. and Theodoulidis, N. An ultra-dense strong-motion urban network based on in-house designed MEMS accelerographs - The case of Lefkas city, 16th European Conference on Earthquake Engineering, Thessaloniki, Greece, June 2018.
- Kirtas, E., Trevelopoulos, K., Rovithis, E., & Pitilakis, K. (2007). Discussion on the fundamental period of Sdof systems including soil-structure interaction. In 4th International Conference on Earthquake Geotechnical Engineering, Thessaloniki, Greece.
- Kishida, T., Ktenidou, O.J., Darragh, R.B., Walter, S., 2016. Semi-automated procedure for windowing time series and computing Fourier amplitude spectra (FAS) for the NGA-West2 database.
- Martins, L., & Silva, V. (2021). Development of a fragility and vulnerability model for global seismic risk analyses. *Bulletin of Earthquake Engineering*, 19(15), 6719-6745.

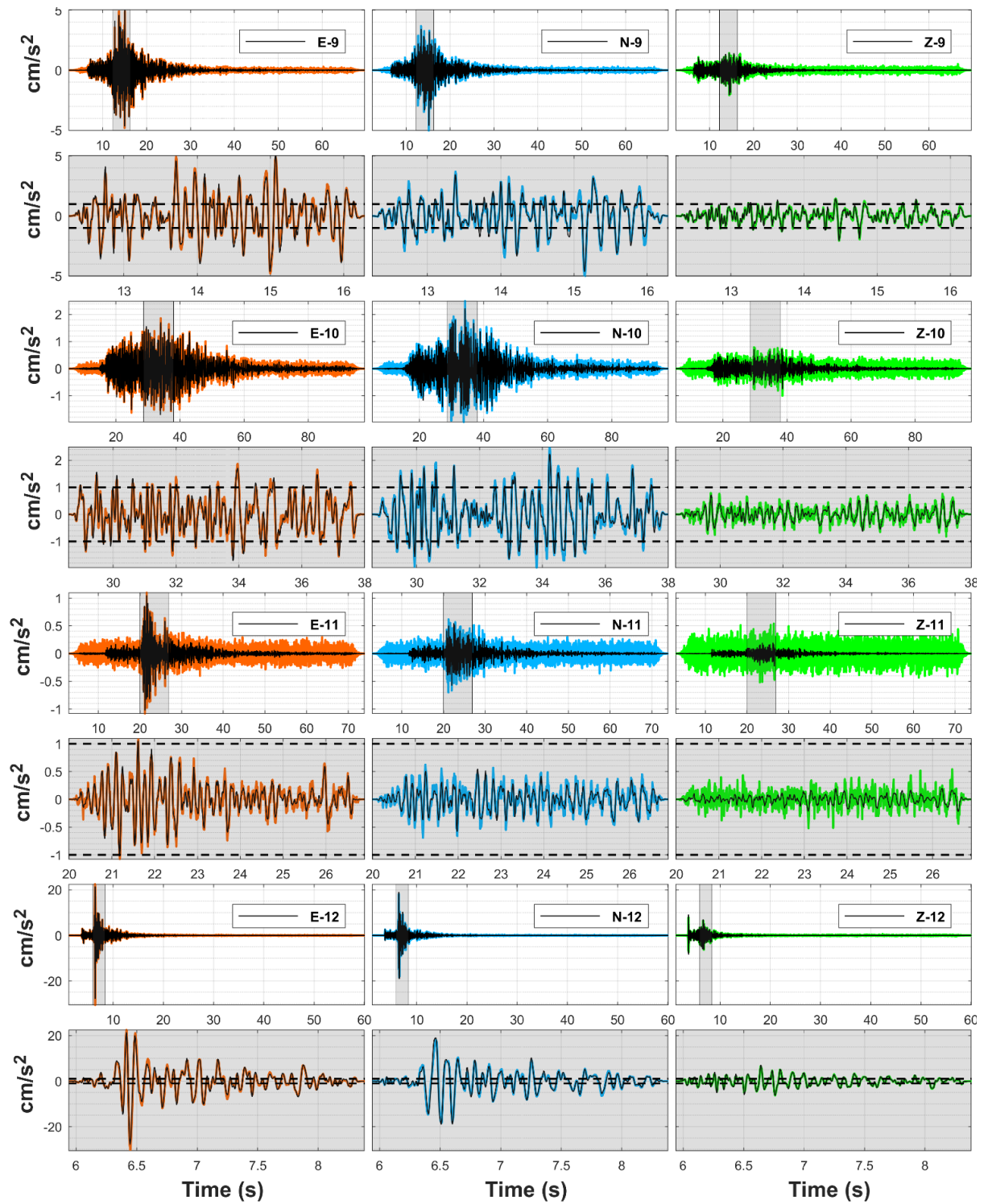
- Papanikolaou, V.K and Karakostas, C.Z. Explicit shakemaps via low-cost instrumentation: The case of Lefkas city, Second European Conference on Earthquake Engineering and Seismology, Istanbul, August 2014.
- Papanikolaou, V.K., Karakostas, C.Z. A low-cost MEMS-based accelerograph, Experimental Vibration Analysis for Civil Engineering Structures EVACES'13, Ouro Preto, Brazil, October 2013, pp. 116-123.
- Papanikolaou, V.K., Karakostas, C.Z. and Theodoulidis, N.P. A Low-Cost Instrumentation System for Seismic Hazard Assessment in Urban Areas, Sensors, 2021, Vol. 21, No. 11, 03618.
- Rossetto, T. (2004). Vulnerability Curves for the Seismic Assessment of Reinforced Concrete Building Populations [PhD Thesis]. In *Environmental Engineering*. Imperial College, University of London.
- Stewart, J. P., Seed, R. B., & Fenves, G. L. (1998). Empirical evaluation of inertial soil-structure interaction effects (No. 7). Berkeley: Pacific Earthquake Engineering Research Center.
- Su, R.K.L., Lam, N. T. K., & Tsang, H.H. (2008). Seismic Drift Demand and Capacity of Non-seismically Designed Concrete Buildings in Hong Kong. *Electronic Journal of Structural Engineering*, 01, 110-121. <https://doi.org/10.56748/ejse.9101>
- TBSDC-2018, Turkish Building Seismic Design Code, Disaster and Emergency Management Authority, Ankara, 2018.
- Theodoulidis, N., Hollender, F., Mariscal, A., Moiriat, D., Bard, P.Y., Konidakis, A., Cushing, M., Konstantinidou, K., Roumelioti, Z., 2018. The ARGONET (Greece) seismic observatory: An accelerometric vertical array and its data. *Seismol. Res. Lett.* 89, 1555-1565.

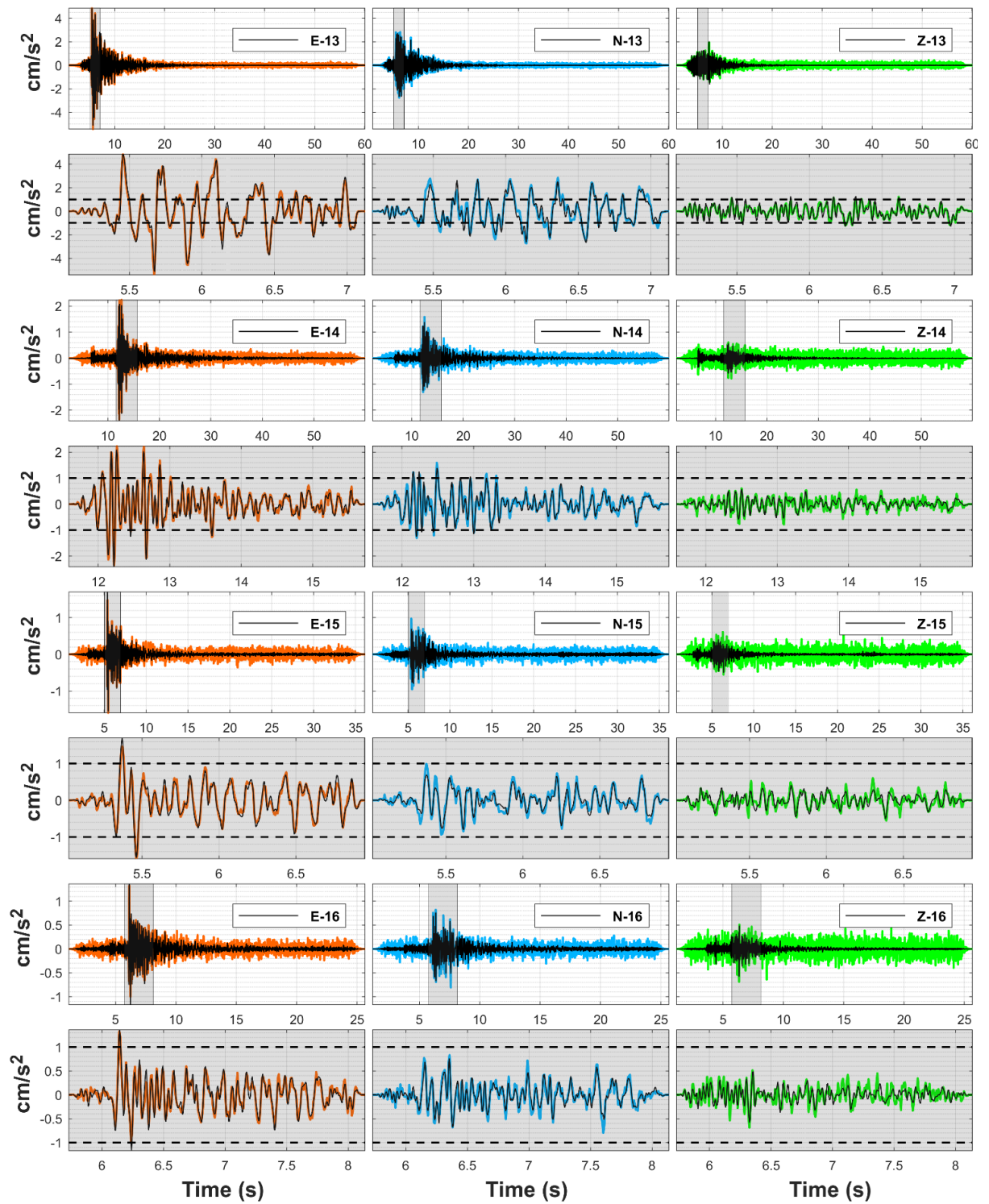
**APPENDIX-A: TESTING RESULTS IN TIME DOMAIN (ACCELERATION TIME HISTORIES)**

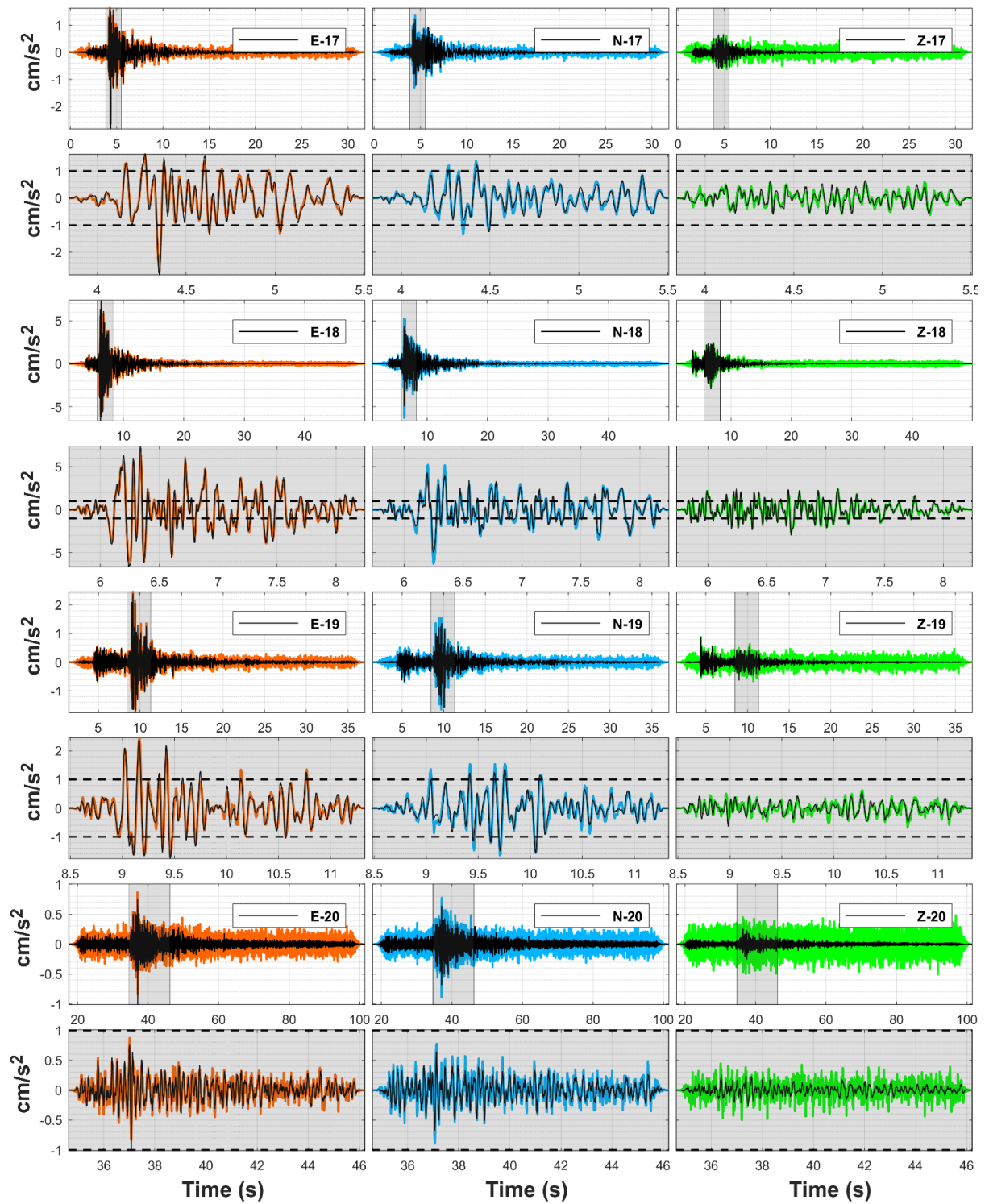




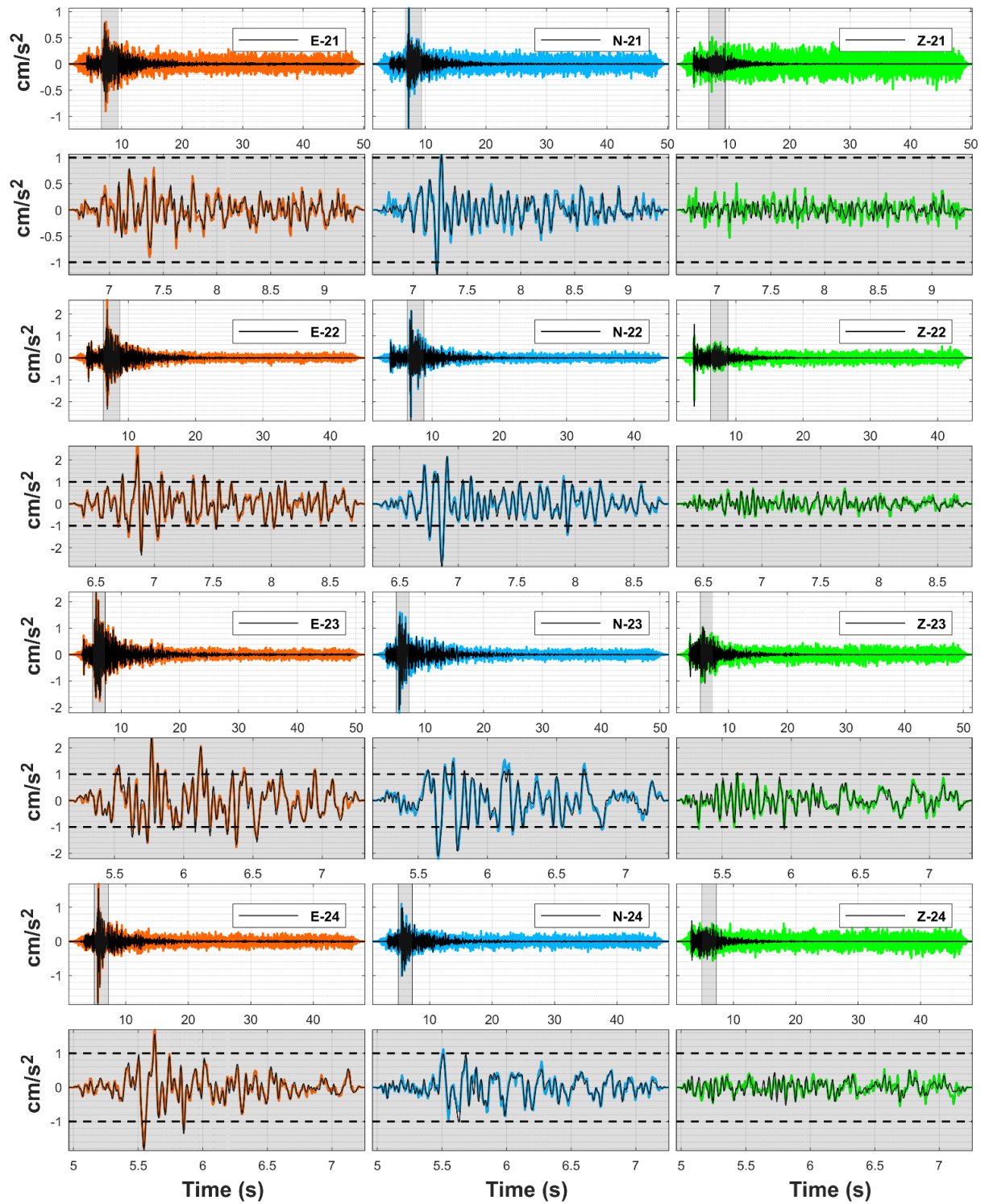
Earthquake Resilient Schools - EReS [BSB 966]  
Project Nr: 101101206 (UCPM-2022-PP)  
Deliverable D4.1: Investigation of seismic risk indicators based on instrumentation  
of school buildings in the selected pilot sites

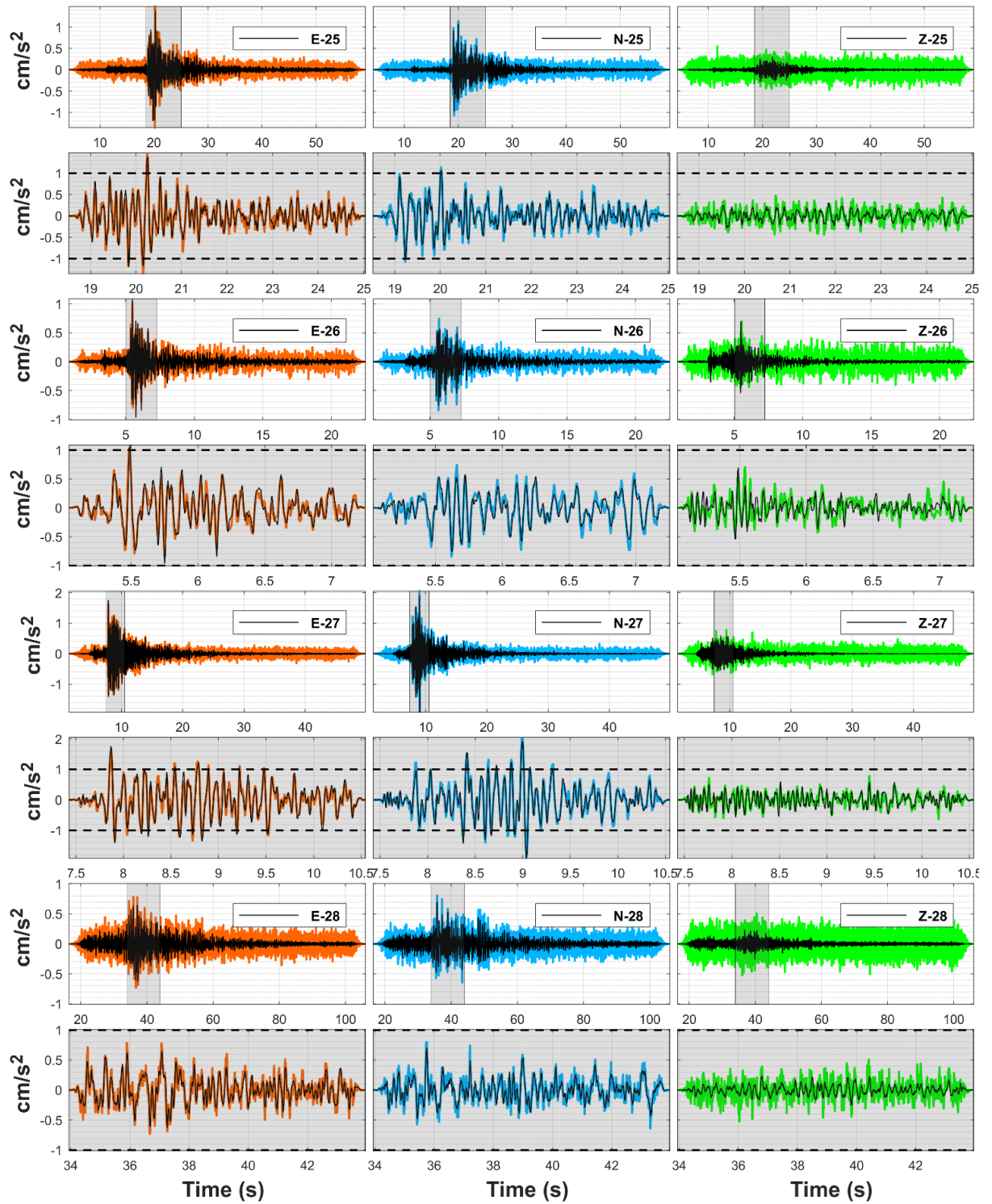


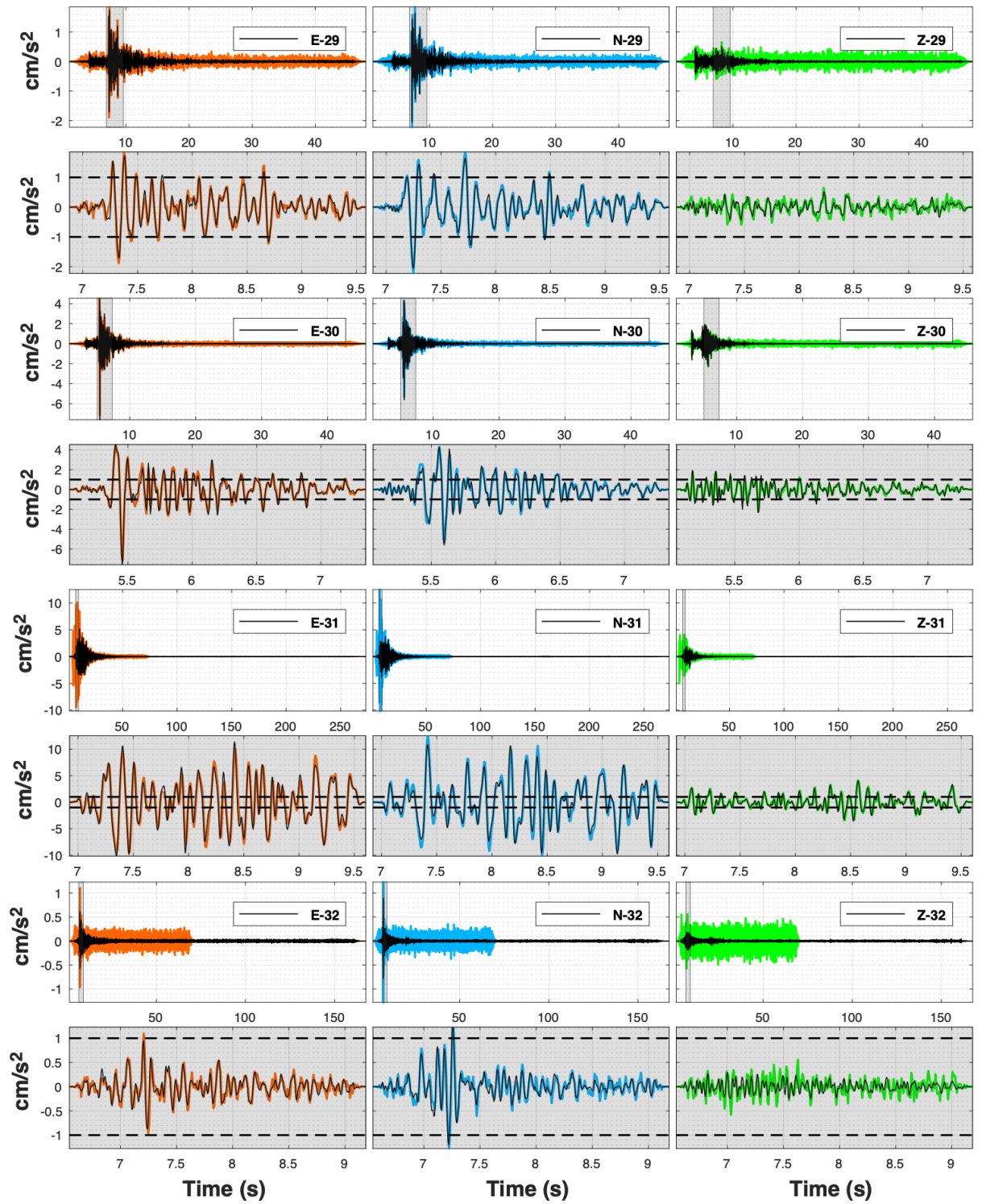




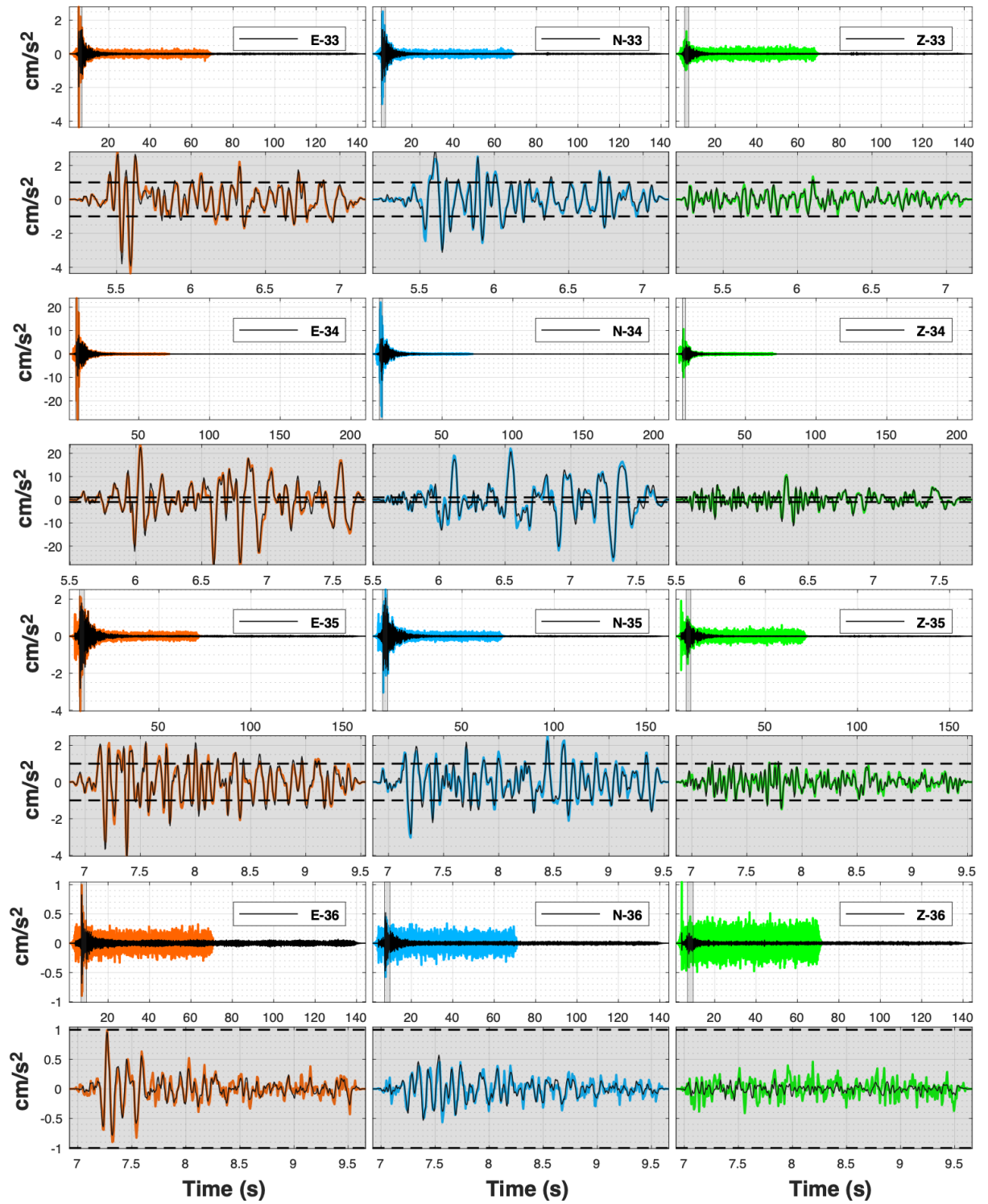
Earthquake Resilient Schools - EReS [BSB 966]  
Project Nr: 101101206 (UCPM-2022-PP)  
Deliverable D4.1: Investigation of seismic risk indicators based on instrumentation  
of school buildings in the selected pilot sites



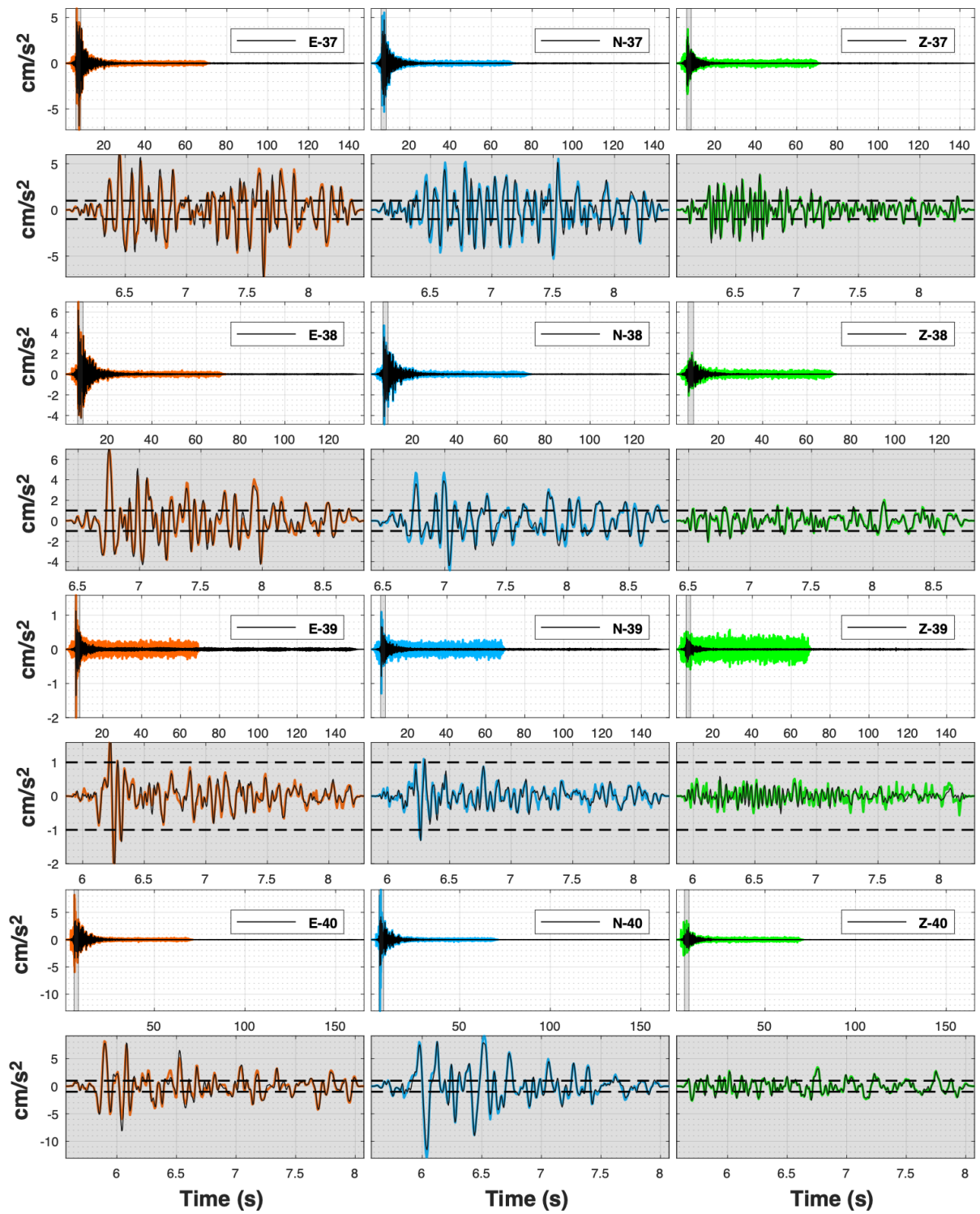




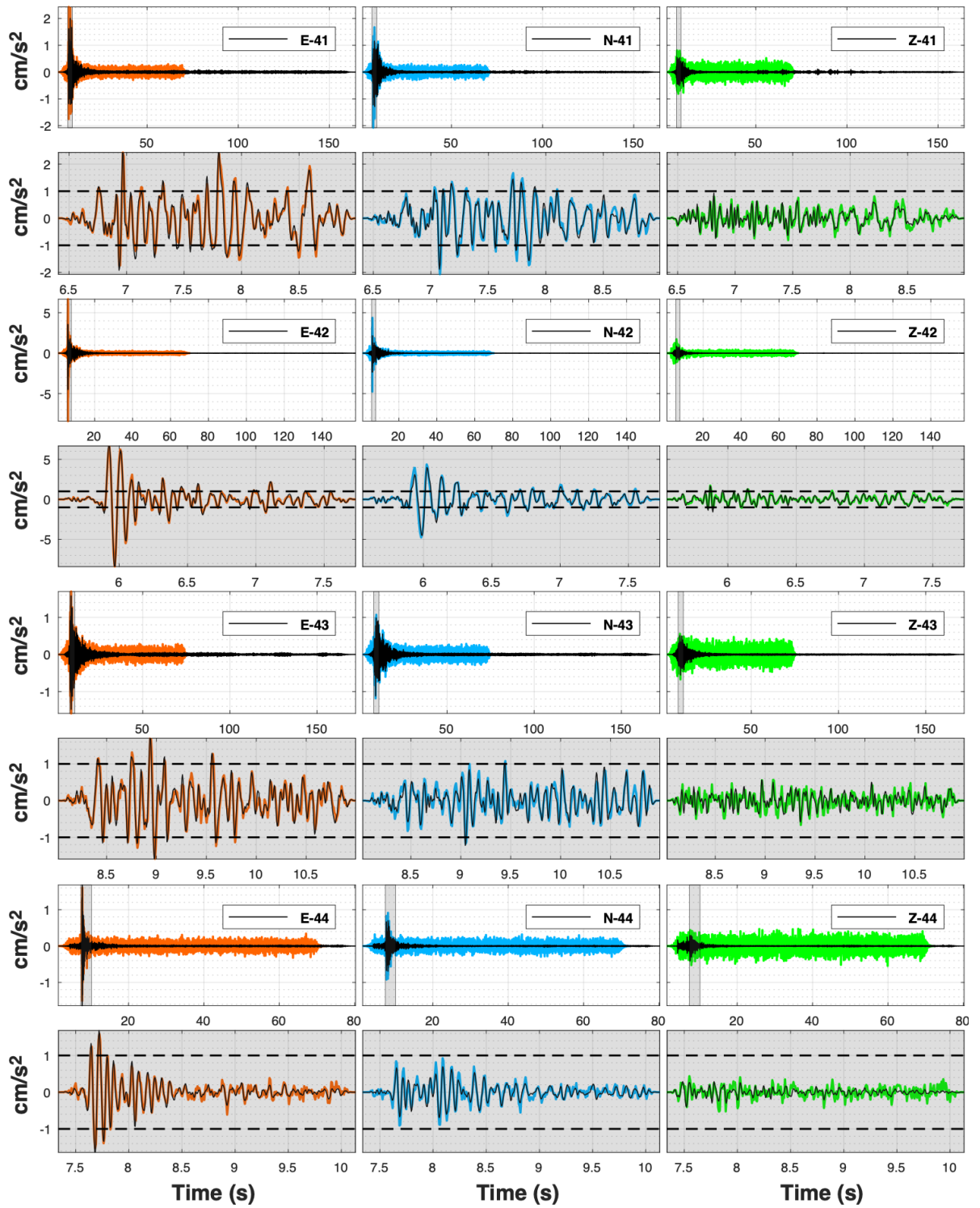
Earthquake Resilient Schools - EReS [BSB 966]  
Project Nr: 101101206 (UCPM-2022-PP)  
Deliverable D4.1: Investigation of seismic risk indicators based on instrumentation  
of school buildings in the selected pilot sites



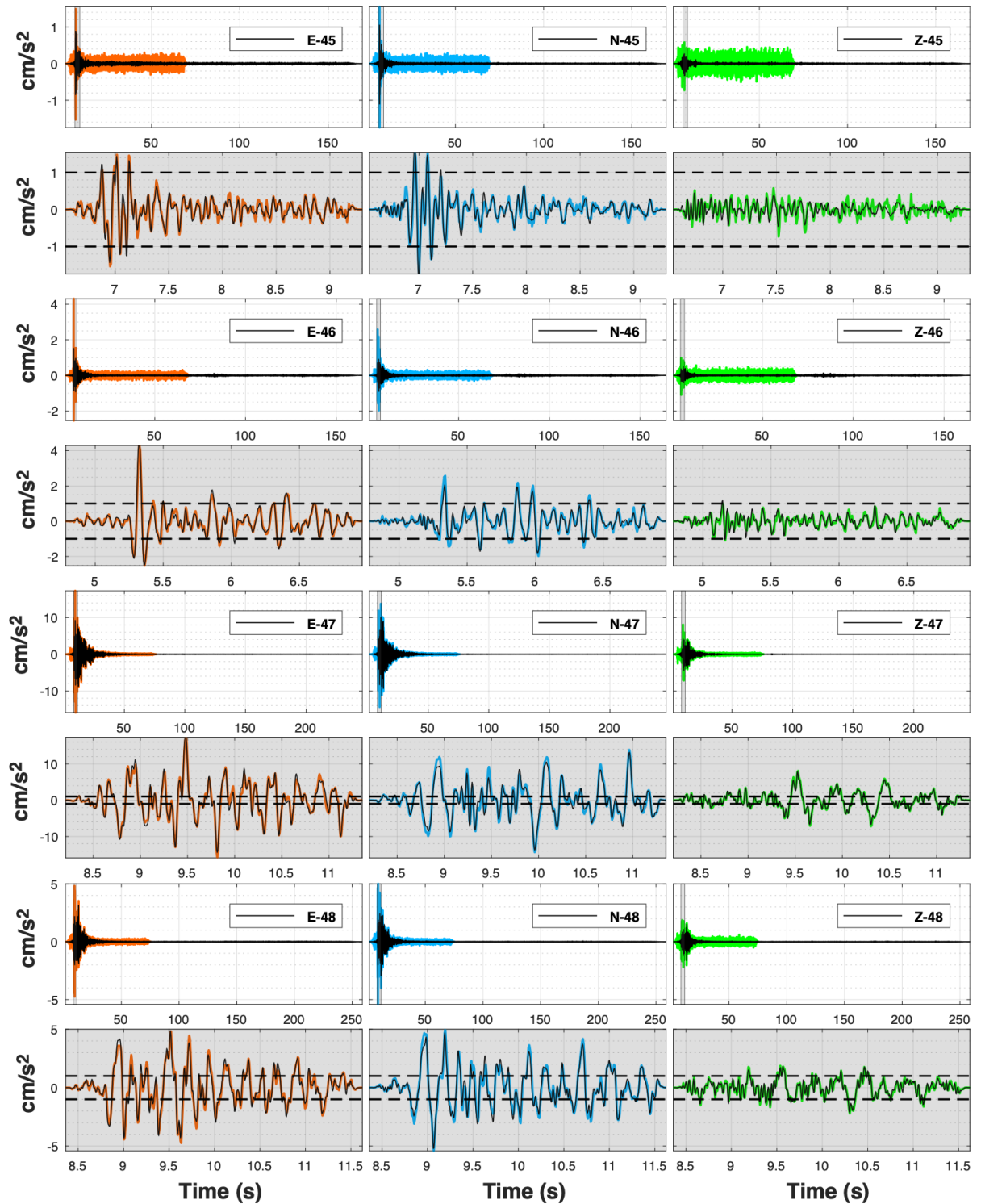
Earthquake Resilient Schools - EReS [BSB 966]  
Project Nr: 101101206 (UCPM-2022-PP)  
Deliverable D4.1: Investigation of seismic risk indicators based on instrumentation  
of school buildings in the selected pilot sites



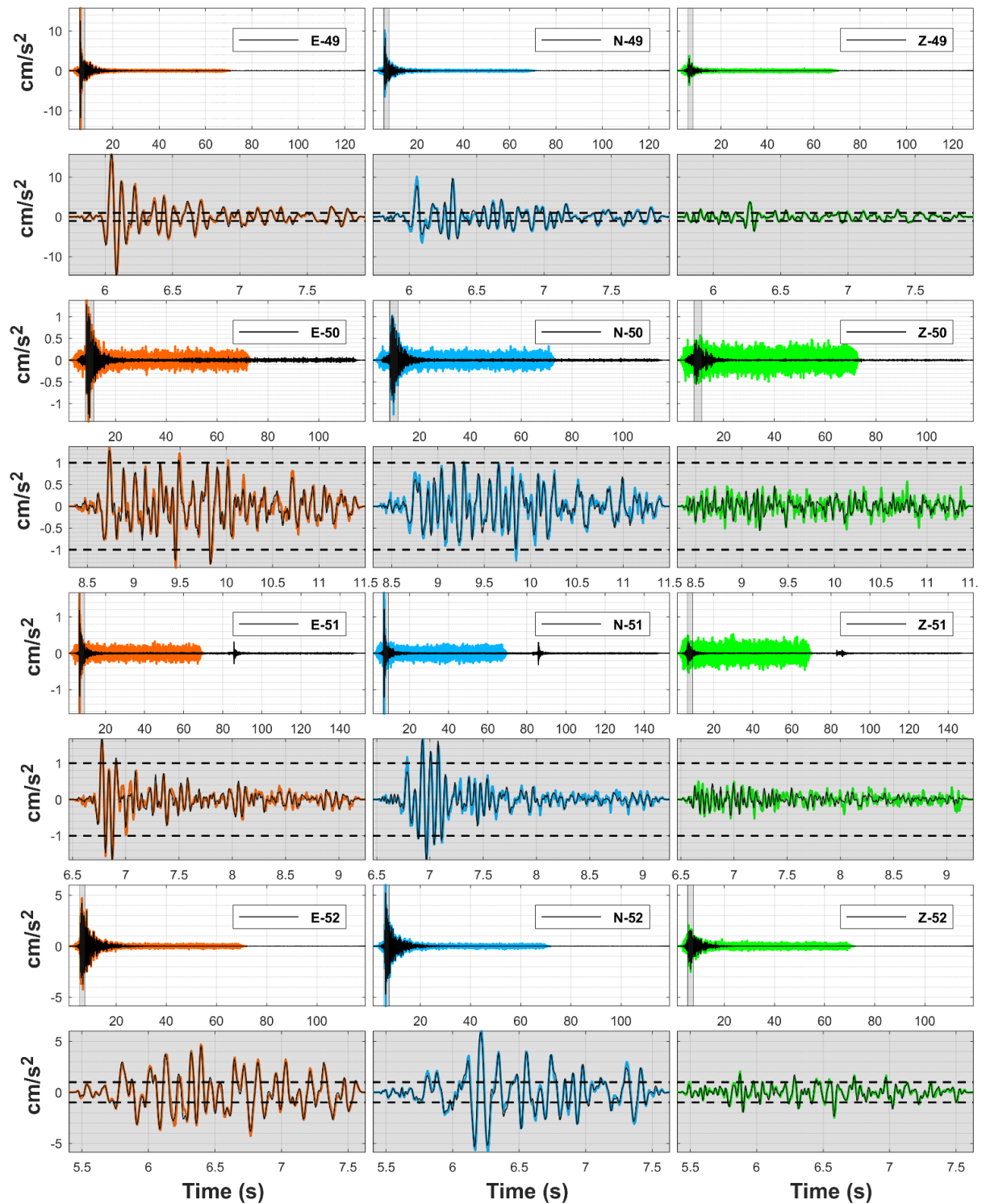
Earthquake Resilient Schools - EReS [BSB 966]  
Project Nr: 101101206 (UCPM-2022-PP)  
Deliverable D4.1: Investigation of seismic risk indicators based on instrumentation  
of school buildings in the selected pilot sites



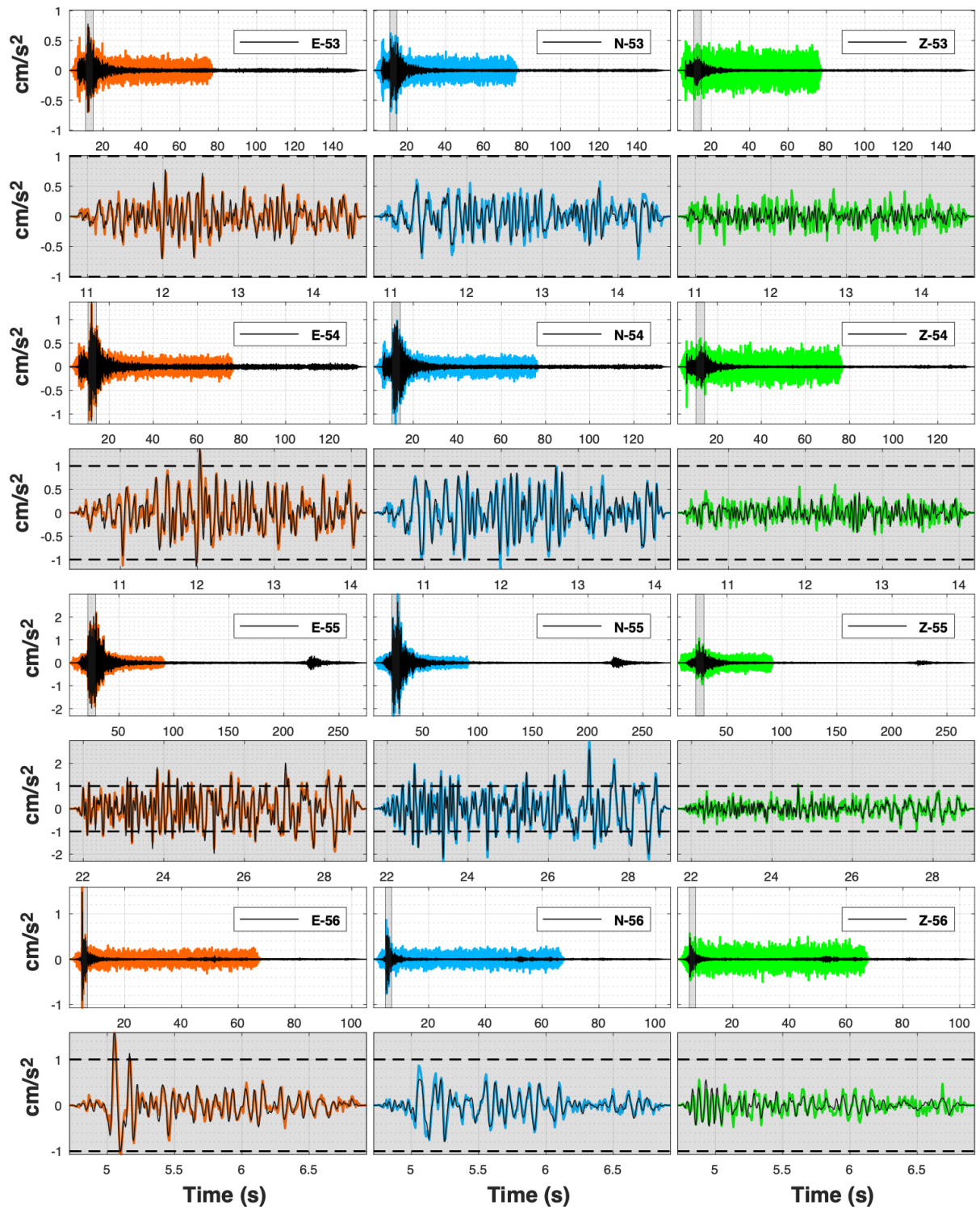
Earthquake Resilient Schools - EReS [BSB 966]  
Project Nr: 101101206 (UCPM-2022-PP)  
Deliverable D4.1: Investigation of seismic risk indicators based on instrumentation  
of school buildings in the selected pilot sites

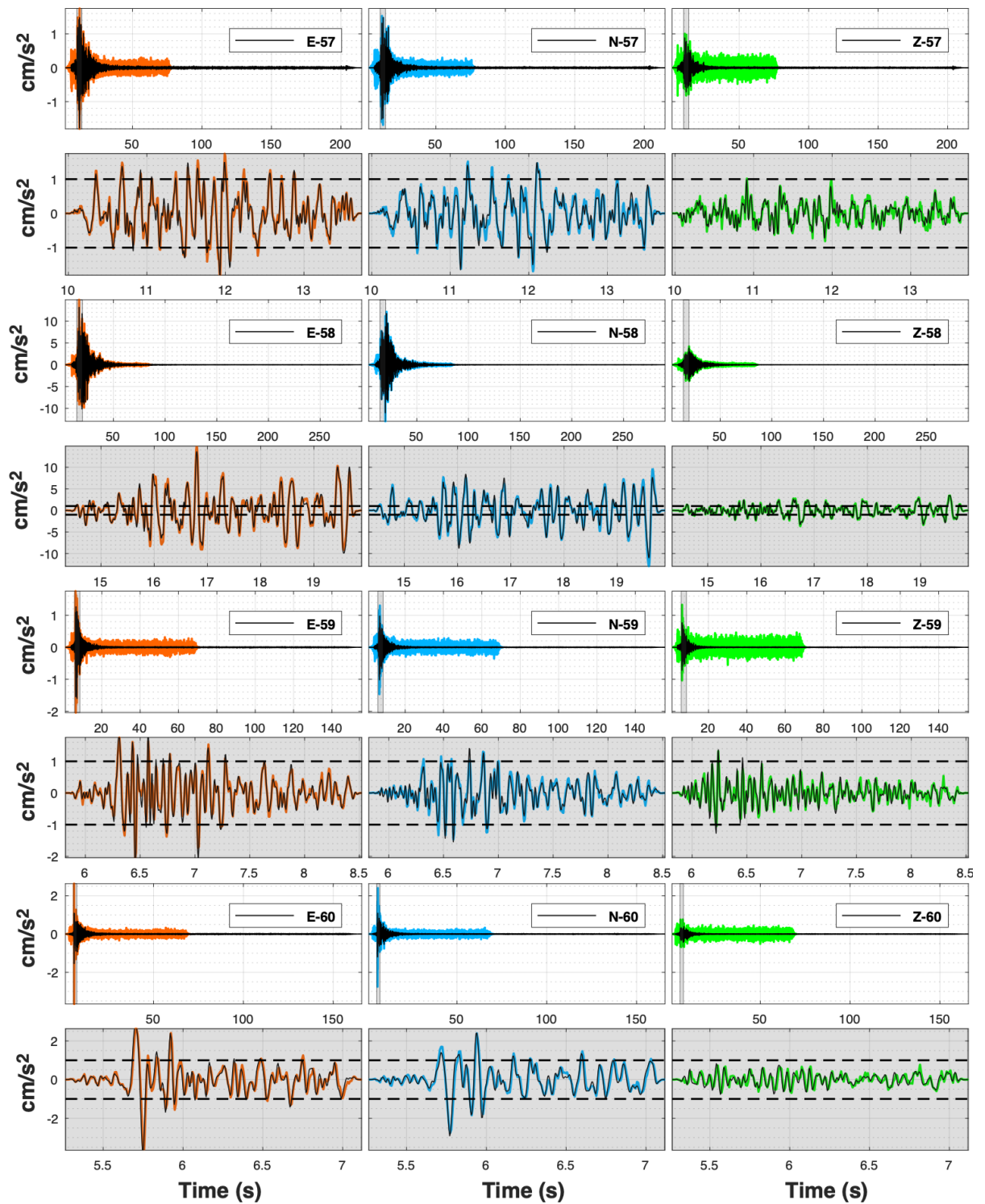


Earthquake Resilient Schools - EReS [BSB 966]  
Project Nr: 101101206 (UCPM-2022-PP)  
Deliverable D4.1: Investigation of seismic risk indicators based on instrumentation  
of school buildings in the selected pilot sites

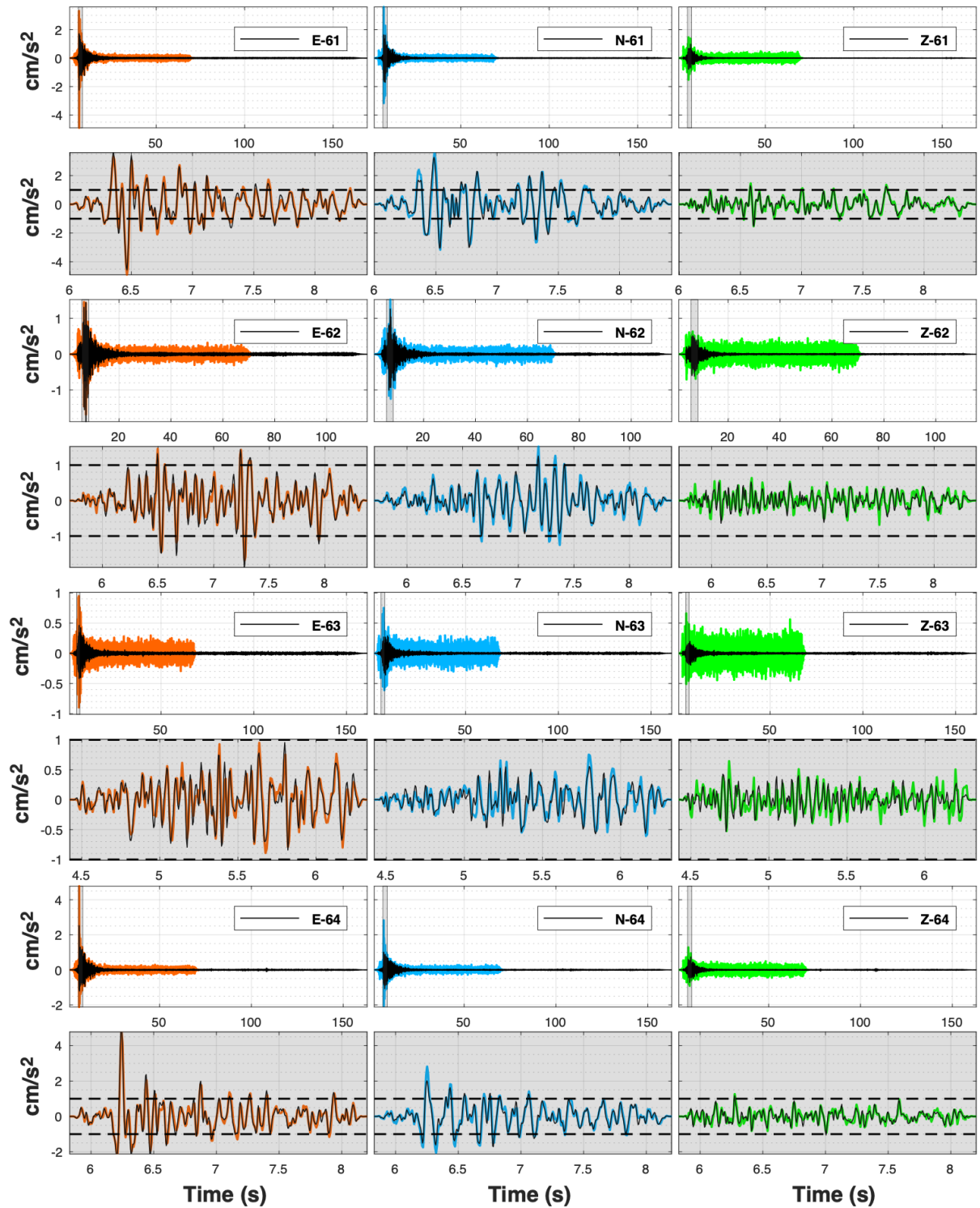


Earthquake Resilient Schools - EReS [BSB 966]  
Project Nr: 101101206 (UCPM-2022-PP)  
Deliverable D4.1: Investigation of seismic risk indicators based on instrumentation  
of school buildings in the selected pilot sites

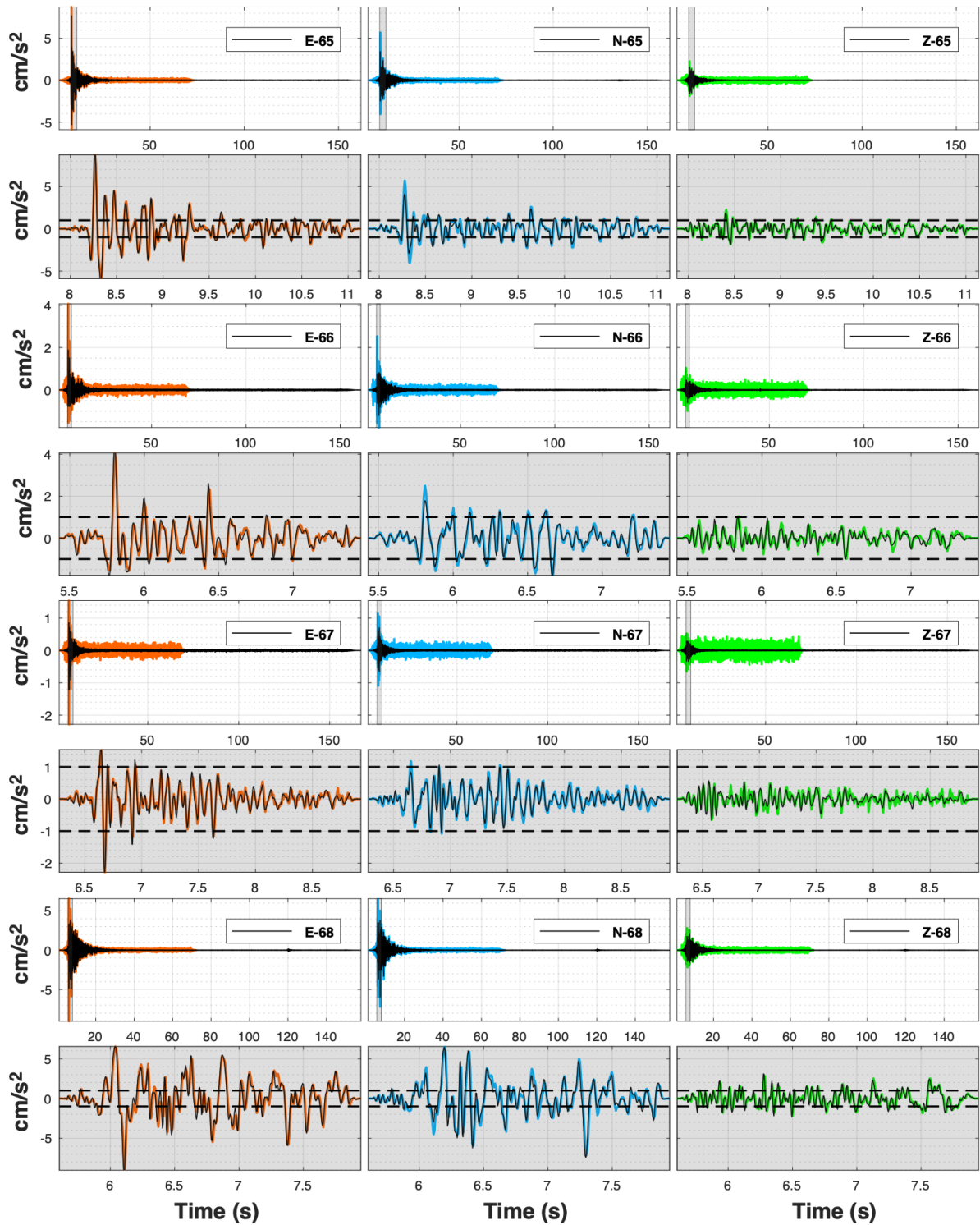




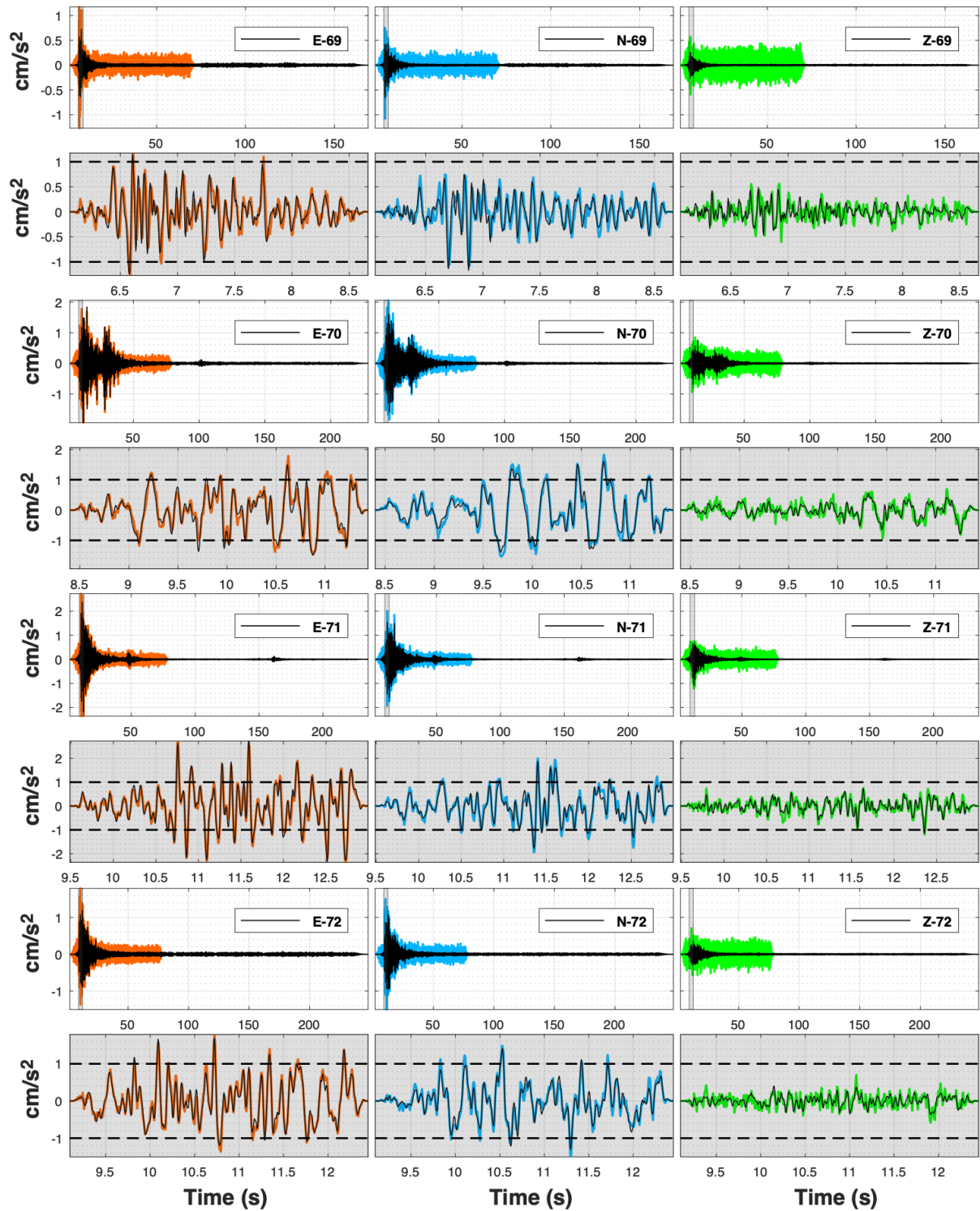
Earthquake Resilient Schools - EReS [BSB 966]  
Project Nr: 101101206 (UCPM-2022-PP)  
Deliverable D4.1: Investigation of seismic risk indicators based on instrumentation  
of school buildings in the selected pilot sites



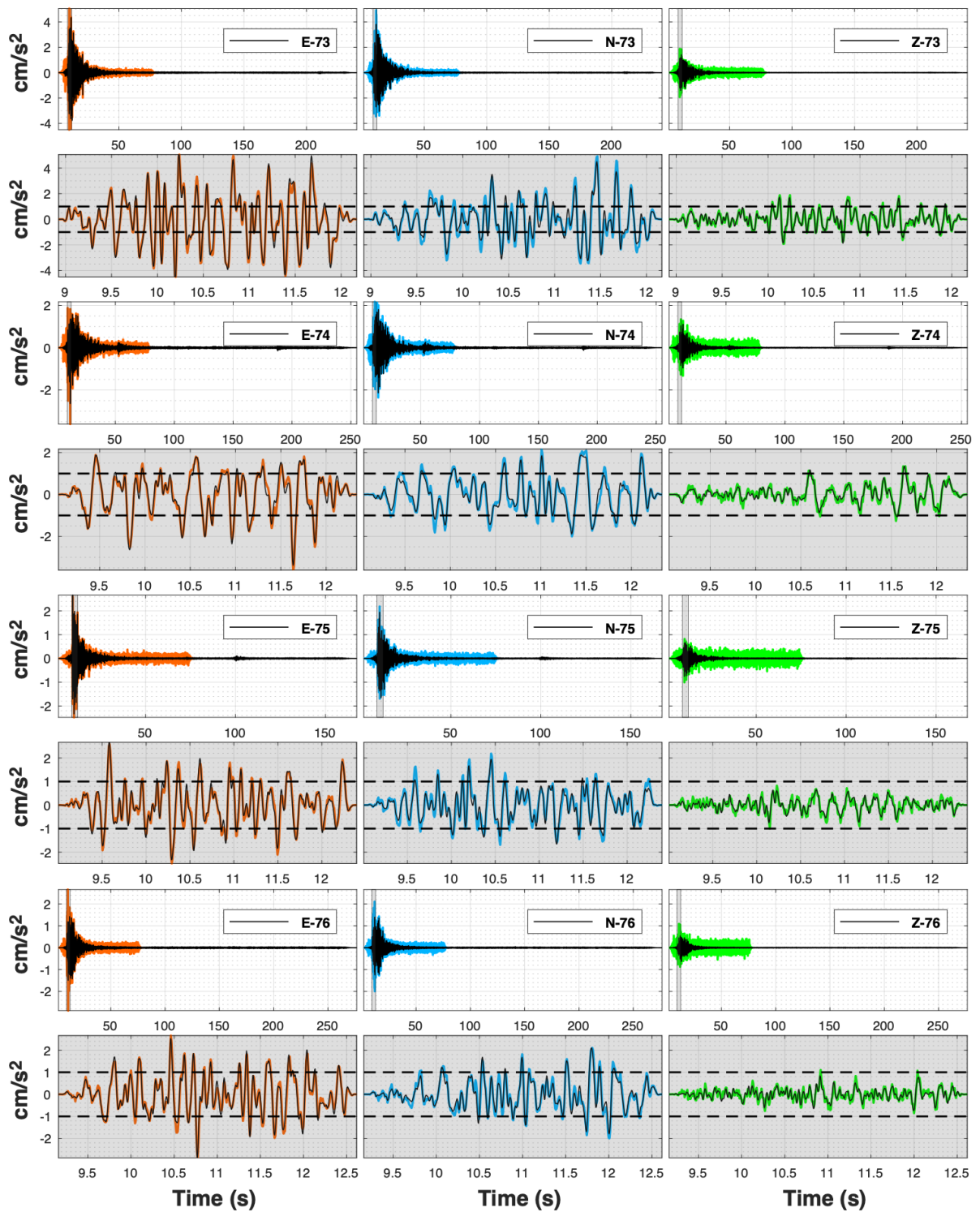
Earthquake Resilient Schools - EReS [BSB 966]  
Project Nr: 101101206 (UCPM-2022-PP)  
Deliverable D4.1: Investigation of seismic risk indicators based on instrumentation  
of school buildings in the selected pilot sites



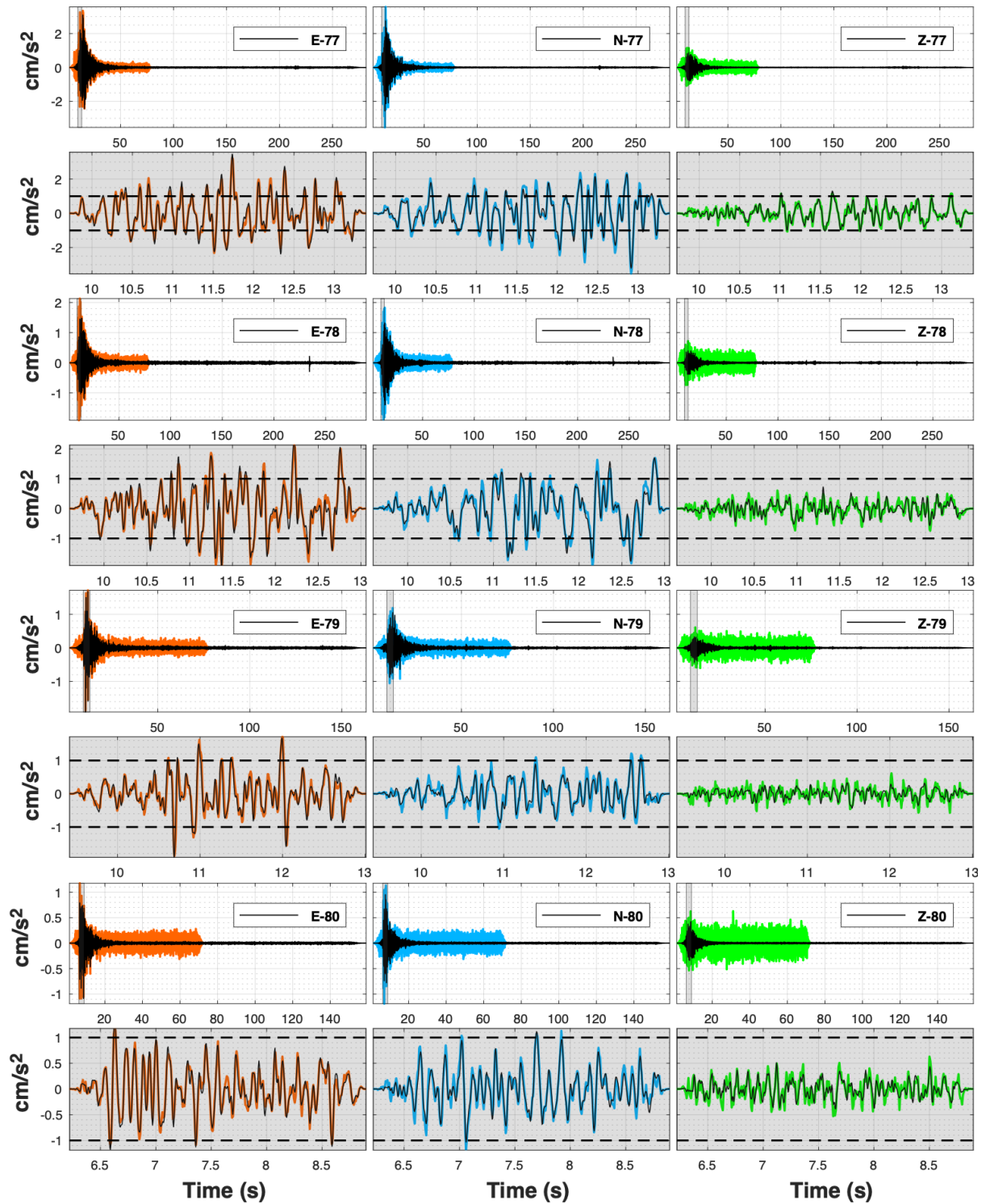
Earthquake Resilient Schools - EReS [BSB 966]  
Project Nr: 101101206 (UCPM-2022-PP)  
Deliverable D4.1: Investigation of seismic risk indicators based on instrumentation  
of school buildings in the selected pilot sites

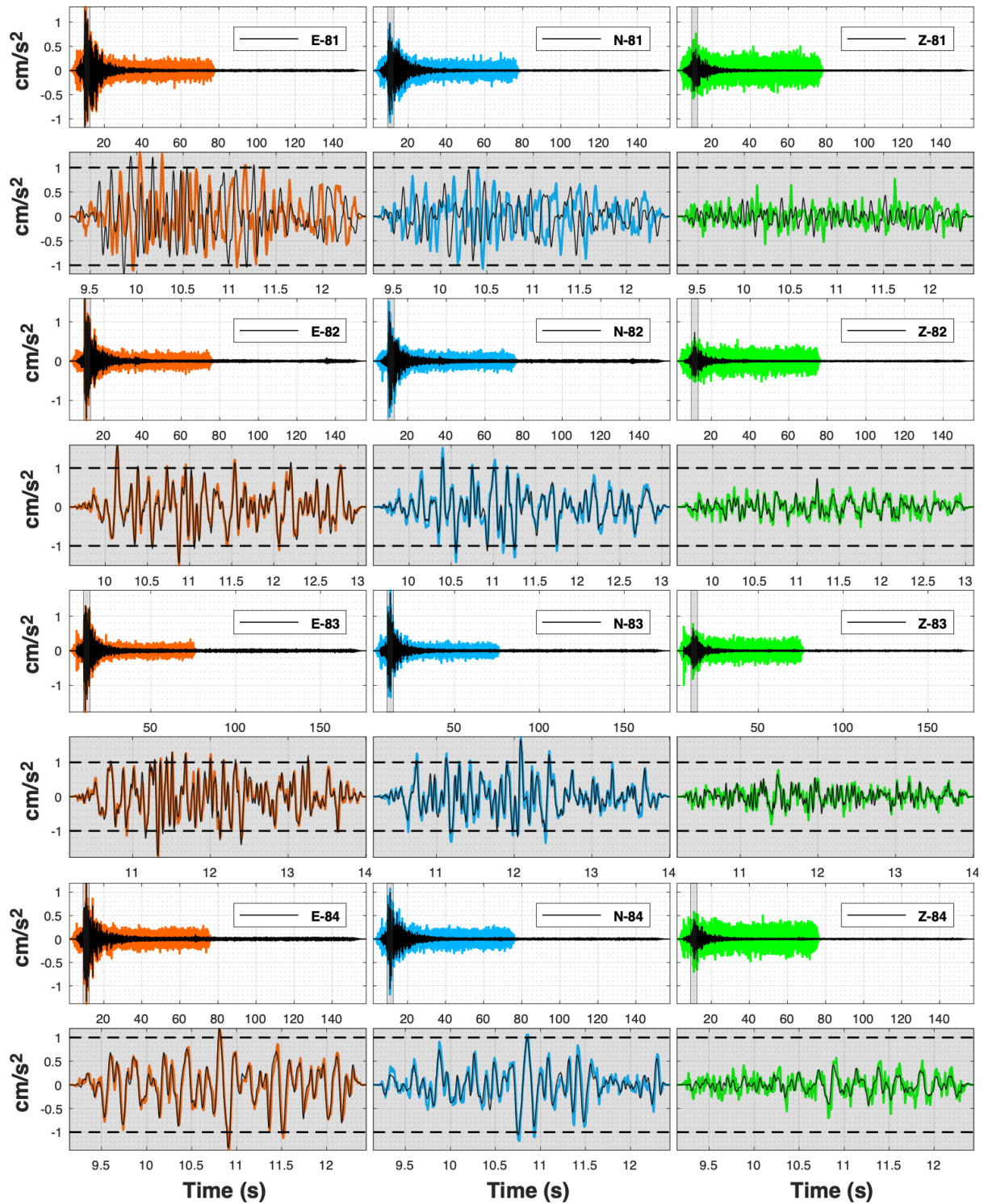


Earthquake Resilient Schools - EReS [BSB 966]  
Project Nr: 101101206 (UCPM-2022-PP)  
Deliverable D4.1: Investigation of seismic risk indicators based on instrumentation  
of school buildings in the selected pilot sites

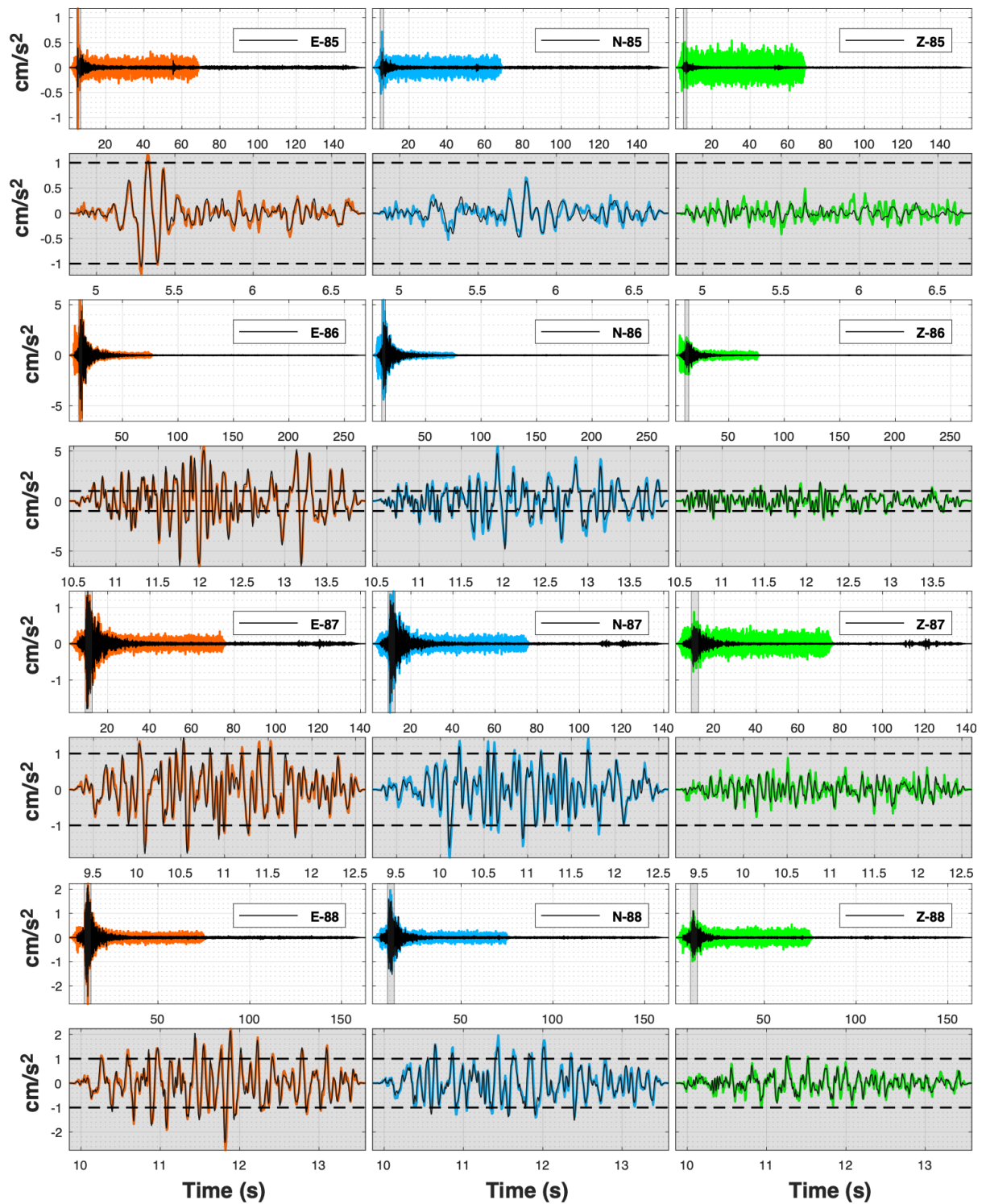


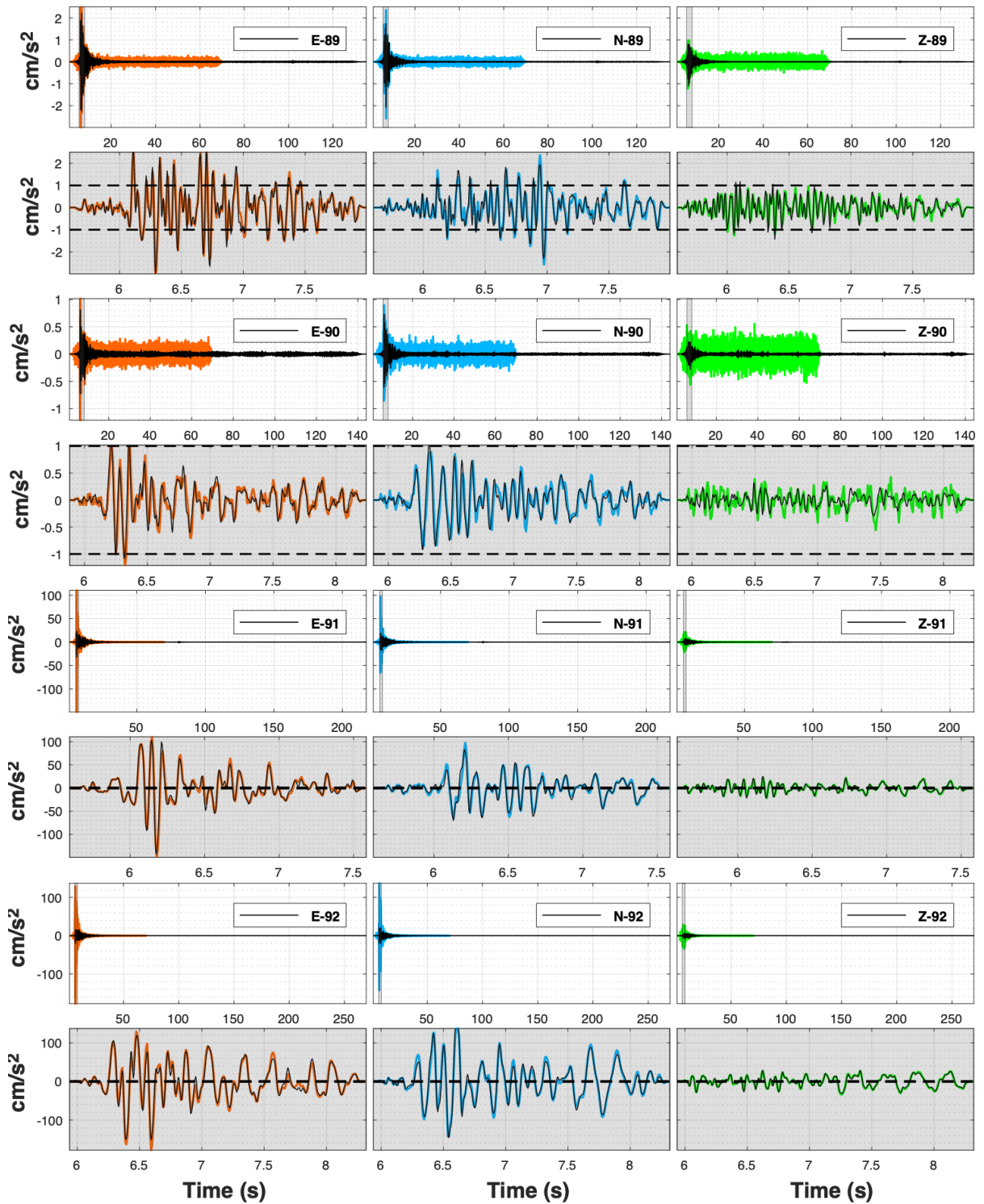
Earthquake Resilient Schools - EReS [BSB 966]  
Project Nr: 101101206 (UCPM-2022-PP)  
Deliverable D4.1: Investigation of seismic risk indicators based on instrumentation  
of school buildings in the selected pilot sites



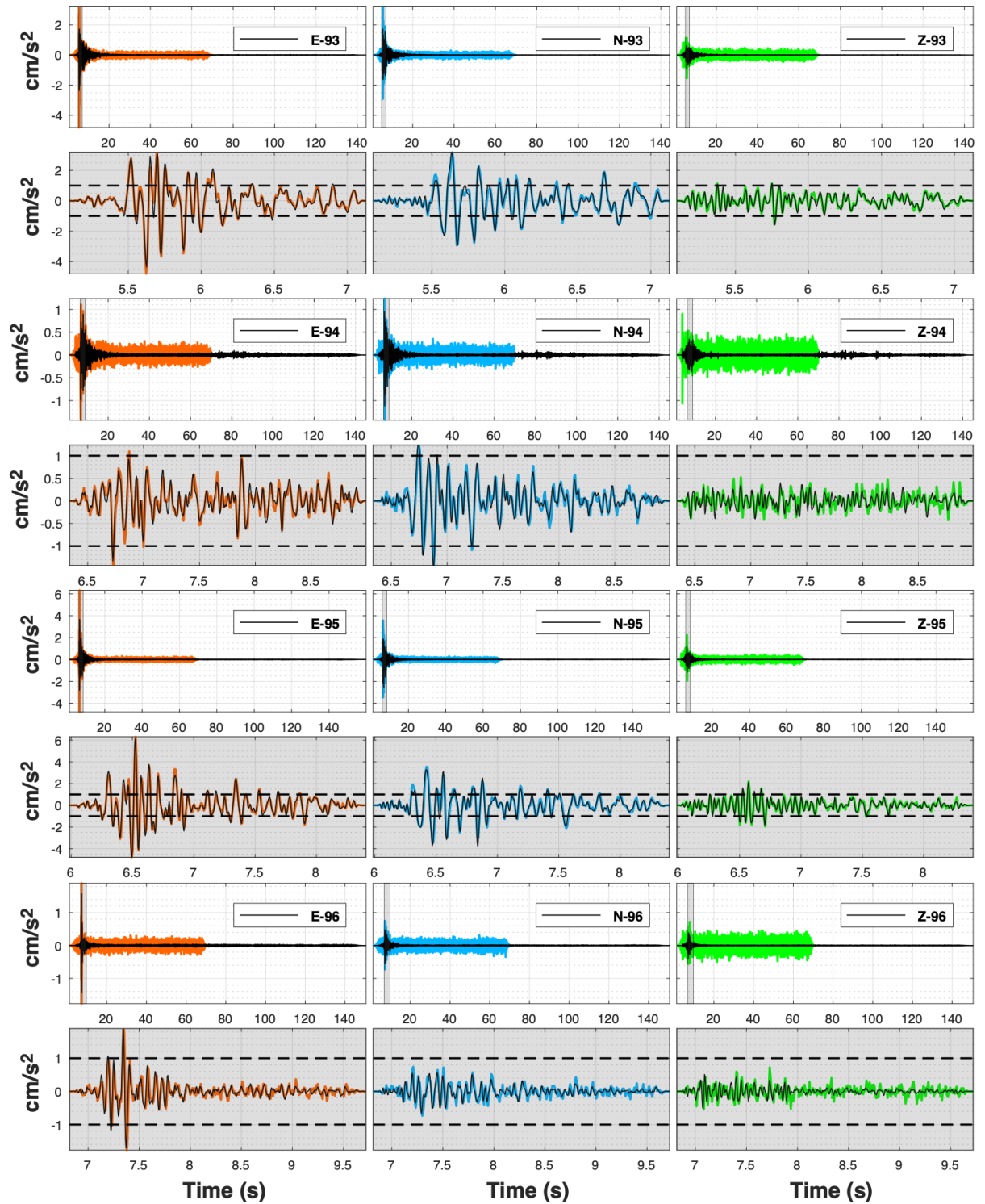


Earthquake Resilient Schools - EReS [BSB 966]  
Project Nr: 101101206 (UCPM-2022-PP)  
Deliverable D4.1: Investigation of seismic risk indicators based on instrumentation  
of school buildings in the selected pilot sites



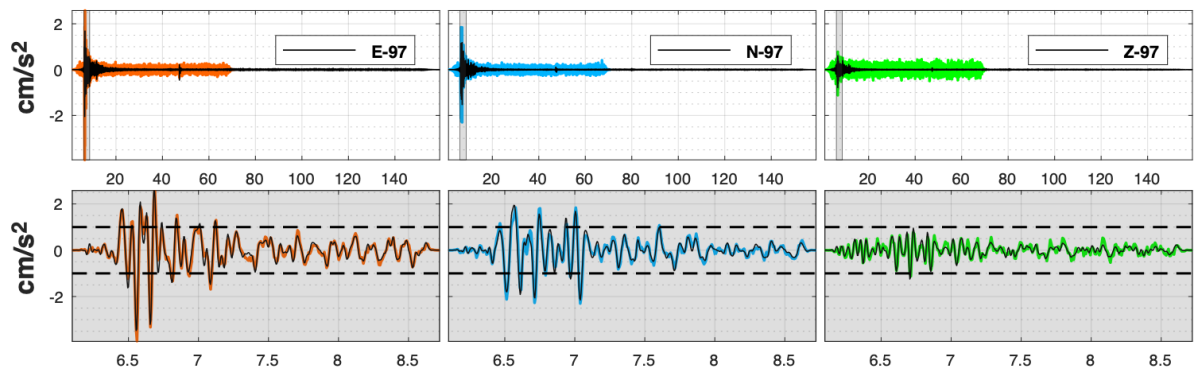


Earthquake Resilient Schools - EReS [BSB 966]  
Project Nr: 101101206 (UCPM-2022-PP)  
Deliverable D4.1: Investigation of seismic risk indicators based on instrumentation  
of school buildings in the selected pilot sites



Earthquake Resilient Schools - EReS [BSB 966]  
Project Nr: 101101206 (UCPM-2022-PP)  
Deliverable D4.1: Investigation of seismic risk indicators based on instrumentation  
of school buildings in the selected pilot sites

---



**APPENDIX-B: TESTING RESULTS IN FREQUENCY DOMAIN (FAS)**

